**Title**
Delamination of Bacterial Biofilms using Laser-Generated Shockwaves



**Author**
Ramaprasad, Vidyunmala

**Publication Date**
2014

Peer reviewed|Thesis/dissertation

UNIVERSITY OF CALIFORNIA
Los Angeles

# Delamination of Bacterial Biofilms Using Laser-Generated Shockwaves

A dissertation submitted in partial satisfaction
of the requirements for the degree
Doctor of Philosophy in Biomedical Engineering

by

**Vidyunmala Ramaprasad**

2014

ABSTRACT OF THE DISSERTATION

# Delamination of Bacterial Biofilms Using Laser-Generated Shockwaves

by

**Vidyunmala Ramaprasad**

Doctor of Philosophy in Biomedical Engineering

University of California, Los Angeles, 2014

Professor Warren S. Grundfest, Chair

The goal of this thesis is to explore the use of laser generated shockwaves (LGS) as a potential methodology to treat wound surfaces infected with bacterial biofilm as they impose a major financial, economic and social burden on the society.

First, the basics of LGS and how the concept could be used as a potential treatment technique needed to be understood. For this, LGS technique was initially used to delaminate biofilm grown on polystyrene and PDMS surfaces. The system is based on a Q-switched, Nd:YAG pulsed laser with an output wavelength of 1064 nm and a pulse width between $2-6$ ns that ablates titanium-coated target (glass) under confinement, thereby generating unipolar compressive waves. The adhesion strength of S. epidermidis biofilms grown on polystyrene, under static growth conditions was found to be 22.75 MPa ±0.16% using interferometry techniques. Biofilm material properties measured by other techniques vary significantly due to the viscoelastic effect of biofilms under low strain rates. LGS technique exclusively uses compressive waves and high strain rate loading, thus the decohesive failure observed is an intrinsic strength measurement of the material and does not vary.

A low-cost, high-speed imaging system was developed and characterized to capture the LGS as they travel through the titanium- coated target and coupling medium. Cavitation bubbles forming at the glass/ water interface, and propagating in the same direction as the compressive wave were successfully imaged. As observed during biofilm delamination experiments these bubbles were responsible for causing localized delamination of the biofilm.

Preliminary studies to examine the safety of LGS on ex vivo skin (porcine skin) were conducted. These studies were conducted to ascertain the impact of LGS on skin tissues that would underlie the biofilm in a typical wound bed. LGS on *ex vivo* porcine skin caused no qualitative structural damage at energy fluences between 16.68 and $70.42 mJ/mm^2$. All the 3 layers of the skin, the stratum corneum, epidermis and dermis remained intact. The collagen structure also appeared undisturbed by LGS treatment.

A thorough study to determine the damage threshold for *ex vivo* porcine skin was carried out. The effect of a wide range of energy fluences from 250 mJ (35.38 mJ/$mm^2$) to 1500mJ (212.28 mJ/$mm^2$) was studied. A large number of samples (total of 105 tissue samples) was used in this study. By scoring the tissue samples based on the damage that had occurred to them and performing statistical analysis on the scores, the damage threshold for *ex vivo* porcine skin was determined to be 1500mJ (212.28 mJ/$mm^2$).

The biofilm delamination studies and experiments to determine damage threshold of *ex vivo* porcine skin has provided an optimal range of energy fluences that would cause biofilm delamination as well as be safe to use for *in vivo* experiments.

Finally, the LGS propagation through the coupling medium, biofilm and underlying

muscle was modeled using COMSOL. This model would help predict the outcome of changing any of the parameters in the experimental set up. It will also be able to predict the effect of multiple shockwaves on the biofilm and the underlying muscle tissue. This will drastically reduce the number experimental trials needed to be performed when any changes to the system are proposed in order to make the system more suitable for *in vivo* or clinical settings saving tremendous amount of money, time and effort.

The dissertation of Vidyunmala Ramaprasad is approved.

Daniel B. Ennis

David A. Haake

Michael Albert Thomas

Warren S. Grundfest, Committee Chair

University of California, Los Angeles

2014

*To my family*

# Table of Contents

# List of Figures

# List of Tables

# Acknowledgments

I take this opportunity to thank my adviser, Prof Warren Grundfest for teaching and guiding me through all these years. His encouraging words, invaluable criticism and sparkling wit kept me motivated and focused. I learnt from him how to take it in my stride and keep at it when things did not work out. Through the course of my PhD, he gave me the opportunity to serve as his teaching assistant because of which I discovered my hidden passion for teaching. Most of all I thank him for believing in me that I was capable of achieving this feat. I would also like to thank my committee members Professors M. Albert Thomas, David A. Haake and Daniel B. Ennis for their guidance and valuable suggestions. It certainly helped make my research more meaningful and worthwhile.

I am very thankful to my lab-mates, especially Artemio Navarro for teaching me everything I needed to know about this lab when I was new to it. I cherish all those times when he taught me how to use each and every equipment in the lab, when we had profound discussions about our career and the future, and when we joked and laughed while working in the lab endlessly! Thank you Sean, Shahzad and Nathan for making all those hours spent in the lab aligning and repeating experiments so much fun and painless! Also thank you Meg, Neha and Priya for always being ready for those quick gossip sessions in between work. It really used to pep me up!

I am thankful to all my roommates and friends in Los Angeles who created a home away from home for me! Surabhi, my first year in LA would not have been as memorable and fun without you. You made me fall in love with LA! Susneha, you have been the elder sister to me that I never had. Varsha, Shalini, Asha ji and Amruta thank you for being such good roommates and friends! Thank you Karyl for being with me throughout even without being in LA! Your friendship helped me sail through countless highs and lows!

Most of all I would like to thank my husband. None of this seems achievable without him by my side. When all I could see was darkness ahead he has been my guiding light. When I was dispirited and dejected he has been my energy and motivating force. He knows how to bring a smile on my face when I need it the most and when I am flying too high in the sky he knows how to bring me down to mother earth and remind me of the arduous journey that lies ahead! Thank you mom and dad for encouraging me and helping me find my dream. I don't think I will be able to express how much your love, care and support means to me!Thank you Savi for being the best sister to me! I don't think anyone tolerates and tackles all my crazy tantrums and weirdness as well as you do! Special thanks to my brother-in-law Sridhar for teaching and helping me with COMSOL when I had no idea how to go about working with it. Thank you mom-in-law and dad-in-law for taking care of me like your daughter. I am forever indebted to you both for all the support and blessings.

# VITA

| | |
|---|---|
| 2003 | Naval Public School<br>New Delhi, India |
| 2009 | B.Tech. Biotechnology<br>Netaji Subhas Institute of Technology (Delhi University)<br>New Delhi, India |

# CHAPTER 1

# Introduction

Chronic wounds and infections place a major burden on the already overwhelmed healthcare system. Care of such chronic wounds is not only a financial burden on the patients, but they also undergo tremendous physical and emotional trauma, which affects their families and in turn the society. Chronic wounds are wounds that have failed to proceed through an orderly and timely process to produce anatomic and functional integrity, or have proceeded through the repair process without establishing a sustained anatomic and functional result [3]. Many diseases associated with chronic infections, such as urinary, dermal and neurovascular diseases are linked to biofilm phenotype bacteria [4]. Contrary to planktonic, single organism infection theory bacteria almost always exist as biofilms. Bacterial biofilms are communal structures of microorganisms encased in an exopolymeric coat that attach on both natural and abiotic surfaces. The sessile bacteria in these biofilms can withstand host immune responses, and are much less susceptible to antibiotics compared to their nonattached individual planktonic counterparts [5].

This chapter will provide a basic understanding of what biofilms are, how they interfere with wound healing; why it is not possible to treat them with conventional techniques used to treat bacterial infections; the current techniques used to tackle bacterial biofilm infections and their shortcomings; it will ultimately focus on the benefits of using Laser Generated Shockwaves as a treatment modality for treating bacterial biofilm infections.

## 1.1 What are Bacterial Biofilms?

Bacterial biofilms as mentioned before are sessile communities of bacteria that are embedded in an exopolysaccharide (EPS) matrix that these bacteria secrete [6]. Biofilms can be found on both biotic and abiotic surfaces. For instance biofilms have been found present in domestic environments including food, laundry and kitchen items; water reclamation systems; medical implants such as catheters; tooth surfaces; urinary tracts; chronic wounds to name a few. Biofilms have also been reported to have colonized metallic surfaces in the presence of toxic chemicals [7].

## 1.2 Structure and Differentiation of Biofilms

Claude Zobell *et al.* were one of the first groups to have observed the preferential growth of marine bacteria on surfaces in 1943 [8]. After several years Costerton and his group extended this observation and noted that bacterial adhesion to surfaces can be found in a variety of microbial ecosystems, including freshwater systems and eukaryotic tissues [1]. Even then as late as 1987 [9] biofilms were perceived as sessile bacterial cells randomly embedded in simple "slabs" of exopolymeric matrix material. In this early biofilm era the most pressing question that was being asked was "How do the bacterial cells that are deeply embedded in the matrix get their nutrition, including oxygen?" The modern era of biofilm began when this question was answered. SCLM images of living biofilm colonies [10] showed that the bacterial cells exist as microcolonies within the matrix interspersed with open water channels. The structure and architecture of these microcolonies and channels depend on the types of bacteria as well as environmental factors such as shear forces acting on the biofilm. The main function of these channels however, is to entrain the water from the bulk phase and deliver nutrients including oxygen to the complex bacterial communities residing deep inside the biofilm. Figure 1.1 shows a

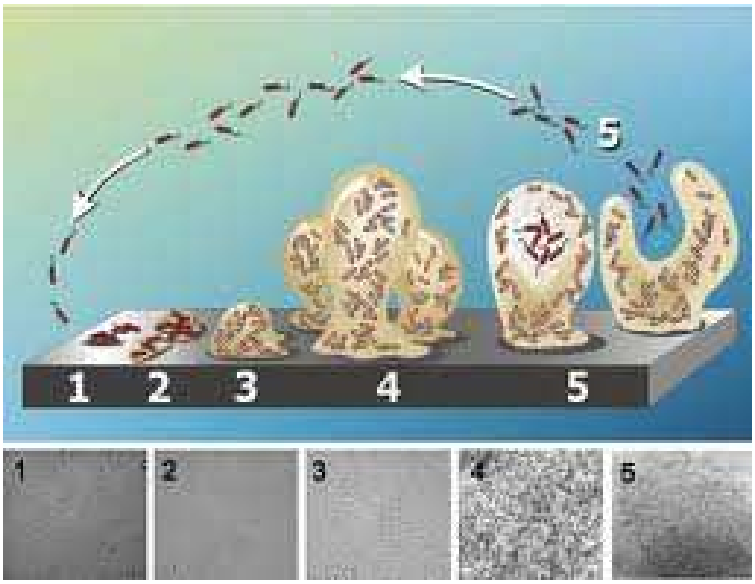


Figure 1.1: Above: Stages of Biofilm Development; Below: Series of computer-assisted compilation of SCLM images of live biofilm colonies. Image taken from http://bacteriality.com

series of computer- assisted compilation of SCLM images of live biofilm colonies as well as a cartoon depiction of the various stages of biofilm development.

## 1.3 Stages of Biofilm Growth and Formation

Biofilm development can be differentiated into at least four distinct stages. These are (a) reversible attachment, (b) irreversible attachment, (c) maturation, and (d) detachment. Detached cells can return to return to the planktonic mode of growth, thus closing the biofilm developmental life cycle. A schematic overview is shown in Figure 1.1.

### 1.3.1 Reversible Attachment

The most common theory of how biofilm formation begins is that initially free-floating planktonic bacteria attach reversibly to solid surfaces or adhere to each other (coaggregate) at surface interfaces i.e. air-water interface through weak interactions via bacterial components like pili or fimbriae [11] [12]. The bacteria continue to exist in the planktonic state and will continue to proliferate at their maximum rate under conditions of nutritional abundance and no chemical or physical environmental stress. However if the bacteria sense any environmental or nutritional stress, they will shift into a biofilm phenotype and begin to secrete various extracellular matrix components [11] [13].

### 1.3.2 Irreversible Attachment

Biofilm formation on the surface can occur by a number of different mechanisms. There are three mechanisms that are most commonly cited in the literature. One is the attached cells redistribute to aggregate around a surface by surface motility [14] [15]. O'Toole and Kolter [16] studied Pseudomonas aeruginosa mutants and suggested that type IV pili-mediated twitching motility plays a role in surface aggregation for this organism. The second mechanism is basically due to binary division of the attached cells [17]. The daughter cells produced by cell division spread outward and upward from the attachment surface to form cell clusters. The third mechanism is the recruitment of cells from the bulk fluid to the growing biofilm [18]. The relative contribution of each of these mechanisms will depend on the organisms involved, the nature of the surface being colonized, and the physical and chemical conditions of the environment [19]. The distinct feature of bacterial biofilms that differentiates them from bacteria that simply attach to a surface is that biofilms contain EPS that surround the bacteria [19]. The EPS aid the bacteria to firmly adhere to the surface, leading to the formation of structured micro-

colonies. Microbial EPS are biosynthetic polymers that can be highly diverse in chemical composition and may include substituted and unsubstituted polysaccharides, substituted and unsubstituted proteins, nucleic acids and phospholipids [20].

### 1.3.3 Maturation

This phase of biofilm development, maturation, results in the generation of complex architecture, channels, pores, and a redistribution of bacteria away from the substratum [21]. In a study by Sauer *et al.* [22] mature biofilms of P. aeruginosa were shown to have a radically different protein profile from planktonic bacteria grown in chemostats.More than 300 of these proteins were found on in mature biofilm samples and not in planktonic bacteria. The proteins were found to be belonging to one of the following categories: metabolism, phospholipid and LPS-biosynthesis, membrane transport and secretion, as well as adaptation and protective mechanisms [22]. Research on the special functions performed by bacteria when in groups has led to understanding of how the bacterial cells function together as a community to form mature biofilms. It has been seen that quorum sensing is an important mechanism for bacteria to communicate with one another to form a mature biofilm [23]. Fuqua *et al.* [23] studied Gram-negative bacteria and found out that acylhomoserine lactone signals are produced by individual bacterial cells. At a critical cell density, these signals can accumulate and trigger the expression of specific sets of genes. Davies *et al.* [21] characterized two P. aeruginosa quorum sensing systems. One, the LasR-LasI system which controls the expression of a host of extracellular virulence factors. The other system RhlR-RhlI is also controlled by LasR-LasI system. The RhlR-RhlI controls genes required for the production of a number of secondary metabolites. RhlI catalyzes the synthesis of butyrylhomoserine lactone, and LasI directs the synthesis of 3-oxododecanoylhomoserine lactone. The wild type, a lasI mutant, and a rhlI mutant all can colonize a glass surface and form microcolonies. Microcolonies of the wild type and

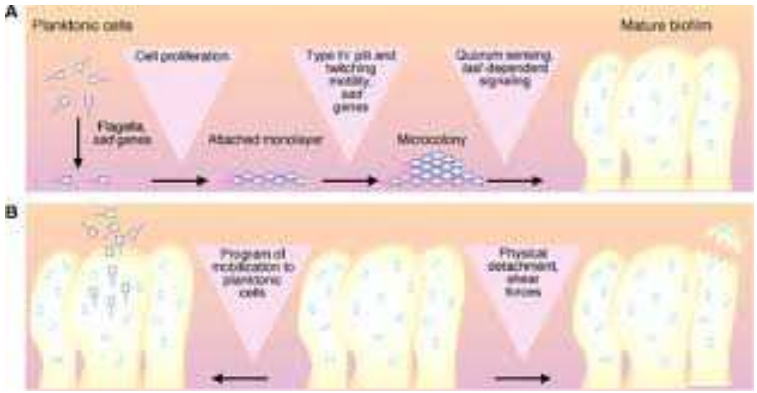


Figure 1.2: Development of *P. aeruginosa* biofilm at a molecular level [1].

the rhlI mutant differentiate into structured, thick, biocide-resistant biofilms, whereas the lasI mutant microcolonies remain thin, undifferentiated, and sensitive to dispersion by a weak detergent (0.2 % sodium dodecyl sulfate). Addition of the missing signal, oxododecanoylhomoserine lactone, to the lasI mutant restores biofilm development.

Figure 1.2 [1] shows the development of P. aeruginosa biofilms at a molecular level. Specific cell surface components are required for adhesion to a surface and additional components are required for aggregation of cells into undifferentiated microcolonies. The generation of a mature P. aeruginosa biofilm requires quorum sensing by way of an extracellular signaling molecule that can be likened to a hormone.

### 1.3.4 Detachment

Detachment is a general term used to describe the stage of biofilm growth in which individual cells or groups of cells separate themselves from a biofilm or substratum. Active detachment is a physiologically regulated event, but only a few studies [24] have been performed to demonstrate a biological basis for this process. The mechanism of detachment is most probably used by bacteria in a sessile biofilm community to colonize new

areas [1]. Pieces of biofilms (Figure 1.2) can break off in the flow and may colonize new surfaces. Furthermore, there may be cues for a program of events leading to the release of planktonic bacteria from a biofilm.

Allison et al. [25] showed that incubation of P. fluorescens biofilms for long periods of time led them to experience detachment, coincident with a reduction in EPS. In Clostridium thermocellum the onset of stationary phase has been correlated with increased detachment from the substratum [25]. There is a growing understanding among biofilm researchers that starvation may lead to detachment by an unknown mechanism that allows bacteria to search for nutrient-rich habitats [16]. Sauer *et al.* [22] compared two-dimensional-gel protein patterns to show that dispersing cells of P. aeruginosa are more similar to planktonic than to mature biofilm cells. This finding indicated that dispersing biofilm cells revert to the planktonic mode of growth; thus, the biofilm developmental life cycle comes full circle. [22].

## 1.4 Why are biofilms harmful?

### 1.4.1 Biofilms - cause of chronic wounds and prolonged infections

Chronic wounds such as diabetic foot ulcers, pressure ulcers and venous leg ulcers contribute to a tremendous increase in healthcare costs [26]. In the United States, $58 billion is spent on dealing with chronic complications associsted with diabetes that afflicts approximately 18 million people [27]. The current treatment for such complications include transiently effective methods and topical application of antibiotics often followed by amputation. It had been estimated in 2007 that nearly $14-24\%$ of all diabetics in the United States will undergo amputation and will consequently suffer its co-morbidities. There is an urgent need for a targeted and effective treatment for such chronic wounds.

Chronic and acute wounds progress through the same stages of healing initially [28]. In a normal wound, the various stages of healing are: hemostasis, inflammation, granulation, epithelislization and maturation [29]. However a chronic wound is not able to resolve the inflammation and the wound remains in a persistent state of “acute” inflammation. A typical chronic wound has prolonged expression of inflammatory cytokines like interleukins (IL - 1) and Tumor Necrosis Factor ( TNF-$\alpha$) [2] [30] [31]. It has become clear over the past few years that bioburden is one of the major causes of chronic wounds [31]. In addition to chronic wounds, biofilm are a major contributor to diseases that are characterized by an underlying bacterial infection and chronic inflammation, eg periodontal disease, cystic fibrosis, chronic acne and osteomyelitis [32] [1] [4].

Contrary to what would generally be expected the inflammation does not harm the biofilm much but instead benefits it. If the biofilm is in close proximity with the host vasculature, by inducing a hyperinflammatory state it will increase capillary permeability, with a sustained release of the intravascular contents; this plasma exudate percolates through the biofilm, providing it with nutrients [33].This ‘parasitic’ strategy for sustaining a chronic infection is observed in biofilm infections such as chronic wounds [33].

Schaber and Rumbaugh [34] studied that a biofilm develops within hours of seeding with planktonic bacteria. Soon after biofilm formation began, bacteria were visualized at the capillary basement membrane of the peri-wound vasculature. Biofilms are well fortified against most immune strategies, so they may select capillary basement membranes as a source of nutrients [33]. It has been seen that coaggregation of different species of bacteria increases the genetic diversity, and thus robustness, of the biofilm, allowing multiple and more flexible biofilm-host interactive strategies [35] [36]. There may be several dozens or even hundreds of different polymicrobial groups that can act in con-

cert, coordinate their combined genetic potentisl and drive a sessile immature biofilm community to produce a clinical biofilm infection. This is termed as synergy.

### 1.4.2 Biofilms are resistant to Conventional Treatment Techniques and Host Immune Responses

Biofilms tremendously increase the tolerance of microorganisms embedded in the EPS matrix to the immune system, anti-microbials and environmental stresses (eg. nutritional or oxygen limitation). This tolerance gives the microbes embedded in the biofilm complete resistance to factors that would easily kill the same microbes when growing in an unprotected, planktonic state [37] [38].

The 3 mechanisms by which biofilms achieve resistance is: Figure 1.3 [39] **Blocking** - The EPS protects the microbes by preventing large molecules (eg antibodies) and inflammatory cells from penetrating into the biofilm matrix. Mature biofilm may also act as a diffusion barrier to small molecules like antibiotics [40].

**Mutual protection** - In a polymicrobial biofilm, the different species of bacteria are capable of cooperating and providing protective effects to each other. For example, antibiotic resistant bacteria may secrete protective enzymes or antibiotic binding proteins that can protect neighboring non-antibiotic resistant bacteria in a biofilm [32]. They are also known to transfer genes to other bacteria that confer antibiotic resistance, even between different species [41]. Studies have also shown that one species can impart specific characteristics to the EPS of biofilms which can play a significant role in the ability of other species to attach and incorporate into an existing biofilm [42].

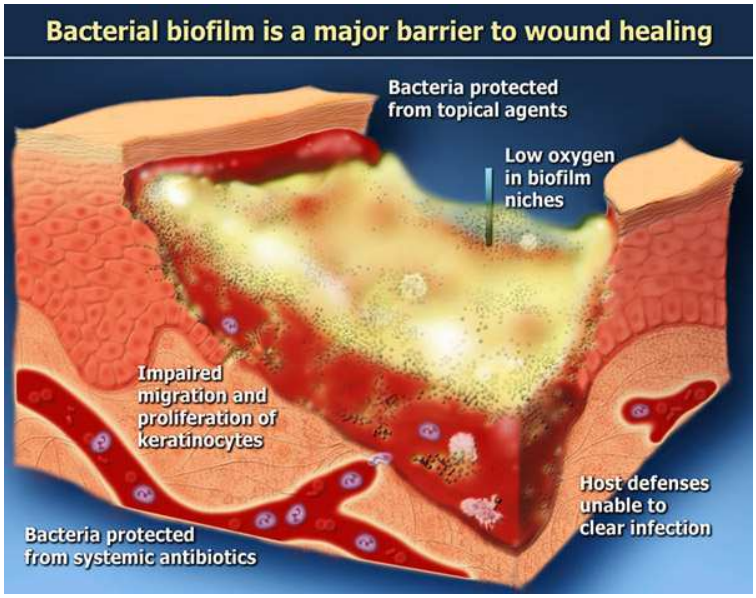


Figure 1.3: Mechanisms by which biofilms achieve resistance [2].

**Quiescence** - Bacteria in biofilms have developed another interesting survival strategy, a sub-population become metabolically quiescent [32] [21] [43]. For antibiotics to act bacteria need to be metabolically active, the quiescent bacteria in biofilms are unaffected by antibiotics that would normally kill active bacteria [32] [44]. Studies has shown that the lowest concentration required to kill or eliminate bacterial biofilm for many antibiotics actually exceeds the maximum prescription levels for the antibiotics [44] [45] [46] [47]. Thus, standard oral doses of those antibiotics, which effectively kill the normally susceptible bacteria when grown planktonically in a clinical laboratory, may have little or no antimicrobial effect on the same type of bacteria in biofilm form in the patient.

Apart from the three factors mentioned above, the increased resistance of bacteria in biofilms to natural antibodies, phagocytic inflammatory cells, antibiotic drugs, antiseptics and disinfectants can be due to several other factors like: highly negatively charged exopolymeric matrix that consists of polysaccharides, DNA and proteins; induced expres-

sion of specific biofilm genes required to produce special efflux pumps in bacterial cell membranes to pump out antimicrobial agents, creation of unique niches in the biofilm where oxygen is limiting or absent [48].

## 1.5 Current Treatment Strategies for Biofilm Infected Wounds

### 1.5.1 Physical

Wolcott *et al.* suggests that physical intervention is vital to the successful management of biofilms [49]. Debridement of the wound reduces the presence of microorganisms and devitalised host components [50]. Debridement helps expose healthy host tissues that are better capable of fighting the bacterial infection. It also helps get rid of the biofilm, but the biofilm has the ability to colonize the wound again, hence debridement alone is not a sufficient technique to get rid of biofilm [51]. Antimicrobial and wound dressing techniques are usually coupled with debridement to make it more effective.

The disadvantages of debridement of wounds is that it is very painful. Debridement of the wound can cause damage to the underlying wound tissue that are trying to heal, worsening the condition of the wound. Also comprehensive debridement is not a completely standardized technique and is heavily dependent on the clinician, though recent patents on wound debridement For example, a patent on the method, device and kit for lesion debridement has been filed which is a step forward in the right direction (US20070135706).

To overcome the disadvantages of debridement alternative methods of debridement are being developed. These include the use of pulsed electrical fields to disaggregate biofilm [US20070239073], use of acoustic shockwaves to eradicate or prevent biofilm formation [US20070239073] as well as the use of ultrasound for debriding biofilm in-

fected wounds [[US20080183109]. Some of these techniques are discussed at length in future chapters.

### 1.5.2 Wound Dressing

Wound dressings are not inherently antibiofilm, but they do help reduce bacterial load and acute infection rates. They act as a physical barrier for the wound surface preventing microbial colonization and in turn biofilm development [52] [53].

### 1.5.3 Antimicrobials

#### 1.5.3.1 Antibiotics

Antibiotics suppress/kill metabolically active cells,in the case of biofilms these cells are the most harmful to the host tissue due to their ability to elicit host inflammation [54]. However, a sizeable portion of the biofilm is composed of dormant cells that do not respond well to antibiotics [55].

Systemic antibiotics are necessary when there is significant wound infection involving deep tissues, or when clinical findings or laboratory markers suggest the infection is systemic [56]. Despite this, systemic antibiotics have been found to be only $25-32\%$ effective against biofilms [56] [57], resulting in only transient suppression of the biofilm at its outermost active edges. The infection often returns after the antibiotic regimen is complete because the antibiotics only suppress rapidly growing cells [58]. Consequently, the recalcitrant biofilm remains and the suppressed cells begin to metabolize rapidly [59]. This recalcitrance of biofilms to antibiotics is not evident in *in vitro* planktonic testing. Treating biofilm infections with antibiotics is even more problematic with

ischemic wounds, since the appropriate level of antibiotic may not reach the infection due to poor blood supply [51].

#### 1.5.3.2 Antiseptic

Topical antiseptics can be used to suppress biofilm formation after the biofilm has been completely removed using debridement and systemic antibiotics since they are known to cause significant microbial death. However, they can cause damage to human proteins like antibodies, cytokines and can even kill human cells [60]. It has therefore been suggested to use antiseptics with caution [61].

#### 1.5.3.3 Ionic Silver

Silver has become increasingly popular in wound care industry since it is seen to exert bactericidal effects at minute concentrations [62]. Some silver dressings have the potential to prevent biofilms in vitro [52]. Laboratory studies have compared silver dressings from different manufacturers, [63] with some positive results on biofilms [64]. There is large variation in the silver content, silver release, and antibacterial activity between various silver containing dressings which makes identifying the most effective dressing for a particular type of wound difficult [65]. Although silver dressings have been demonstrated to be effective against biofilms *in vitro* [66] [64] there exists some speculation as to whether enough silver ions are released from silver dressings to the wound bed in order to treat biofilms present in chronic wounds [67].

#### 1.5.3.4 Iodine

Iodine had been used as a disinfectant for many years. However its efficacy as an anti-biofilm agent is debatable. Also there is growing concerns about its chemical stability and its toxicity to host tissues [60] [68]. Povidone-iodine has been demonstrated as being effective against *Staphylococcus epidermidis* biofilms *in vitro* [69] and may damage host cells less than elemental iodine [70]. Cadexomer iodine has been demonstrated to be effective directly against *Staphylococcus aureus* biofilms textitin vitro [71]. Despite these studies the efficacy of iodine against bacterial biofilms *in vitro* remains to be established.

#### 1.5.3.5 Honey

Honey has been known to have antibacterial and healing properties since long times. *Pseudomonas aeruginosa* and *Staphylococcus aureus* biofilms have been killed using two types of honey, Sidr and Manuka, *in vitro* [72]. Honey might also mediate pro-healing effects on host cells as *in vitro* studies with monocytic cell lines found that honey enhances the release of inflammatory cytokines associsted with innate immunity [73]. It has been suggested that the osmotic potentisl of honey is its key mechanism of action, which may have effects on biofilms, but others suggest that its phytochemicals may be more important [51].

### 1.5.4 Antibiofilm strategies

A number of anti-biofilm agents are available. Some are being used is wound care and others are being investigated *in vitro*. Some of the popular anti-biofilm agents are:

- Lactoferrin

- Ethylenediaminetetraacetic acid (EDTA)
- Xylitol
- Gallium

These agents are not usually detrimental to the microbial cells. They do not affect the growth, reproduction or integrity of the cells. They work by interfering cellular communication, disrupting the intercellular matrix or altering the cellular metabolism [11] [74] [75] [76].

#### 1.5.4.1 Lactoferrin

Lactoferrin is a protein which cause chelating of iron. It is found in most bodily fluids, especially in milk [77]. Lactoferrin has been shown to be effective against both planktonic and biofilm bacteria [78]. The effect of lactoferrin on *Pseudomonas aeruginosa* biofilm was studied *in vitro*. It was seen that lactoferrin prevented the adhesion of bacteria to the surface which is the first essential step in biofilm formation [74]. Lactoferrin also has bacteriostatic effect on bacteria, since it binds to iron[III] depriving the bacterial cells of this essential nutrient [79]. It may also cause bacterial membrane permeabilization [80]. Since lactoferrin is broad spectrum and works in a non-specific manner it has been used to control *in vitro* biofilms like periodontal pathogens [81] and cystic fibrosis-associsted pathogens [82]. It has also been used in clinics as a part of a comprehensive treatment regime to manage biofilm associated ischemic wounds [49].

#### 1.5.4.2 EDTA

Ethylenediaminetatraacetic acid [EDTA] is a polyaminocarboxylic acid that chelates metal ions like calcium[II] and iron[III]. EDTA has been used as an antibacterial for more than 40 years. It kills microbes primarily by chelating iron and interfering with iron[III]- dependent biological pathways in bacteria [83]. Disodium EDTA has been demonstrated to kill clinical isolates of S. epidermis and to prevent attachment of bacteria to catheter segments *in vitro* [84]. Tetrasodium salt of EDTA has been studied to have a broad spectrum effect against biofilms *in vivo*. It was seen that 40 mg/ml tetrasodium EDTA was effective in removing biofilm after 24 hours of incubation [85] [86]. Martineau and Dosch [87] recently showed that including tetrasodium EDTA into a wound gel enhanced its antibiofilm properties on *P. aeruginosa*. However concerns on the effect of EDTA on host cells still persist.

#### 1.5.4.3 Xylitol

Xylitol, a five-carbon alcohol sugar, is a naturally occurring substance commonly used in chewing gum, and can reduce the incidence of dental carries. Most of the research concerning antimicrobial properties of xylitol has been on dental biofilms [88]. Xylitol was then subsequently used in the nasal passage and it was shown to inhibit bacterial adhesion to the nasal mucosa and lead to the patent submission for a xylitol-based nasal spray [US20016258372]. Katsuyama *et al.* demonstrated that xylitol when used with farnesol synergistically inhibited biofilm formation in patients with atopic dermatitis [89]. In this study, xylitol inhibited biofilm formation of *S.aureus* cultures from healthy human and patients with atopic dermatitis.

## 1.6 New Mechanical Approaches to Combat Biofilm Infected Wounds

Mechanical debridement of the wound to get rid of biofilm appears to be the method of choice for combating biofilm infections in wounds at present. As seen in the previous sections, debridement is capable of getting rid of the biofilm from wound surfaces more effectively than any other method like the use of antibiotics or antiseptics. In addition to being very effective they eliminate many problems associsted with other techniques like for instance the development of antibiotic resistance with the indiscriminate use of high doses of antibiotics or the harmful effects on the host cells due to the use of strong antiseptic chemicals to get rid of the biofilm. However, mechanical debridement of the wound has its own problems such as the method being very painful as such also unless performed by a skilled physicisn it could lead excision of healthy tissues underlying the wound bed.

In the recent past many groups are working on developing alternative mechanical approaches to delaminate biofilm off wound surfaces. The emphasis is on making the process less painful and more specifically target the biofilm present on the wound surface and not the host tissue below it. Some of the mechanical approaches being worked on recently include:

- US (Ultrasound)
- ESWT (Extracorporeal Shockwave Therapy)
- LSGT (Laser Generated Shockwaves Therapy)

### 1.6.1 Ultrasound

Therapeutic ultrasound techniques use power densities below 500 mW/$cm^2$. These power densities are calculated by averaging the beam power over the area of incidence and over the pulse repetition period. At these intensities studies ultrasound is known to interact with cell membranes through non-thermal effects such as cavitation and microstreaming [90]. Cavitation is the phenomenon in which the pressure field due to acoustic waves causes the expanding and compressing of air-bubbles. Microstreaming is the process by which fluids move along membranes causes by pressure gradients. These mechanical effects have been shown to increase angiogenesis, which is beneficial for wound healing [91]. In this study, Young et al. showed that when two groups (one control) were exposed to ultrasound at frequencies of 0.75 MHz and 3.0 MHz for 5 min (pulsed 2 ms on and 8 ms off) a day at an intensity of 100 mW/$cm^2$, corresponding to a total energy flux of about 30 J/$cm^2$ per day or 150 J/$cm^2$ for the five-day period, they reported greater formation of new blood vessels within five days of the ultrasound treatment. Since ultrasound promotes angiogenesis it has been shown to be helpful in aiding new bone formation and treatment of diabetic foot ulcers [92] [93].

At lower frequencies, Pitt *et al*. [94] showed that ultrasound treatment increases the growth of bacteria such as *Pseudomonas aeruginosa* and *Staphylococcus epidermidis*.These bacteria were exposed to ultrasound waves at an intensity of 2 W/$cm^2$, frequency of 70 KHz for 48 hours. The pulse duration was 100 milliseconds and repeated every 500 milliseconds. Carmen *et al.* [95] hypothesize that the reason for the increased growth might be that ultrasound at these frequencies increased permeability of the cell membranes, thereby increasing diffusion of nutrients which enhances bacterial growth.

US waves when applied at high intensities and frequencies have antibacterial effects which are being used in the food industry as well as for water decontamination [96] [97].

High intensity US therapy has also been used to combat infections in joint prostheses, by adding gentamicin to the region where US waves are applied [98] [99]. However recent studies on biofilm destruction with US alone have shown that ultrasonic waves at high frequencies are unable to kill the bacteria in the biofilm, but are able to perform tissue damage [100]. Studies have shown that, when exposed to low levels of US (lower than bactericidal level) bacteria adapt to US exposures by producing a stronger biofilm, which gives them higher resistance to further therapeutic actions [101].

### 1.6.2 Extracorporeal Shockwave Therapy (ESWT)

Extracorporeal Shock Wave Therapy (ESWT) has been the gold standard to fragment renal calculi (‘kidney-stones") using lithotriptors [102]. Extracorporeal shockwaves have peak compressive pressures of up to 100 MPa. These pressure waves travel through fluid and tissue mediums and their mechanical effects are mainly due to impedance mismatches [103]. These waves alos exhibit negative pressure of around 5 - 10 MPa, which cause the formation of cavitation bubbles. These bubbles also help in fragments the kidney stones [104].

ESWT technology has been used in the field wound care and has been seen to stimulate the regeneration of tissue [105] [106]. Studies using ESWT show an increase in increase bone formation and healing of soft tissue overlying the bones [107]. The treatment resulted in bone unification and decrease in symptoms for 75.7% of the patients who suffered from non union of bones. Studies show that low doses of ESWT increased angiogenesis and epithelialization [108] [109]. In addition to having wound healing capabilities, ESWT is also seen to have antibacterial effects. Gerdesmeyer et al. showed reduced growth of *Staphylococcus aureus* when the bacterial colonies were subjected to 4000 impulses at 2 Hz with a pulse energy flux of 59 mJ/$cm^2$ [110]. Many other stud-

ies [111] [112] show that high energy extracorporeal shockwaves do exhibit an antibacterial effect. However, the antibacterial effects have been studied only on planktonic cells.

Experiments to remove biofilm from the surface of the teeth using ESWT showed that though some of the biofilm did come off, there was no effect on the visibility of the collected bacteria [113]. However, most of the studies carried out to eradicate biofilm off surfaces have been performed *in vitro* [114] and so the effect of these shock waves on host tissue *in vivo* has not yet been examined. In addition it has been seen that extracorporeal shock waves alone is not sufficient to eradicate biofilm, it requires the concomitant use of antibiotics to get rid of them completely [115].

## 1.7 Laser Generated Shockwaves (LGS)

LGS (Laser-Generated Shockwaves) are exclusively compressive waves, unlike ESW and US waves which have a tensile component. Therefore the primary mode of action for LGS is not cavitation.

LGS are being used in cataract surgery for extraction and photolysis of the lens and for prevention of secondary cataract formation [116]. LGS was found to be better than US waves since it produced no clinically significant heat at the site of incision, thus avoiding any sclera burns during cataract surgery [117].

Studies have shown that LGS treatment increases cell and skin permeability which can be helpful for macromolecule and gene delivery [118] [119] [120] [121]. LGS has also been shown to increase the permeability of bacterial biofilms [122] [123]. Parameters such as rise time, pulse duration and number of pulses determine the permeability of

cells as well as biofilms caused by LGS [124]. Doukas *et al.* [125] showed that stress wave gradient had a greater effect on cell visbility than the peak stress of the wave. However, the exact effect of each of these parameters on biofilm permeability is yet to be determined.

Krespi et al. [126] disrupted Pseudomonas biofilms *in vitro* using LGS on various targets such as culture plates, stainless steel screws, sutures and tympanostomy tubes. Nd:YAG laser pulses between 4 ns and 8 ns duration and 8 mJ and 12 mJ energies were focused vis an optical fiber onto a Ti target immersed in a low-streaming liquid inside a hollow cylindrical probe. The generated stress waves were made incident on biofilm. It was reported that 10 to 20 stress waves, each with an amplitude of $0.8-1$ GPa were needed to break away chunks of the biofilm from these substrates. Their results showed that the biofilm can be pried off from the surface without any visual damage to the underly host structure and that with each stress pulse, the biofilm becomes more permeable [127]. The permeability of the biofilm structure would allow the addition of antibiotics to the coupling medium. In fact, when shockwaves are coupled with antibiotics, there is a reduction in bacterial visbility [128]. It is suggested that LGS with fast rise times increase the permeability of the cell membrane without killing the cells.

## 1.8 The Laser Spallation Technique (LST)

This section describes the process by which laser energy is converted to a mechanical shockwave which causes spallation of thin films. When laser pulse is made incident on a thin metallic film, the laser energy ablates the thin metallic film, causing a rapid thermal expansion of the film resulting in a compressive wave propagating through the substrate. The laser fluence, pulse width, and the substrate material properties contribute

to the temporal characteristics of the stress wave. Gupta *et al.* [129] [130] [131] [132] [131] [133] optimized the laser-generated stress wave profiles for measuring the tensile strength of a thin film interface. High strain rate loading ( $10^7 s^{-1}$) in these processes, suppress all inelastic effects during interface decohesion, and thus, the measured strengths are intrinsic and related directly to the atomic microstructure and chemistry of the interfacial region. This was shown by Yuan *et. al.* [134] by measuring the tensile strengths of Nb/sapphire interfaces whose structure and chemistry were characterized using high resolution transmission electron microscopy and modified by a combination of heat treatment and deposition of 5 to 40 Åthick interlayers of Cr and Sb. Similarly the effects of the Nb deposition mode (RF vs. DC), grain scale substrate roughness, and substrate orientation (prismatic vs. basal) were systematically studied [135], with the sensitivity of the experiment in capturing the influence of the substrate orientation realized in terms of unique spallation patterns that in turn could be directly related to interfacisl atomic arrangement. Thus, atomic scale tailoring of the interfacisl region for either maximizing or reducing adhesion can be accomplished. Using this technology, interfacisl strengths in the range of 0.1 GPa (14.5 ksi) to 2.5 GPa (362 ksi) have been measured in a variety of engineering systems (paints, multilayer electronic devices, engines, tribology) involving metal, ceramic and polymeric coatings deposited on metal, semiconductor and ceramic substrates.

In the Laser Spallation experiment, a $3-6$ nanosecond (ns) long Nd:YAG laser pulse is made incident over a 3 mm diameter area on a 0.5 $\mu$m Titanium (Ti) film sandwiched between the back surface of a glass slide and a 50 to 100 $\mu$m thick layer of water glass ($SiO_2$) [U.S. Patent 5; 438; 402] as shown in Figure 1.4. The melting-induced expansion of Ti under confinement generates a compressive stress wave (with sub-nanosecond rise-time) directed towards the test coating, which is deposited on the substrate's front surface. The compression stress pulse reflects into a tensile wave from the coating's

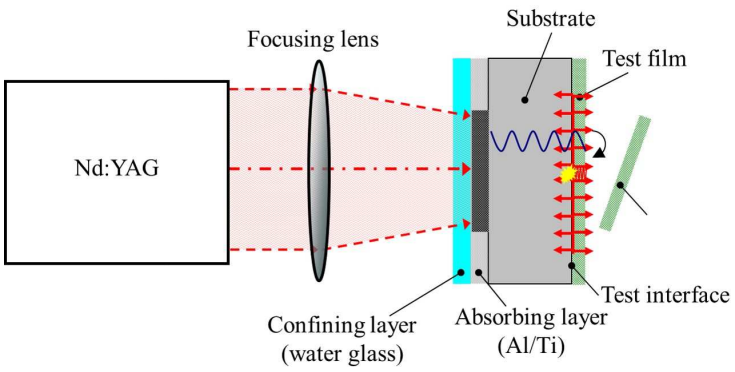


Figure 1.4: The Laser Spallation Experiment

free surface and leads to its spallation (complete removal) at a sufficiently high amplitude. Thus the required minimum laser energy to cause the spallation is determined as the minimum energy required to generate a stress pulse with sufficient peak stress that overcomes the adhesive strength of a material interface. The LST also incorporates a Michealson displacement interferometer to measure the free surface displacement as the wave propagates towards the free surface. The displacement can be ultimately used to find out the input stress generated by the Ti film. The next section will discuss new modifications to the LS technique and details of the displacement interferometer and subsequent calculation of input stresses.

### 1.8.1 Modified Laser Spallation Technique (MLST): 'Top - Down' Setup

The current study involves the use of biological samples which are coupled to the shockwave generating apparatus with a liquid. The system described in the previous section can not be used for this study since the laser shockwaves were generated horizontally and the sample was placed vertically. A new 'Top-Down setup was designed to allow for the laser pulse to be applied from the top, while a more compact displacement interferometer is placed under the sample to measure the surface displacement. The displacement

interferometer is based on a Michelson Interferometer [136], as shown in Figure 1.5.

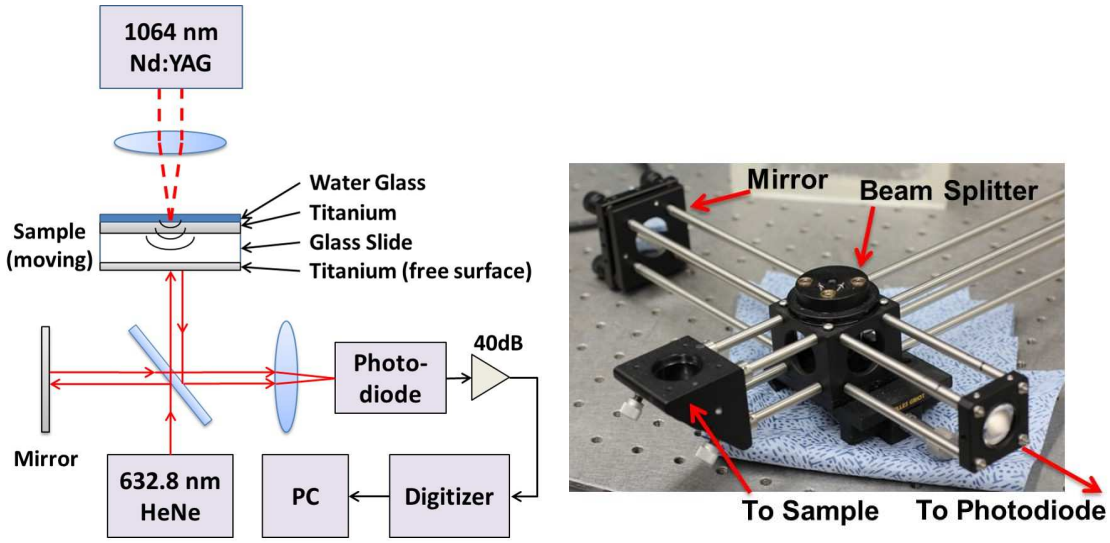


(a) Schematic Diagram of Interferometer (b) Actual Interferometer

Figure 1.5: Figure showing a) Schematic Diagram of the Interferometry Set Up b) Actual Interferometer

In this newer setup, 0.5 $\mu$m of Titanium (Ti) was used as the absorbing layer instead of Aluminium (Al), since Ti is more biocompatible [137]. The Ti film is sandwiched between a glass slide on one side and a layer $15-20$ $\mu$m of water glass on the other. The free surface of he glass slide is coated with 0.04 $\mu$m Ti and acts as the "sample arm" of the displacement interferometer. On the free-surface end a 632.8 nm frequency stabilized laser goes through a 50 : 50 beam splitter, separating one arm of the interferometer toward a reference mirror and the other arm towards the sample. The beams then recombine and are focused by a lens onto an ultra high-speed photodetector (Hamamatsu MSM-64178). As the laser ablates the absorbing layer, a compressive wave is generated and propagates toward the free surface and as a result, the surface displacement offsets the sample arm, causing a varying phase shift in the signal measured. The signal is recorded by a high speed waveform digitizer (Tektronix SCD1000) in single-shot mode with a 0.2 ns in temporal resolution and dynamic rise times of up to 5 ps. The typical

signal is an oscillating pattern, with the peaks corresponding to constructive interference and troughs corresponding to destructive interference. The resulting waveform measures the output voltage and time from the photodetector. The photodetector outputs the voltage amplitude $A_0$(t) recorded by the digitizer and can be expressed in terms of the free surface displacement $u_0$(t).

$$A_0(t) = \frac{A_{max} + A_{min}}{2} + \frac{A_{max} - A_{min}}{2} sin(\frac{4\pi}{\lambda} u_0(t) + \delta)d \tag{1.1}$$

Where $t$ is the time, the $A_{max}$ and $A_{min}$ are the global maximum and minimum fringe amplitudes, respectively, $\lambda$ is the wavelength of frequency stabilized laser (632.8 $nm$) and $\delta$ is the a phase angle in radisns. The free surface velocity can be calculated by differentisting the free surface displacement, $u_0(t)$.

### 1.8.2 1-D Wave Propagation Theory

The stress corresponding to a particular laser energy can be calculated by first experimentally measuring the transient displacement history of the substrate free surface as shown in Figure 1.4 and then using the 1-D wave propagation theory to deduce the value of stress.

According to the longitudinal wave propagation theory, the particle displacement and velocity of any point in the substrate can be assumed as:

$$u(x,t) = u_s(t + \frac{x}{c}) + u_s(t - \frac{x}{c}) \tag{1.2}$$

$$v(x,t) = v_s(t + \frac{x}{c}) + v_s(t - \frac{x}{c}) \tag{1.3}$$

where the subscript $s$ represents the substrate and $c$ is longitudinal wave velocity in the substrate and is assumed to be constant. Under plane strain and one dimensional wave

propagation assumptions, the strain and stress along $x$-axis can be presented as:

$$\epsilon(x,t) = \frac{\partial u}{\partial x} = \frac{1}{c}\left[v_s(t+\frac{x}{c}) + v_s(t-\frac{x}{c})\right] \tag{1.4}$$

$$\sigma(x,t) = (\lambda+2\mu)\frac{\partial u}{\partial x} = \rho c\left[v_s(t+\frac{x}{c}) + v_s(t-\frac{x}{c})\right] \tag{1.5}$$

where $\lambda$ and $\mu$ are the Lamé constants and $\rho$ is the density of the substrate. Using the boundary condition at the free surface:

$$\sigma(0,t) = 0 \tag{1.6}$$

$$v_0(t) = v(0,t) = 2v_s(t) \tag{1.7}$$

where $v_0(t)$ is the transient velocity of the free surface obtained by the interferometry. Finally, the compressive stress generated can be derived and expressed as:

$$\sigma_i = \sigma(h, t-\Delta t) = -\frac{1}{2}\rho c v_0(t) \tag{1.8}$$

The stress wave generated propagates as a one-dimensional planar wave over a cylindrical region. If the ratio of the dismeter of the laser spot size to the laser propagation distance is atleast 3 [138], then under lateral constraints, the stress pulse will propagate under unisxisl strain conditions and the wave velocity $c$ in 1.8 can be related to the Lamé constants $\lambda$ and $\mu$ by:

$$c = \sqrt{\frac{\lambda+2\mu}{\rho}} \tag{1.9}$$

where $\lambda$ can be related to the Young's modulus $E$ and the shear modulus $\mu$ to Poisson's ratio $\nu$.

The free surface displacement function $u_0$ from Equation 1.1 and corresponding free surface velocity can be expressed as:

$$u_0(t) = \gamma\left\{-\alpha[e^{-t/\alpha}-1] + \beta[e^{-t/\beta}-1]\right\} \tag{1.10}$$

$$v_0(t) = \gamma\left\{\alpha e^{-t/\alpha} + \beta e^{-t/\beta}\right\} \tag{1.11}$$

Therefore, the generalized expression to fit the raw waveform from the photodector can be determined by combining equation 1.1 and equation 1.11 to get:

$$A_0(t) = \frac{A_{max} + A_{min}}{2} + \frac{A_{max} - A_{min}}{2} sin(\frac{4\pi}{\lambda}\gamma\left\{-\alpha[e^{-t/\alpha} - 1] + \beta[e^{-t/\beta}) - 1]\right\} + \delta) \quad (1.12)$$

The function 1.12 is the complete function required to fit the raw waveform obtained from the photodetector. For a unique solution the six constants $\alpha$, $\beta$, $\gamma$, $A_{max}$, $A_{min}$, $\delta$ must be determined and fitted to the data. This method is very tedious and a different strategy is used to determine the peak stress. The raw data was used to obtain the time points of the peaks and troughs of the fringes. The distance between each peak to trough is $\lambda/4$, where $\lambda$ is the wavelength of the HeNe frequency stabilized laser of 632.8 $nm$. After obtaining the displacement and the corresponding time values, OriginPro 8 was used to fit the displacement 1.10 vs. time plot to obtain the constants $\alpha$, $\beta$, $\gamma$. The stress generated in the substrate can be directly calculated by combining equations 1.8 and equations 1.11 and the fitted constants as:

$$\sigma_i = -\frac{1}{2}\rho c\gamma\left\{\alpha e^{-t/\alpha} + \beta e^{-t/\beta}\right\} \quad (1.13)$$

# CHAPTER 2

# Determining Delamination Threshold of Biofilm using Laser Generated Shockwaves

In the previous sections it was seen that the mechanical methods of disrupting biofilms from their surfaces were the most effective. Apart from debridement of the wound, other mechanical techniques like the use of US (Ultrasound) and ESWT (Extracorporeal Shock Wave Therapy) are being explored. This thesis explores the use of LGS (Laser-Generated Shockwaves) to delaminate biofilm off surfaces. In order to delaminate the biofilm from the surface it is attached to, it is important to have an understanding of how strongly the biofilm is attached to the surface. With that knowledge we can develop techniques to use just the right amount of force to delaminate the biofilm and cause minimal damage to the underlying wound bed.

## 2.1 Introduction

This chapter focuses on measuring the adhesion strengths of *S. epidermidis* biofilms cultured on polystyrene petridishes that have not been treated. Microscope glass slides were used as the substrate to produce the shockwaves because of their ability to generate very high compressive stress. They are also known generate rarefaction shocks under higher stress loading [136], thereby allowing for the measurement of adhesion strength of very thin interfaces. The modified Laser Spallation Technique will be used to measure the

adhesion strength of the biofilm to the surface of the petridish.

## 2.2 Materials and methods

### 2.2.1 Sample Preparation: Bacterial Stock

*S. epidermidis* (ATCC #35984, Strain Designation: RP62A) was used to produce biofilm for the experiments. These bacteria produce an extracellular polysaccharide adhesin which is responsible for the virulence in S.epidermidis. A stock of the bacteria in glycerol solution was prepared and stored in a (−80°C) freezer.

### 2.2.2 Sample Preparation: Culturing Biofilm on Polystyrene Petridish

A small amount of bacteria was taken from the bacterial stock and added to a 50 mL test tube containing 40 mL of TSB. The test tube was placed in an incubator at 37°C for 24 hrs to culture the bacteria. The cell density of the bacterial stock was measured using a spectrometer (Biocompare Ultrospec 10 Cell Density Meter) at 600 nm.

### 2.2.3 Sample Preparation: Sputtering Ti film on Glass Slide

Microscope slides (soda-lime glass) 3 x 1 inch by 1 mm thick were RF sputtered (Denton Discovery II 550) with 0.5$\mu$m of Titanium (Ti). A uniform layer of waterglass ($SiO_2$) was then spin-coated on top of the Ti to achieve a uniform layer of 15-20$\mu$m. The waterglass layer acts as the constraining layer and is transparent to the Nd:YAG laser wavelength of 1064 nm.

### 2.2.4 Experimental Procedure

After 24 hour growth, the petridishes with bacterial biofilm culture were washed 5 times with phosphate buffer saline (PBS) [139]. Washing with PBS helps get rid of any non-adhering bacterial cells. The biofilm was then stained with Alcian Blue. Alcian Blue stains acidic polysaccharides which are produced by bacteria in the biofilm. The stain helps visualize the biofilm using light microscopy. The following is the method to prepare Alcian Blue and use it for staining [140]:

1. 1g of the Alcian Blue Kit (SGX) was mixed with 3% acetic acid solution until a stable pH of 2.5 was achieved.

2. 1 mL of the Alcian Blue stain was evenly spread onto each petridish and the petridish was gently moved to uniformly distribute the Alcian Blue.

3. The petridish was let to stand for 30 minutes to allow the Alcian blue to bind with the polysaccharides in the biofilm.

4. The petridish containing the biofilm was then washed 3 times with distilled water to remove any unbounded stain.

The petridish was then placed over a water reservoir as shown in Figure 2.1. The Ti sputtered glass slide was placed over the biofilm in the petridish, using two tapes approx 1 mm thick. The tapes were placed at the end of the glass slides which also helped maintain a constant distance between the biofilm and petridish where PBS could be added as a coupling agent. No air bubbles were allowed in the coupling medium. This was very important as the fluid and air interfaces have a large impedance mismatch. Consequently any air interfaces could lead to reflections of the incoming compressive shockwaves. The samples were then ready for LGS treatment.

A 2$\sim$6 nanosecond long 1064 nm Nd:YAG laser pulse was made incident over a $\sim$3 mm dismeter area on the Ti film that was sandwiched between the glass slide and a layer

of waterglass. The absorbed laser energy causes volumetric expansion of the Ti due to the generated plasma and the confinement of the Ti between the two layers leads to generation of a compressive shock wave directed towards the water and the biofilm. In order to find the amount of laser energy used per pulse, the beam is made to go through a 60-40 beam splitter where 60% of the energy goes to the sample and 40% goes to an energy meter to measure the energy. Using the value of the reference energy, the energy to the sample can be calculated. The threshold energy fluence, or the amount of laser energy per pulse needed to delaminate the biofilm, was determined by starting from the lowest energy of and increasing the laser energy by the minimum resolution of the laser i.e 2 - 5 mJ per pulse. The laser energy was varied from 77 - 640 mJ per pulse. The spot size was maintained at 3 mm diameter. After LGS treatment the samples are viewed under a standard light microscope.

### 2.2.5 Qualitative Results: Light Microscopy

Figures 2.2, 2.3 and 2.4 shows the effect of increasing the energy of LGS on biofilm delamination. Images of the delaminated biofilm were acquired using a color CCD camera (Motic 2.0) under 4x magnification. It can be seen that samples treated with higher energy have much larger area of delamination. This is because more area under the stress of the shockwave has enough tensile stress to cause delamination of the biofilm from the surface of the petridish. Uniform delamination of biofilm could not be achieved since biofilm is inherently non uniform. Different regions of the biofilm with different thicknesses will require different amounts of tensile stress to be delaminated.

30 mJ/$mm^2$ was seen to be the threshold energy required for delamination of the biofilm. Delamination was evident across 24 hour to 72 hour growths. Some effect of cavitation bubbles causing small regions of delaminations around the central delaminated regions could also be seen. The stress corresponding to the threshold energy was

measured using a displacement interferometer.

Though the area under the shockwave has 3 mm dismeter, maximum delamination can be observed at the center. This is because as the stress wave propagates viscous forces reduce the particle displacement as the shockwave travels through the medium. Consequently the stress profile varies radislly away from the center. For the purposes of measuring the adhesion strength, maximum particle displacement was captured during interferometry.

### 2.2.6 Cavitation Phenomenon

Small areas of delamination were observed around the main region of delamination as can be seen in Figures 2.2, 2.3 and 2.4. These small areas of delamination is caused by cavitation bubbles. They are generated due to the large impedance mismatch between the water and glass interface. These bubbles are seen to cause delamination on the order of the dismeter of the bubbles. Chapter 3 will discuss the results of a high-speed imaging system built to get a better understanding of phenomenon of formation of cavitation bubbles.

## 2.3 Shock Wave Characterization by Modified Laser Spallation Technique (MLST)

MLST was used to find out the stress corresponding to the threshold energy that caused delamination of the biofilm. The value of stress obtained is the compressive stress generated by the glass slide. The input stress corresponding to 7 energy levels were found out. Using MLST, the input compressive stress to the petridish was also found out. This

helped find out how much compressive stress propagated through all the mediums. As discussed in Chapter 1, the MLST technique and theories of 1 D wave propagation was used to find the input stresses.

### 2.3.1 Shockwave Characterization: Glass

The stress generated by the Ti film sandwiched between the glass slide and the water-glass was determined using the displacement interferometer.

### 2.3.2 Materials and Methods

A glass microscope slide (3 inch by 1 inch by 1 mm thick) is used as shown in Figure 2.5. One side of the slide was RF sputtered with a 0.5$\mu$m thick layer of Ti. A $15-20\mu$m water glass layer was spin-coated over the Ti film. The waterglass acts as a constraining layer during the melting induced expansion of the Ti film. This confinement helps generate the compressive shockwave. At the bottom of the glass slide, a 0.04$\mu$m layer of titanium was sputtered. The thin Ti film at the bottom of the glass slide acts as a reflective layer. It also functions as the sample arm in the interferometery setup. The thin layer of Ti does not affect the shockwave propagation as its thickness is smaller than the spatial disturbance of the shockwave. The amount of time it takes for the shockwave to propagate through 0.04$\mu$m thick Ti is approximately $7-9$ ps. That is 1000X smaller than $2-6$ ns, the rise time of the generated shockwaves. The samples were prepared just like the samples used in the biofilm delaminations experiments. The interferometry system was shown earlier in Figure 1.5. Data was acquired for 200 ns with 1024 points, with a time resolution of $\sim$0.2 ns. The sharp rise time of the stress pulse was captured with the resolution. The raw interferogram data was transferred to other softwares for waveform fitting and cal-

culation of input stress.

### 2.3.3 Interferometry Results

The displacement, velocity, and stress profile were plotted for the 7 energy levels used in the biofilm delamination experiment. Figure 2.6 shows interferogram fits for 4 of the 7 energy levels. The wave arrives at ∼465 ns when lower energies are used. As the energy increases the time of arrival is earlier. This is due to the increase in the shockwave pressure. In each of those plots, the first several fringes from the interferogram fit well on the curve generated to fit the interferogram. After that the fit deviates from the interferogram curve. The deviation begins roughly after ∼50 ns from the first peak. Since most of the displacement information occurs within the first ∼ 20 ns, this deviation from the curve fitting does not affect the final results.

Observing the interferograms at energies of 46 $mJ/mm^2$ and higher, the fringes begin at a lower frequency in the first fringe. Then high frequency fringe pattern is observed for 10-15ns, and then the fringes are seen to trail off (Figure 2.6(d)). This phenomenon is an inherent quality of stress waves generated by glass due to the fact that glass becomes more compressible at higher stresses. Since the glass becomes more compressible, the rise time tends to be longer. It can be seen that the fit data presented in Figure 2.6(d) does not match with the interferogram curve. This is because the sample vibrates when the LGS is generated and propagates through it. Ideally if the interferometer system is free from vibrations both due to the environment and due to the shock loading, the waveform amplitude of the interfergram and the fitted curve would be the same. This anomaly does not however affect the calculation of the peak stress of the LGS. This is because the calculations for the peak stress is based on the peak and trough time positions which is still matching for both the interferogram and fitted curve.

Figure 2.7 shows the total displacements and surfaces velocities measured using the MLST. The displacement and velocity profiles are determined by putting in the fitting parameters presented in Table 2.1 into equation and equation, respectively. It can be seen that most of the displacement occurs within the first 20 ns (Figure 2.7(a)). At higher energy fluence (93mJ/$mm^2$) the total displacement ranges from 0.35$\mu$m-3.89$\mu$m and the corresponding velocities range from 15 m/s - 186.1 m/s. The stress at various energies can be seen in Figure . As can be seen from stress plots, the rise time of the shockwave is quite consistent at around 6-8 ns. The total pulse duration is usually less than 70 ns. The peak stress however varies widely with varying energy levels. It ranges from 120 MPa at 11 mJ/$mm^2$ to 1.4GPa at 93mJ/$mm^2$. Free surface velocities of the glass range from 15 m/s to 190 m/s. The total displacement of the glass slide has a maximum of $\sim$ 4 $\mu$m. At lower energies the time taken to reach the peak stress i.e. the rise time is $\sim$6 ns, while at higher energies, particularly 93 mJ/$mm^2$, the rise time is $\sim$9 ns. The plots show a sharp rise in pressure till about 8 ns, after which the pressure levels and drops sharply for $\sim$60 ns. In the study by Gupta *et al.* [136], the increase in fringe frequency shows an increase in velocity and stress, and the decrease in fringe frequency corresponds to a sharp decrease in velocity and stress due to rarefaction shock produced in glass. This effect is because of increased compressibility of glass under higher pressure gradients as mentioned earlier. Figure 2.7(b) shows the peak stresses for all the 7 laser energies.

As can be seen from the graphs, the peak stress corresponding to the energy fluence that caused delamination of the biofilm i.e. 30 mJ/$mm^2$ is 391.6 MPa. This is however the peak stress generated at the interface of glass and the coupling medium (water). It is not possible to find out the peak stress generated at the biofilm-petridish interface using this experimental set up, since biofilm cannot be made reflective. As can be seen from the experimental set up in order to find out the peak stress generated at any surface in this experiment that particular surface needs to be made reflective which then act as one

of the arms of the interferometer.

In order to determine the peak stress generated at the biofilm-petridish interface a 1-D Analytical model was created by a senior graduate student in the lab (Artemio Navarro). He modeled the propagation of Laser Generated Shockwaves through the coupling medium, biofilm and the underlying petridish. The details of the model can be seen in his dissertation [141]. According to the model, a peak stress of 391.6 MPa lead to a peak stress of 22.86 MPa at the biofilm-petridish interface. Hence, the delamination threshold for biofilm is 22.86 MPa.

## 2.4 Conclusions

This chapter describes the set of experiments conducted to determine the threshold energy that causes delamination of biofilm from the surface of petridishes in which the

Table 2.1: Curve fitting parameters '$\alpha$','$\beta$' & '$\gamma$' for glass and polystyrene. These parameters are used to define the displacement function 1.10 and to calculate the input stress function 1.8.

| | | Energy Fluences $[mJ/mm^2]$ | | | | | | |
|---|---|---|---|---|---|---|---|---|
| | | 11 | 14 | 30 | 46 | 59 | 75 | 93 |
| Glass Slide | $\alpha$ | 8.6 | 8.6 | 8.6 | 8.6 | 8.996032 | 7.87 | 7.87 |
| | $\beta$ | 8.3 | 8.3 | 8.3 | 8.3 | 8.35249 | 7.37 | 7.35 |
| | $\gamma$ | 1150 | 2500 | 4000 | 5450 | 3244.239 | 7000 | 7400 |
| Polystyrene | $\alpha$ | 33.16 | 33.15806 | 33.16 | 33.16 | 33.16 | 33.16 | 33.16 |
| | $\beta$ | 4.367 | 4.36725 | 4.37 | 4.37 | 4.4 | 4.37 | 4.37 |
| | $\gamma$ | 26 | 29.8 | 39.5 | 55 | 58 | 65 | 68 |

biofilm was cultured. In addition the peak stress corresponding to the energy that causes the delamination was also determined by performing interferometry experiments and analytical 1D modeling.

The threshold laser fluence that causes biofilm delamination from the surface of petridishes was found out to be 30 mJ/$mm^2$. The peak stress corresponding to this energy fluence is 391.6 MPa. However as explained in the chapter this peak stress is that which occurs at the glass/water(coupling medium) interface. Using analytical 1D modeling the peak stress at the biofilm/petridish interface was determined to be 22.86 MPa. Hence, the delamination threshold for biofilm was determined to be 22.86 MPa.

This knowledge of the minimum energy required to delaminate biofilm from a surface will be helpful in deciding the laser energy parameters in future experiments.

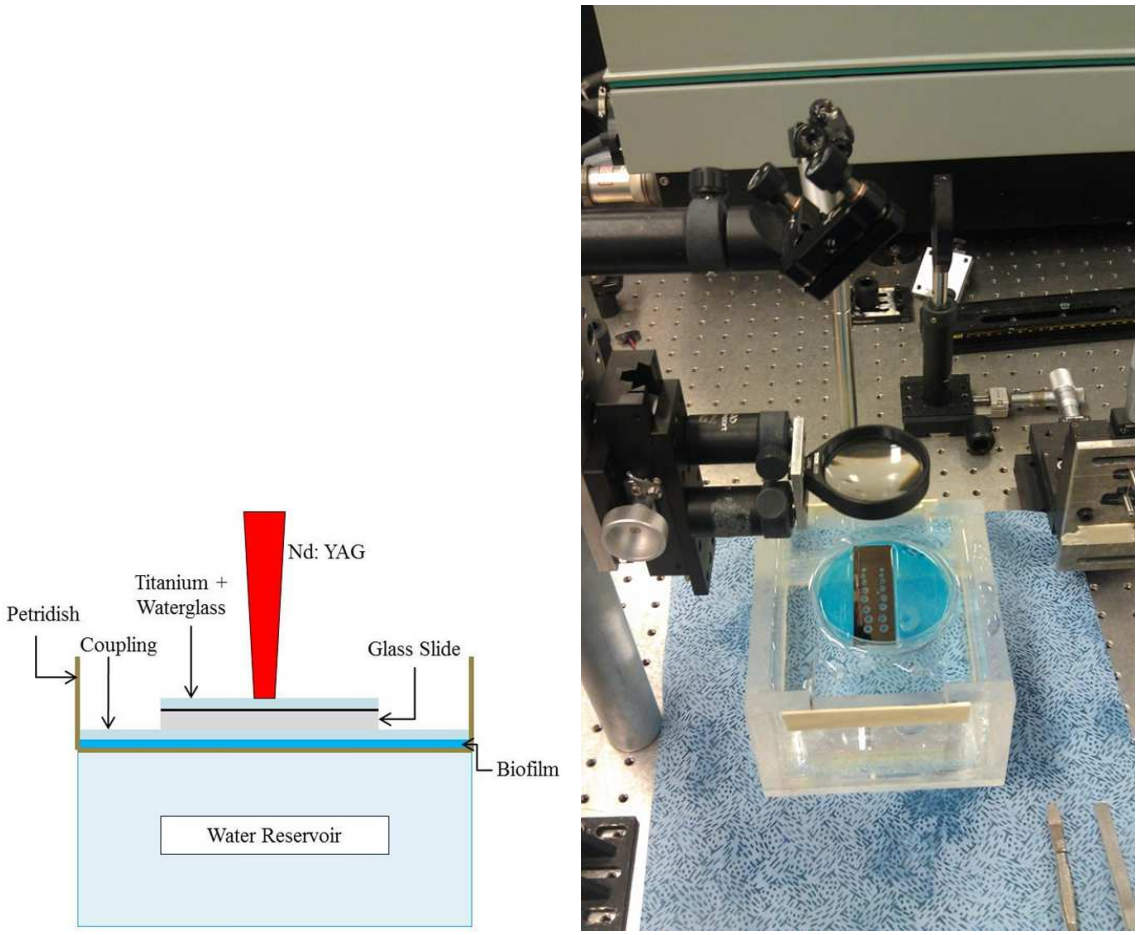


(a) Schematic Diagram of Experimental Set Up (b) Actual Set Up

Figure 2.1: Figure showing a) Schematic Diagram of the Experimental Set Up b) Actual Experimental Set Up, for the experiment to determine the delamination threshold of Biofilm

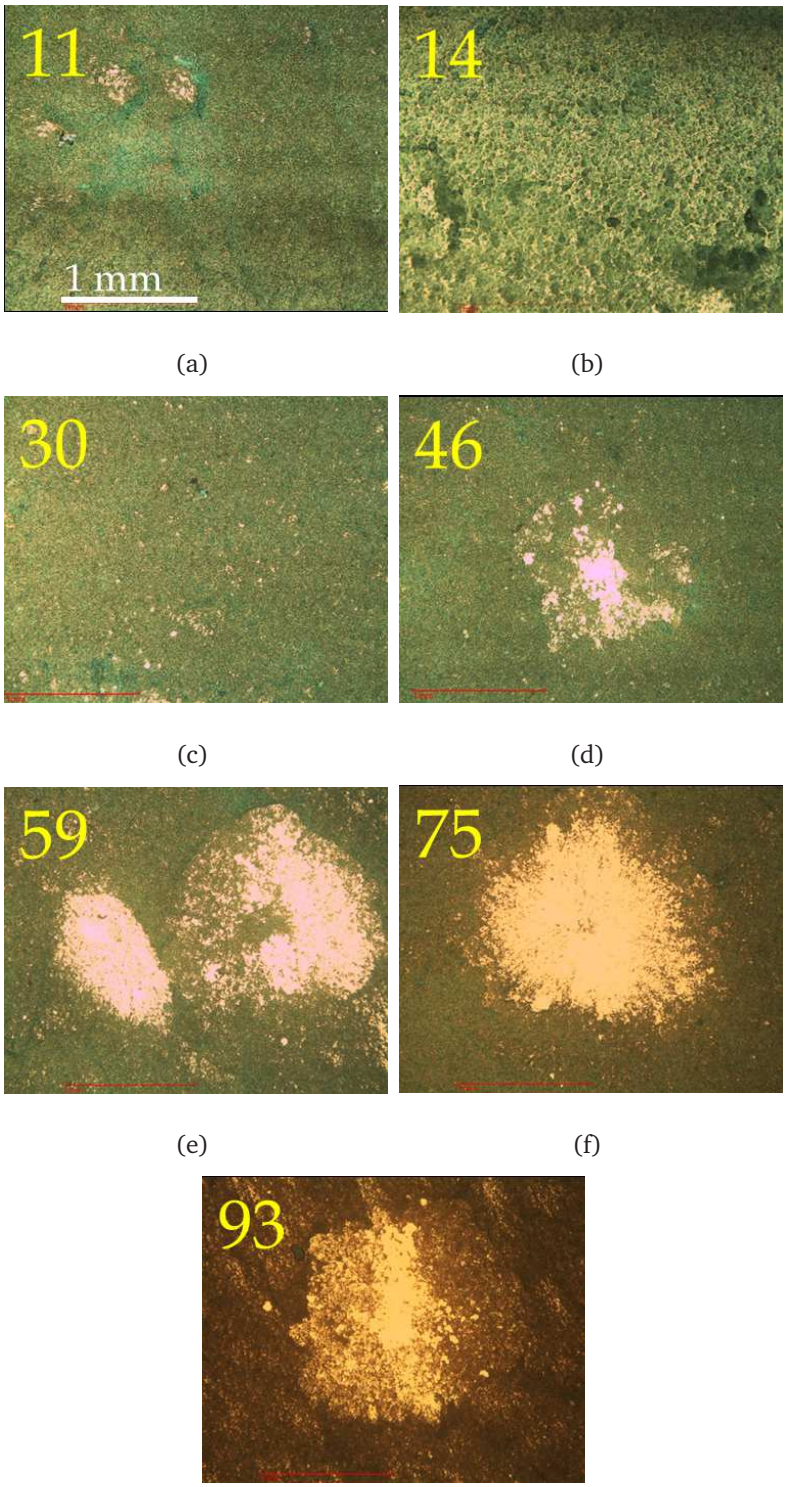


(a) (b) (c) (d) (e) (f) (g)

Figure 2.2: Light Microscope Images showing regions of biofilm delamination due to LGS. The biofilm samples were cultured for 24hours. The images are taken under 4x magnification. The biofilm samples were treated with a) 11 mJ/$mm^2$ b) 14 mJ/$mm^2$ c) 30 mJ/$mm^2$ d) 46 mJ/$mm^2$ e) 59 mJ/$mm^2$ f) 75 mJ/$mm^2$ g) 93 mJ/$mm^2$ respectively. Scale = 1 mm

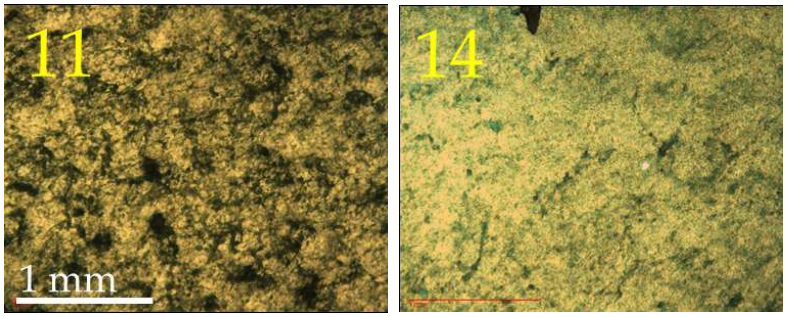


(a)




(b)

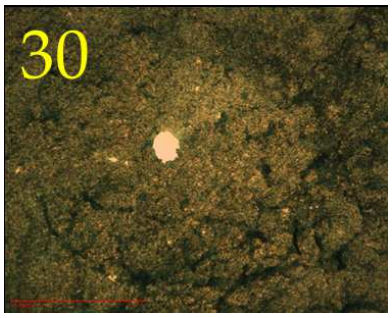


(c)

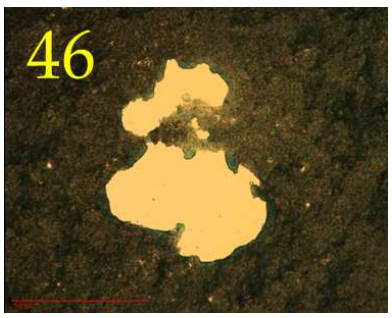


(d)

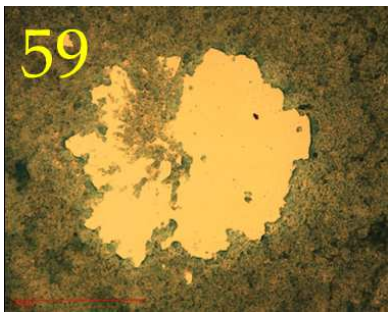


(e)

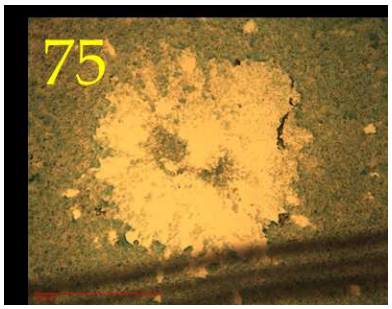


(f)


(g)

Figure 2.3: Light Microscope Images showing regions of biofilm delamination due to LGS. The biofilm samples were cultured for 48hours. The images are taken under 4x magnification. The biofilm samples were treated with a) 11 mJ/$mm^2$ b) 14 mJ/$mm^2$ c) 30mJ/$mm^2$ d) 46 mJ/$mm^2$ e) 59 mJ/$mm^2$ f) 75 mJ/$mm^2$ g) 93 mJ/$mm^2$ respectively. Scale = 1 mm

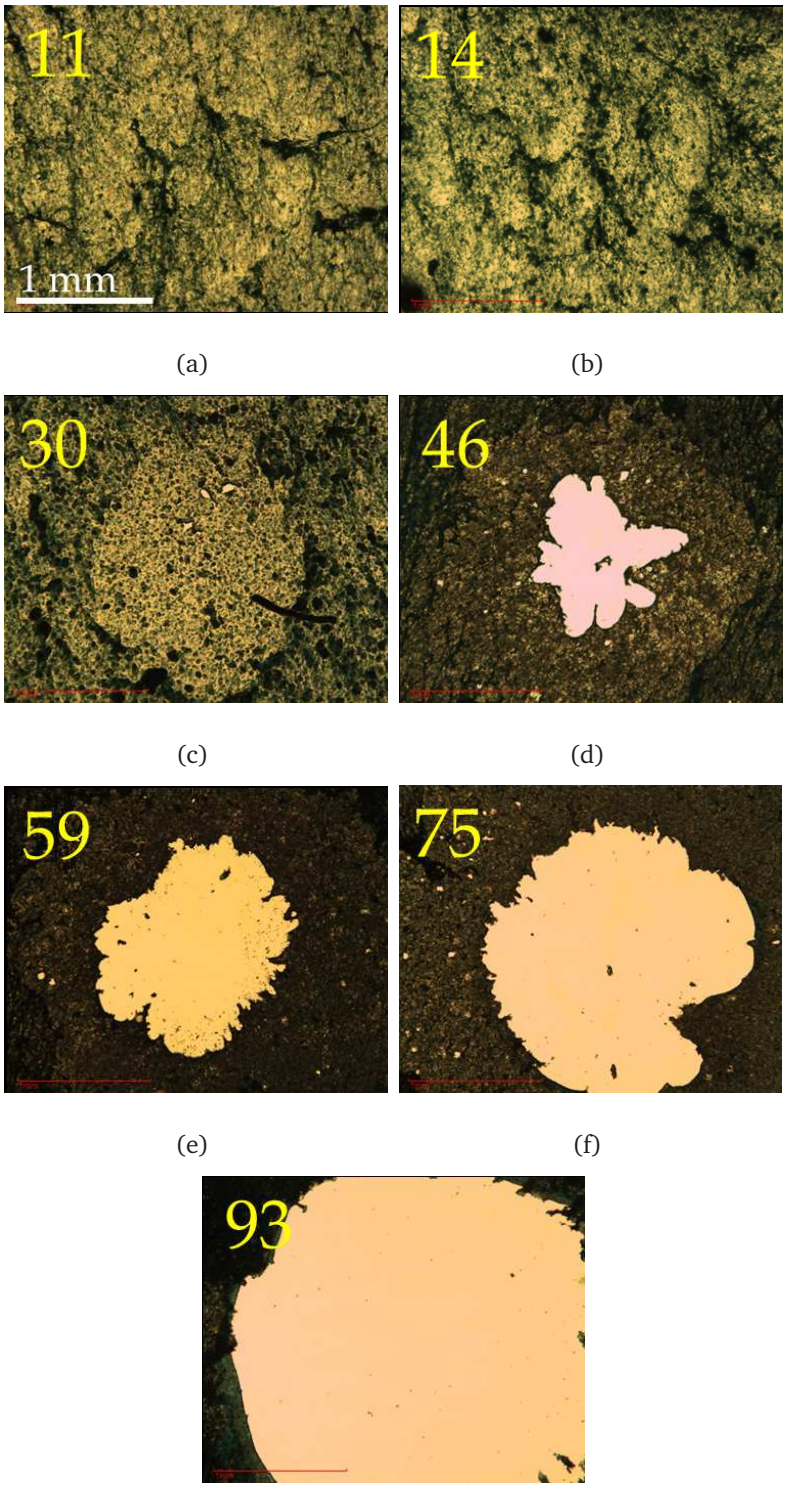


(a) (b) (c) (d) (e) (f) (g)

Figure 2.4: Light Microscope Images showing regions of biofilm delamination due to LGS. The biofilm samples were cultured for 72hours. The images are taken under 4x magnification. The biofilm samples were treated with a) 11 mJ/$mm^2$ b) 14 mJ/$mm^2$ c) 30 mJ/$mm^2$ d) 46 mJ/$mm^2$ e) 59 mJ/$mm^2$ f) 75 mJ/$mm^2$ g) 93 mJ/ $mm^2$ respectively. Scale = 1 mm

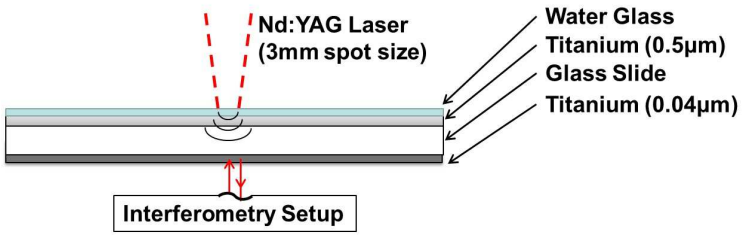


Figure 2.5: Set up used to generate a mechanical shockwave by making laser energy incident on it.

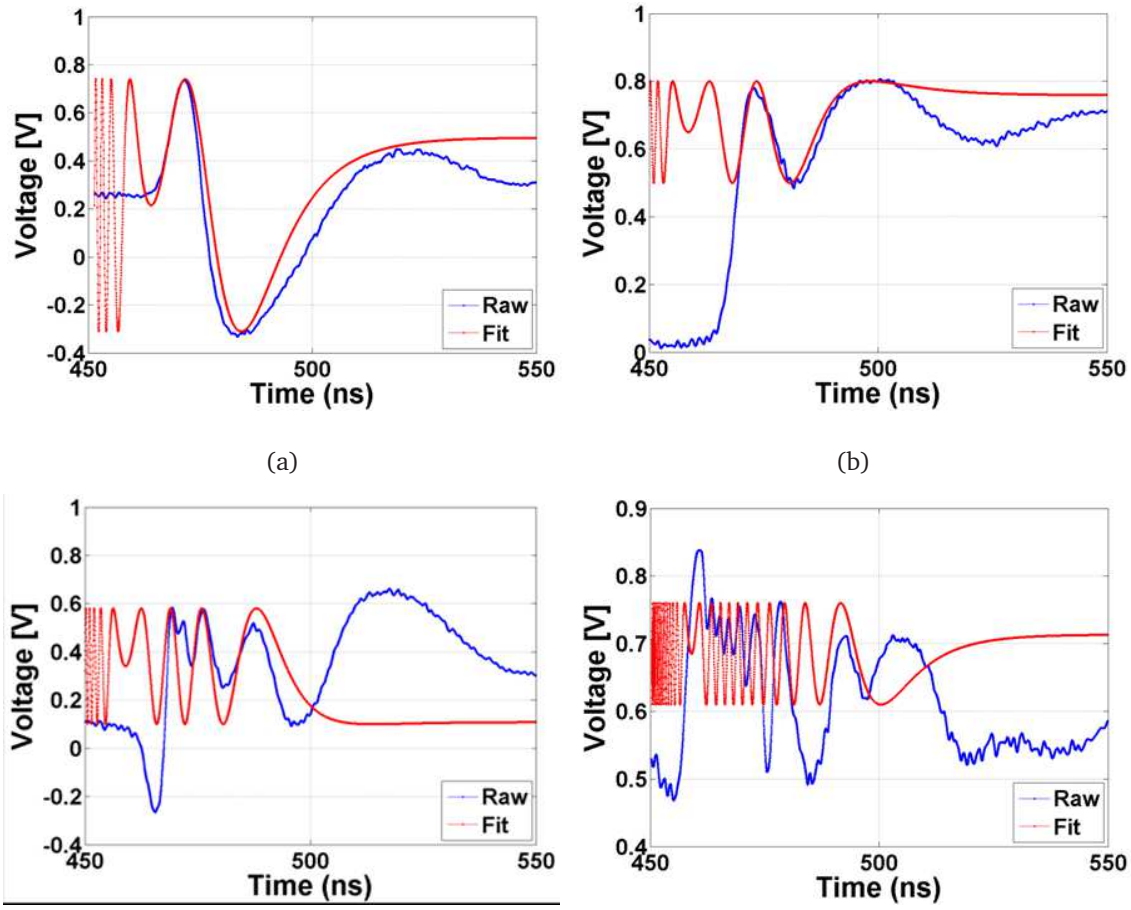


Figure 2.6: Raw as well as fitted interferograms for glass. The glass was treated with a) 11 mJ/$mm^2$ b) 14 mJ/$mm^2$ c) 30 mJ/$mm^2$ d) 75 mJ/$mm^2$ of energy

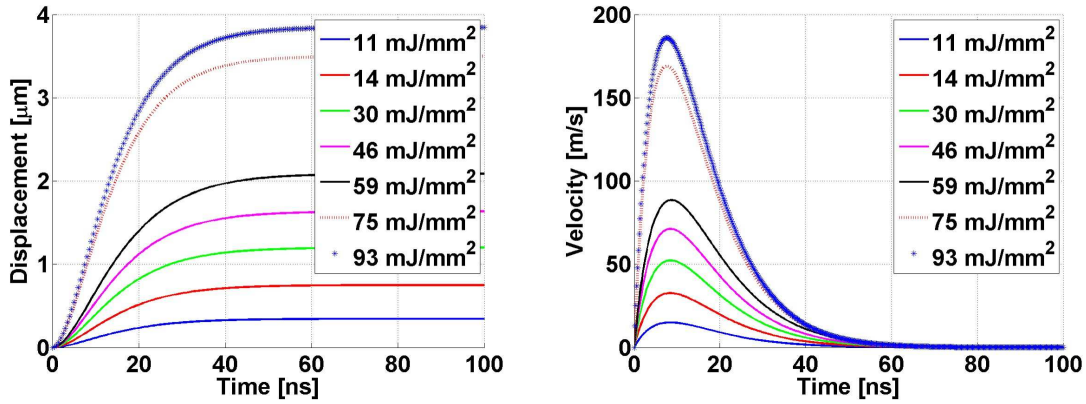


(a) (b)

Figure 2.7: Displacement and Velocity profiles for glass at 7 energy levels. These graphs were extracted from the interferometry data. The figures show the following a) Total Displacement profiles b) Surface Velocity Profiles

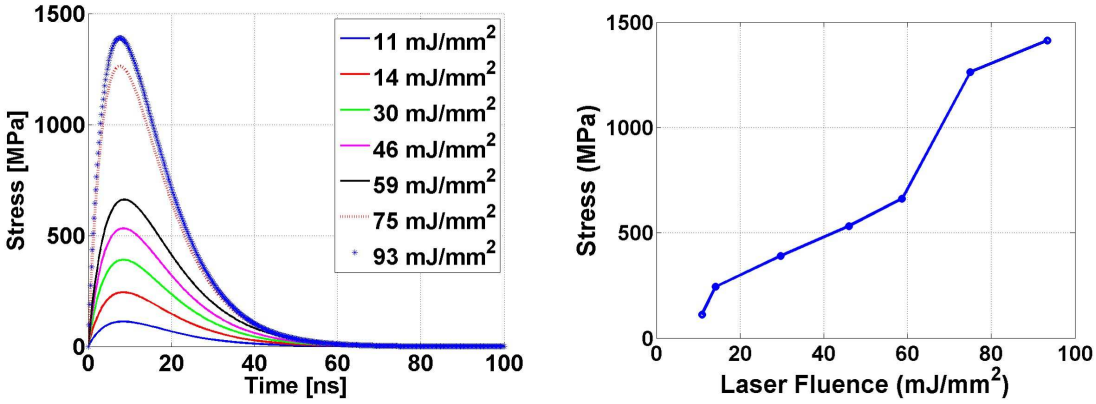


(a) (b)

Figure 2.8: The input stress profile for glass. a) Input stress profiles for 7 different energy levels b) Graph showing Peak Stresses vs laser fluence

# CHAPTER 3

# High Speed Imaging

A novel, low-cost high speed imaging system was developed to study the propagation of LGS (Laser-Generated Shockwaves). This chapter discusses the process of developing as well as using the imaging system to capture the propagation of the LGS. The system was able to successfully capture the phenomenon of cavitation that occurs as the LGS propagates from the surface of the glass into the coupling medium. At this interfaces there is a transition from positive to negative pressures and hence this phenomenon occurs here.

In the biofilm delamination experiments small regions of delaminations around the main region of delamination was observed. The study using the high speed imaging system was able to explain the cause of those small regions of delaminations in the periphery. These delaminations were caused by small cavitation bubbles.

## 3.1 Introduction

A high speed imaging system was designed and developed to study the propagation of the LGS. Of particular interest for imaging is the coupling medium since this is the region where the LGS moves from an extremely dense medium to one that is much less dense and this transition causes the formation of cavitation bubbles. A high speed imaging system was required to observe this phenomenon since it occurs in a time frame of

nanoseconds - microseconds. The system discussed in this chapter could take images of the events that are otherwise too fast for cameras. Due to lower shutter speeds of ordinary cameras the images turn out to be blur.

High speed imaging systems generally fall into 2 major categories. The first kind creates a video sequence with the number of frames per second (fps) larger than 25 - 30 Hz. Examples of these tpes of cameras are camcorders or webcams. These cameras then produce a slow-motion event during playback at normal fps rate. The second kind of system record frozen images of fast moving objects making sure that the image isn't blur [142]. For the first system, images of fast events are taken continuously at a very high rate, which, when pieced together form a video of the event. However, the second type of systems take images only once per event. If the entire event is to be recorded, the event has to be repeated a number of times. Each time the event occurs, the camera can capture an image at a different time instance during the event. These various images can then be stitched together to recreate the entire event. In the current study, the high speed imaging system developed was of the second type.

Infrared radiations were used to capture images in this particular study. Near and mid infrared region (700 nm - 14$\mu$m) has been used to image numerous phenomenon in the past such as fluid flows, water droplets, thermal changes, and shock wave propagation [126] [143] [144]. Shadowgraphy techniques such as the one described in [126] has also been widely used to image wave propagation. While capturing images in this study, the camera was positioned perpendicular to the direction of propagation of the laser beam and the LGS as shown in Figure 3.1. Water was coupled to the shockwave generating set up. As the LGS was generated and propagated downwards through water, images of the surface of water was acquired.

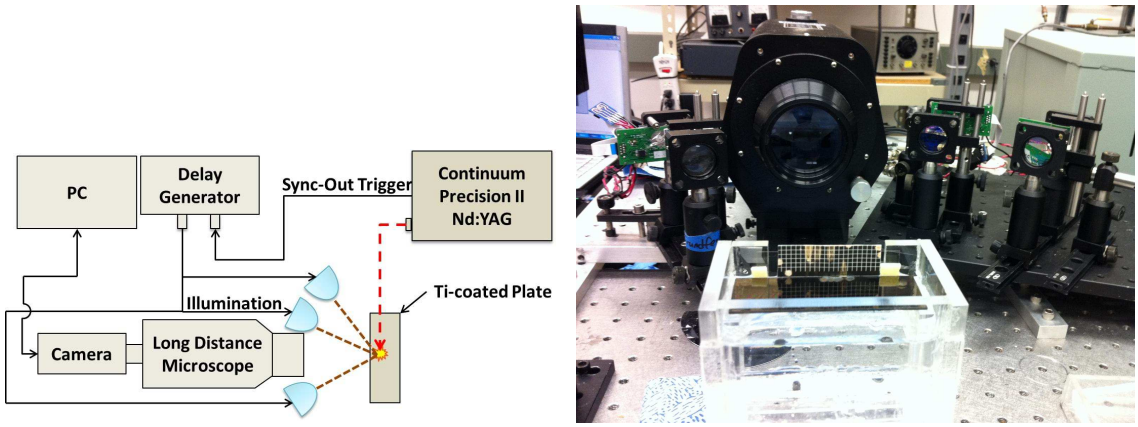


(a) (b)

Figure 3.1: a) Schematic Diagram b) Actual image of the high speed imaging system

One of the best sources of illumination for high speed imaging are short pulsed lasers [145] [146]. These laser systems are quite expensive and are usually bulky. For the high speed imaging system used in this study high power LEDs were used. They were much more economical and compact [143]. Many patents have been filed describing LED illumination packages [147] [148] for pulsed LED based high speed imaging. These are far more compact and cheaper compared to the pulsed lasers. In the current system, 3 LEDs were used to illuminate the target as shown in Figure 3.2. The infrared camera was coupled to a long working-distance microscope and appropriate filters were used to capture the reflected light from the imaging plane.

## 3.2 Parts of the Imaging System

### 3.2.1 Diodes

Three high power LEDs at 850 nm were used to illuminate the imaging plane as mentioned in the previous section. They were placed in a circular fashion around the imaging plane. The LEDs illuminate continuously for 9 ns when triggered using a single pulse. The integration time for each image is around 9 ns. Each LED was controlled by a diode

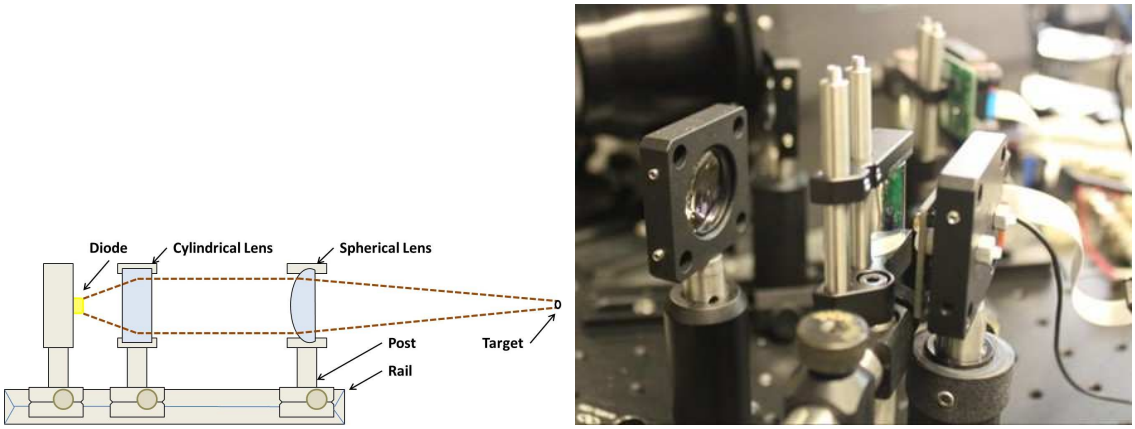


(a) (b)

Figure 3.2: a) Schematic Diagram b) Actual image of one of the LED system used for imaging

driver that requires 5 V for operation. Powerful illumination by the LED was was achieved using an external control voltage. An input of 0 to 3.8 V was scaled to an appropriate output from 0 to 200 V. The drivers controlling the LEDs were powered by a power supply and triggered using a single delay generator. Figure 3.2 shows a block diagram of the illumination and optics. In order to focus the light beam, a cylindrical (f = 20 mm) and a spherical plano-convex (f = 20 mm) lens were placed in line with the LED. The LED and lenses were mounted on a rail for easy alignment. The light from the three LEDs were focused on to the imaging plane.

### 3.2.2 Microscope and CCD Camera

A long working-distance microscope (Questar QM 100) which could be used to focus on objects 15 30 cm away was used. A CCD camera (Sony XCG 5005E) was placed behind the microscope such that the camera would capture images as seen through the microscope. This setup enabled the camera to take good images from a distance and also protected it from any debris flying from the shockwave generating apparatus. The microscope was placed 23 cm from the imaging plane. Two filters were placed between

the camera and the microscope: a 945 nm low-pass filter that blocked the 1064 nm laser light from entering the camera and a 850 nm band-pass filter that allowed only the light from the LEDs to enter into the camera. The camera in turn was connected to a PC. The camera was a high resolution black-and-white CCD camera with 2448 x 2048 pixel resolution and a fastest shutter speed of 10 ms. Using the software and manual control on for the camera shutter and LED an equivalent shutter speed of 9 ns was achieved.

### 3.2.3 Software

The laser was used to trigger the delay generator vis an external syncout port. The camera shutter took considerable time to open (several microseconds) compared to the time taken by the shockwave to arrive ( a few nanoseconds). As a result, the shutter was not connected to the delay generator but was controlled manually through the software provided for controlling the camera. Once the shutter was opened, the laser was fired. This would in turn trigger the LEDs to illuminate the imaging plane. The camera shutter would then close.

### 3.2.4 Image Processing

Image processing was carried out using MATLAB's histogram equalization and 2-D filtering functions. As a result of a high shutter speed and low illumination, the raw images was underexposed. Histogram equalization was performed to evenly distribute the pixel intensities. This helped increase the image contrast, but also resulted high frequency noise being highlighted.

To reduce the noise in the image, a finite impulse response filter was used. A 1D low-pass filter was convolved with itself to create a 2D low-pass filter. The filter had a blurring kernel that removed high frequency noise (Figure 3.3) creating a smoother image. The

entire process is demonstrated using an image taken by the imaging system (Figure 3.4).

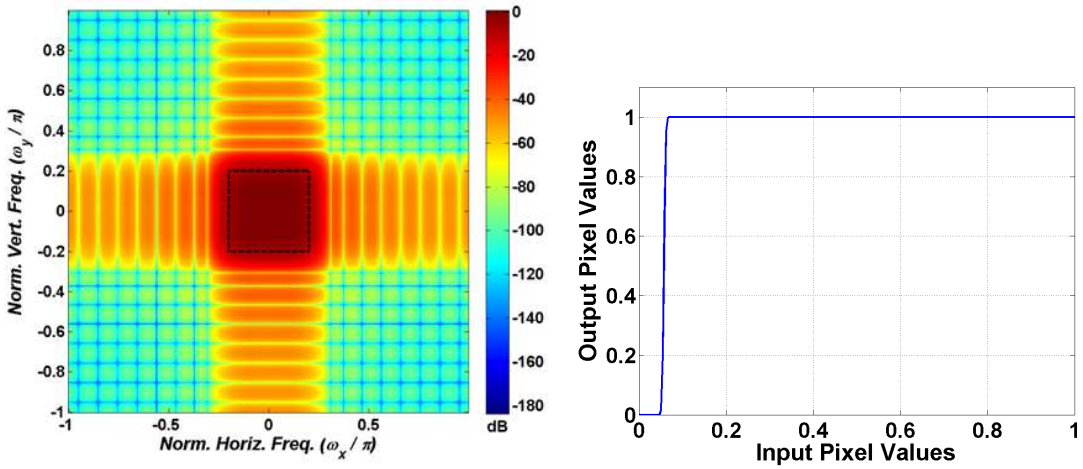


(a) (b)

Figure 3.3: Figure showing the image processing steps. (a) Histogram equalization mapping (b) 2-D lowpass filter frequency response obtained by convolving two 1-D FIR low–pass filters.

## 3.3 Experiment

Preliminary experiments were performed to ensure that shock wave propagation could be captured. Initisslly, the shockwave was generated, and no coupling medium was placed below the shockwave generating apparatus. The displacement of the glass slide caused by the shock wave was imaged. In the second set of experiments, the shockwave generating apparatus was coupled to water to image cavitation bubbles generated in water.

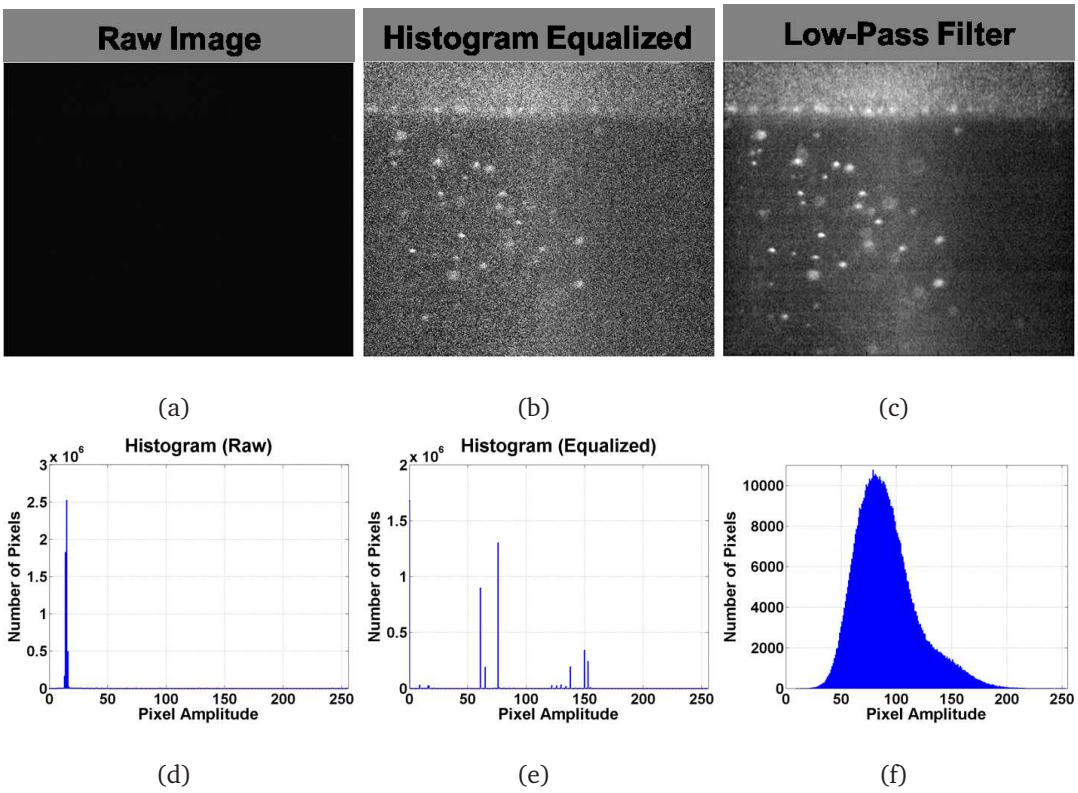


Figure 3.4: Implementation of the image processing process. (a) Raw image and (d) its corresponding histogram. (b) Histogram equalized image and (e) its corresponding histogram. (c) Low-pass filtered image and (f) its corresponding histogram

### 3.3.1 Imaging of Displacement caused by Shockwave

#### 3.3.1.1 Sample Preparation

The shockwave was generated using silica glass coated with a Ti film and waterglass as described in Chapter 2. Microscope slides (Corning Inc.) of the dimension 3 in x 1 and 1 mm thick were used.

#### 3.3.1.2 Imaging Platform

The glass slide was placed on a platform whose position could be adjusted in the x, y, and z-axes. The platform was positioned such that the bottom half of the glass slide was visible to the camera. A delay generator was triggered using the laser. As soon as the laser fires, it would send a signal to trigger the delay generator which in turn would trigger the LEDs for illumination of the event. The camera shutter was triggered manually and not connected to the delay generator. This is because it was not able to respond fast enough to the delay generator signal in order to capture the arrival of the shockwave on time. The time between triggering the laser pulse to the generation of the mechanical pulse at the titanium film was measured to be $\approx$ 370 ns. The time taken by the wave to travel through the glass slide was $\approx$ 100 ns. This time was calculated by simply using speed of sound in glass slide ($\approx$ 5910 m/s) and the thickness of the glass slide (1 mm). Thus the shockwave reached the bottom surface of the glass at $\approx$ 460 ns. Therefore, in order to image the shockwave as it exited the glass slide and entered the coupling medium , the delay generator was set to trigger the LEDs at $\approx$ 460 ns following the signal from the laser. The camera shutter was set to 15 frames per second which corresponds to a shutter speed of 66.57 ms. The Sony XCG software was used view the images captured by the camera. Using the multiple snapshots feature in the software a set of 10 frames could be captured. The shutter button and the laser were triggered manually almost simultaneously. The laser in turn triggered the delay generator which turned on the LEDs. The illumination by the LEDs lasted $\approx$ 9 ns in duration, and so only one of the ten captured was illuminated. The laser spot was targeted on the edge of the glass slide so that $\approx 3/4$ of the beam would hit the surface, and $\approx 1/4$ fell to the side. This was done so as to make sure enough stress was generated at the edge to be able to capture the events that are caused by the stress.

#### 3.3.1.3 Results and Discussions

Figure 3.5 shows images of the glass slide captured by the high speed imaging system. The top region of the images have bright regions which seems to be 850 nm emissions due to fast thermal expansion of the Ti film. The interferometry results suggest that the maximum displacement of the glass slide that can be brought about by a shockwave (93 $mJ/mm^2$ i.e. 660 mJ/pulse) is $\approx 4\mu$m. Since the resolution of the camera is $\approx 2.13\mu$m per pixel, this displacement of $4\mu$m would result in a maximum displacement of $\approx 1.9$ pixels in the image. This change is difficult to discern as shown in Figure 3.5. It can easily be confused as vibrational displacement. In Figure 3.5(a) however, localized displacement is observable when compared to Figure 3.5(b). This displacement is most probably brought about by tensile stress waves rather than compressive waves. In Figure 3.5(c), it can be seen that the glass slide has been fractured slightly which has caused cavities and dents at the bottom of the slide. This occurs because when the shockwave reaches the glass-air interface , it reflects back as a tensile wave due to the large impedance mismatch between glass and air. The magnitude of the tensile stress exceeds the failure level of the glass and causes it to fracture. Adding a coupling medium below the surface of the glass will allow the shockwave to propagate through the coupling medium without significant reflection.

### 3.3.2 Imaging of Cavitation Bubbles Caused by Shockwaves

#### 3.3.2.1 Sample Preparation

In order to image the cavitation bubbles, the bottom of the glass slide was painted black. This is to prevent the light in 850 nm range generated by Ti ablation from passing through the glass slide. As can be seen in the previous experiments, this light seeping through the glass slide was polluting the image (Figures 3.5(a) and 3.5(b)). Also a thin piece of paper was placed vertically on top of the edge of the glass slide to prevent any light generated

during shockwave generation from entering the camera 3.6. The laser energy used was 530 mJ/pulse. 0.5$\mu$m of titanium was sputtered onto the glass slide, and $15-20\mu$m of water glass was spin-coated onto the titanium.

#### 3.3.2.2 Imaging Platform

Figure 3.7 shows a glass slide holder that was designed for this experiment. It has a compartment for holding water and a window at the side from where the shockwave propagation could be captured. The viewing window was covered using a cover slip to prevent any debris generated during the shockwave generation from flying towards the long distance microscope. The glass slide was placed horizontally next to the microscope coverslip. The compartment below the glass slide was filled with water till there were no air bubbles visible. The field of view of the camera was set below the glass side (Figure 3.7(b)), with the edge of the glass slide protruding down $\approx 0.2$ mm from the top of the viewing frame. The vertical focusing plane was $\approx 1$ mm into the glass slide. That is the edge of the glass slide was slightly out of focus.

#### 3.3.2.3 Timing Mechanism

The experimental procedure to capture the image in this section is the same as that discussed in section 3.3.1.2. The various timings that are important for the purposes of this imaging system are shown in Figure 3.8. In this set of experiments when the camera was triggered it took 3 images. Each image frame lasted 329.42 ms. For each trial, the camera was triggered and the laser was fired manually within 1 second of each other. This ensured that the shockwave propagation event was captured within the three frames. Figure 3.9 shows a series of images taken before, during, and after the shock wave propagation at the glass-water interface. Figure 3.9(b) taken at 475 ns captures the shock wave event. The bottom of the glass slide can be seen as the bright horizontal region

at the top of the image. The glass slide is out of focus since our focusing plane is 1 mm into the glass slide. As can be seen, there are no cavitation bubbles in the images before the shock wave arrives at the glass-water interface. Also there are only two bubbles left after the shockwave has propagated through the glass-water interface. This proves that the LGS is indeed the reason for the generation of the cavitation bubbles. Images shown are generated by processing the images captured by the infrared camera.

Cavitation bubbles in tissues induced by shock waves are known to cause tissue damage [149]. But in the case of our experiment, the propagating bubbles created by cavitation meet the biofilm layer before reaching the underlying tissue. As seen in Chapter 2, these bubbles cause delamination of the biofilm and do not get the chance to reach underlying tissue to cause them any harm. From the images, it can be seen that the shock wave produces a collection of microbubbles traveling downwards to a distance of at least 1 mm. The total distance traveled by the microbubbles might be more than 1 mm but it cannot be viewed in the images taken by the current system. Nevertheless, these images prove that cavitation bubbles are produced at the glass-water interface due to the propagation of LGS from glass to water.

Figure 3.10 depicts the generation and propagation of cavitation bubbles. The shock wave reaches the glass-water interface at $\approx$ 460 ns. At 465 ns, clusters of bubble formation can be seen (Figure 3.10(a)). The size and shapes of the bubbles moving downwards remain almost constant from 495 - 535 ns. At a later instant in time 1000—2000 ns, significantly less cavitation bubbles can be seen. The cavitation bubbles move in 3-dimensional space, hence many bubbles in the image are out of focus. According to the literature it takes several microseconds for the bubbles to form and collapse [150]. From the current set of images it takes $\approx 2\mu s$ for the bubbles to form and collapse. After $2\mu s$ fewer bubbles are visible, this may be because the bubbles might have collapsed or migrated to other

regions out of view.

The sizes and number of bubbles in the images were found out using the ImageJ software. Four of the outlined images are shown in Figure 3.11. Figure 3.12 shows the number of bubbles counted for each image. Figure 3.13 shows the average diameters of the bubbles found in each image. The number of bubbles are inconsistent according to the Figure 3.12. That is because the bubbles migrate in and out of the field of view. During the first 60 ns the average dismeter of the bubbles is 39$\mu$m. From 600 ns to 2000 ns it increases to 71$\mu$m.
In the biofilm delamination experiment described in chapter 2, the coupling medium was 1 mm thick. Thus there would be an interaction between the cavitation bubbles and the biofilm. The small regions of delamination around the central delaminated region, as shown in Figure 3.14 are caused mainly by cavitation bubbles.

## 3.4 Conclusions

This chapter discusses the building of a low cost, high speed imaging system and how it was used to image the propagation of laser generated shockwaves. The imaging system made use of low cost LED's for illumination, a black and white CCD camera and a long distance microscope. Firing of the laser and triggering the camera was done manually. The LED illumination was controlled by the laser. Images of the LGS propagation was successfully captured using this system.

The images showed that LGS propagation from glass to the coupling medium lead to the formation of cavitation bubbles which moved in the same direction as the LGS. These bubbles are now known to be the cause of the small regions of biofilm delaminations around the central delaminated region. These bubbles are formed as a secondary effect

and are very small in size. As a result they have very low penetration power and do not lead to high tensile pressure when the burst. Hence they do not seem to cause any damage to the regions lying below the biofilm and simply cause minor delaminations of the biofilm.

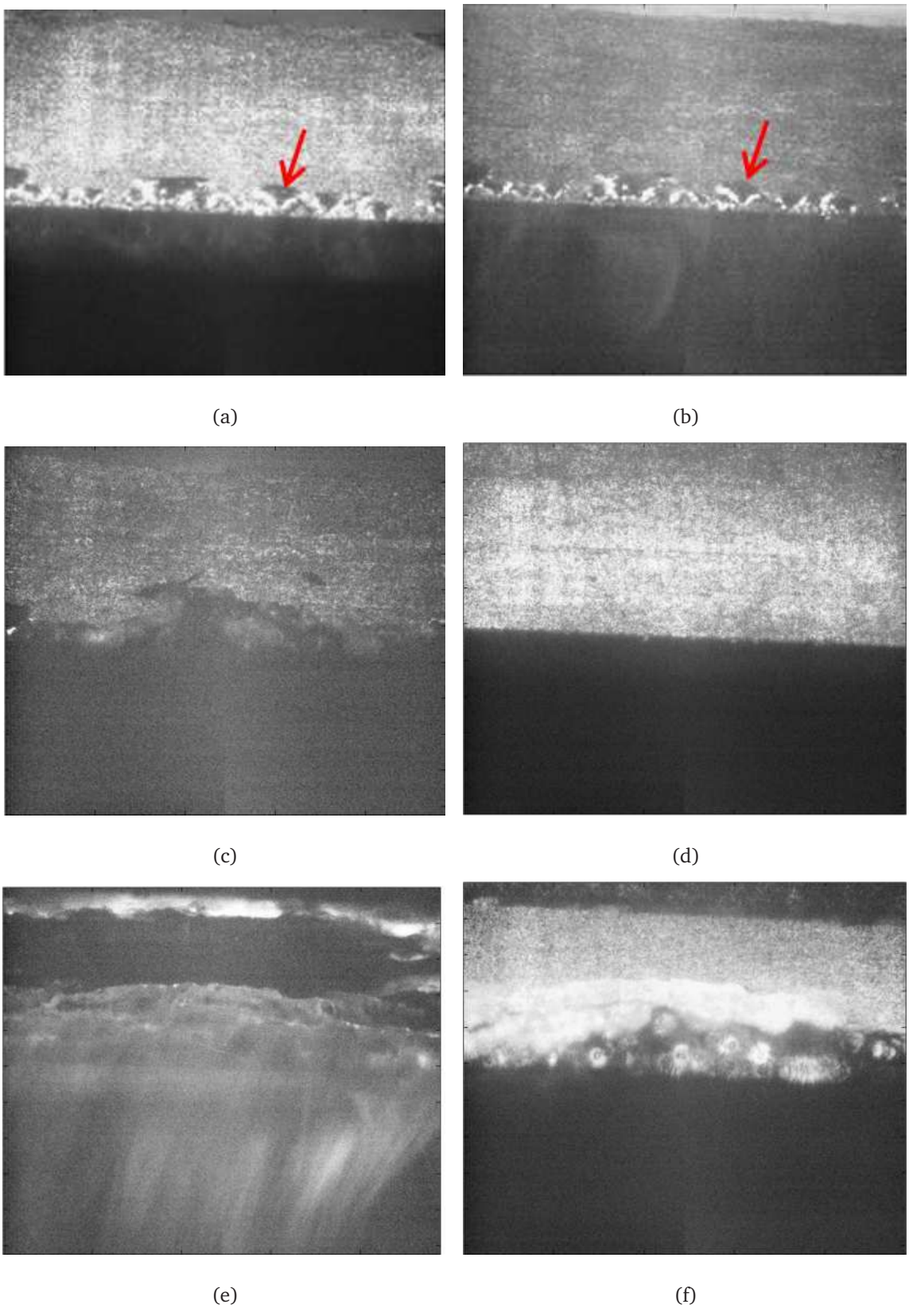

Figure 3.5: The glass slide before,during and after LGS application at two different points in the the glass slide. For point 1 a) before b) at 460 ns during LGS propagation c) after LGS application; For point 2 a) before b) at 530 ns during LGS propagation c) after

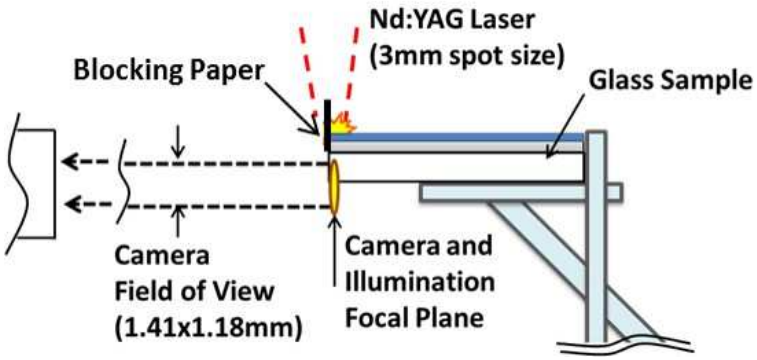


Figure 3.6: The Imaging Platform with a blocking paper in order to block the light produced during shockwave generation from entering the image

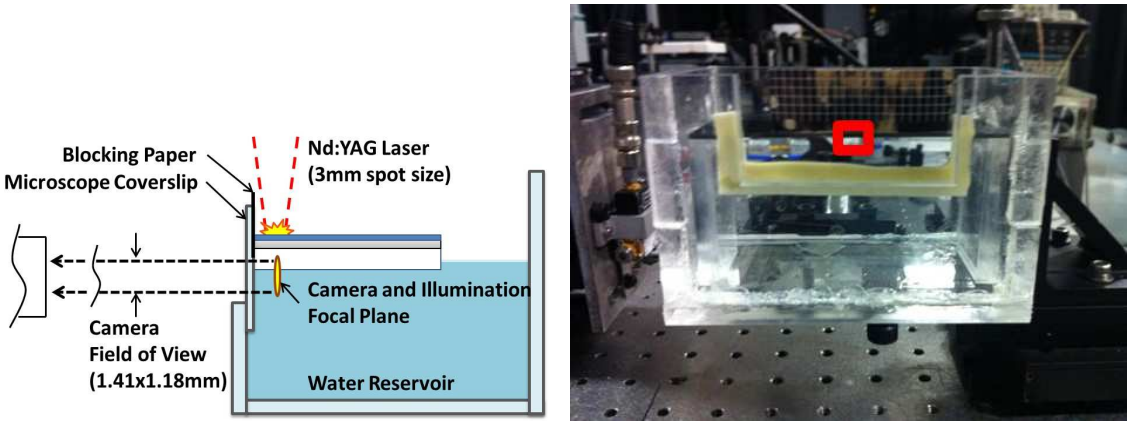


(a) (b)

Figure 3.7: a) Schematic Diagram b) Actual image of the high speed imaging system used to image the cavitation bubbles. The red box shows the approximate field of view.

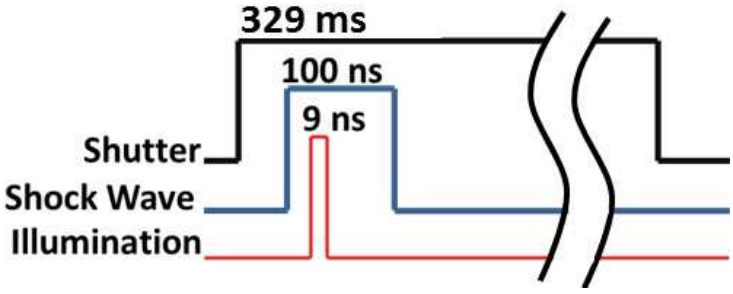


Figure 3.8: Relative timings for illumination and capturing of image

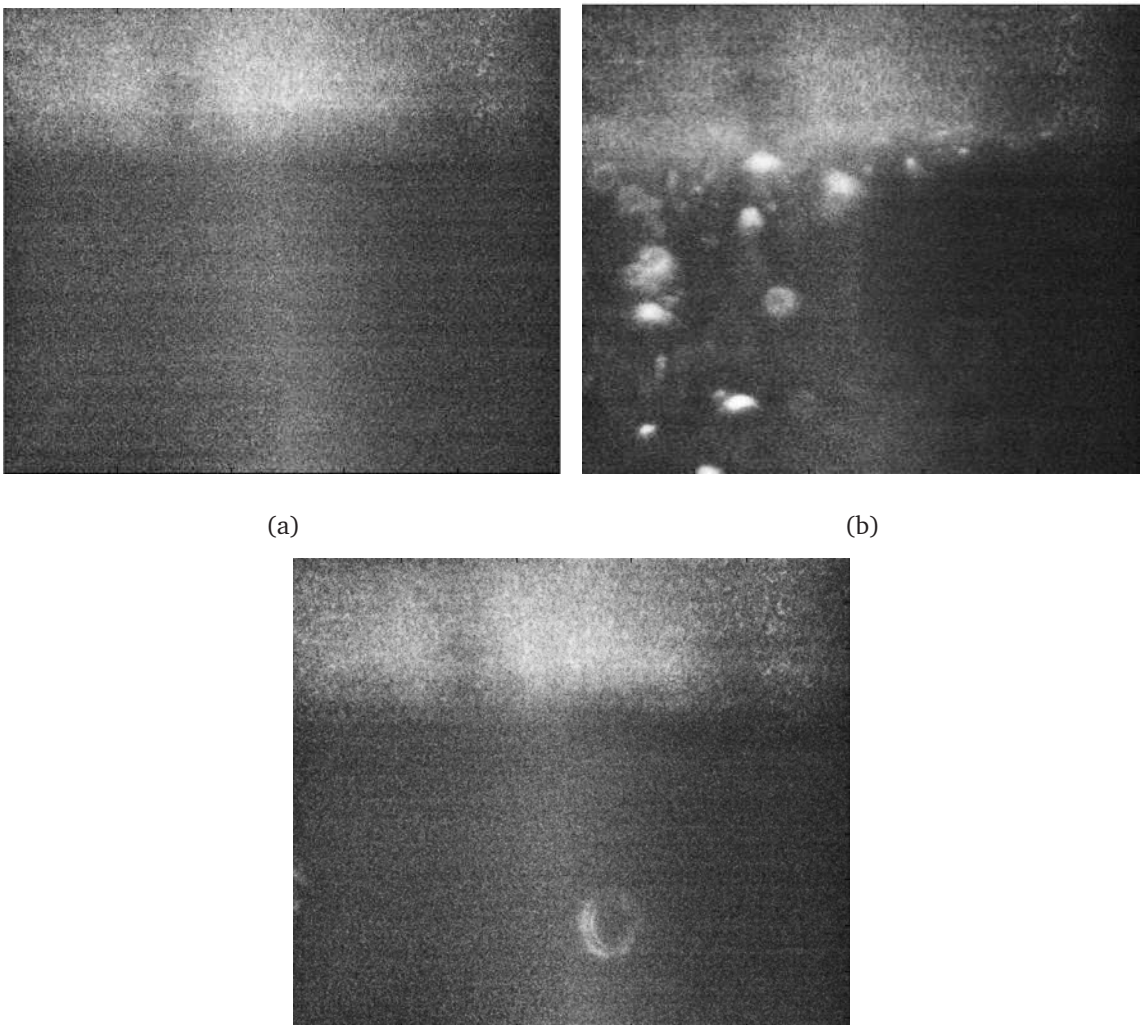

(a) (b)

(c)

Figure 3.9: The same region in the coupling medium before,during and after the shockwave propagation event, a) Before the laser was fired b) During the shockwave propagation, 475 ns after the laser was fired c) After shockwave propagation.

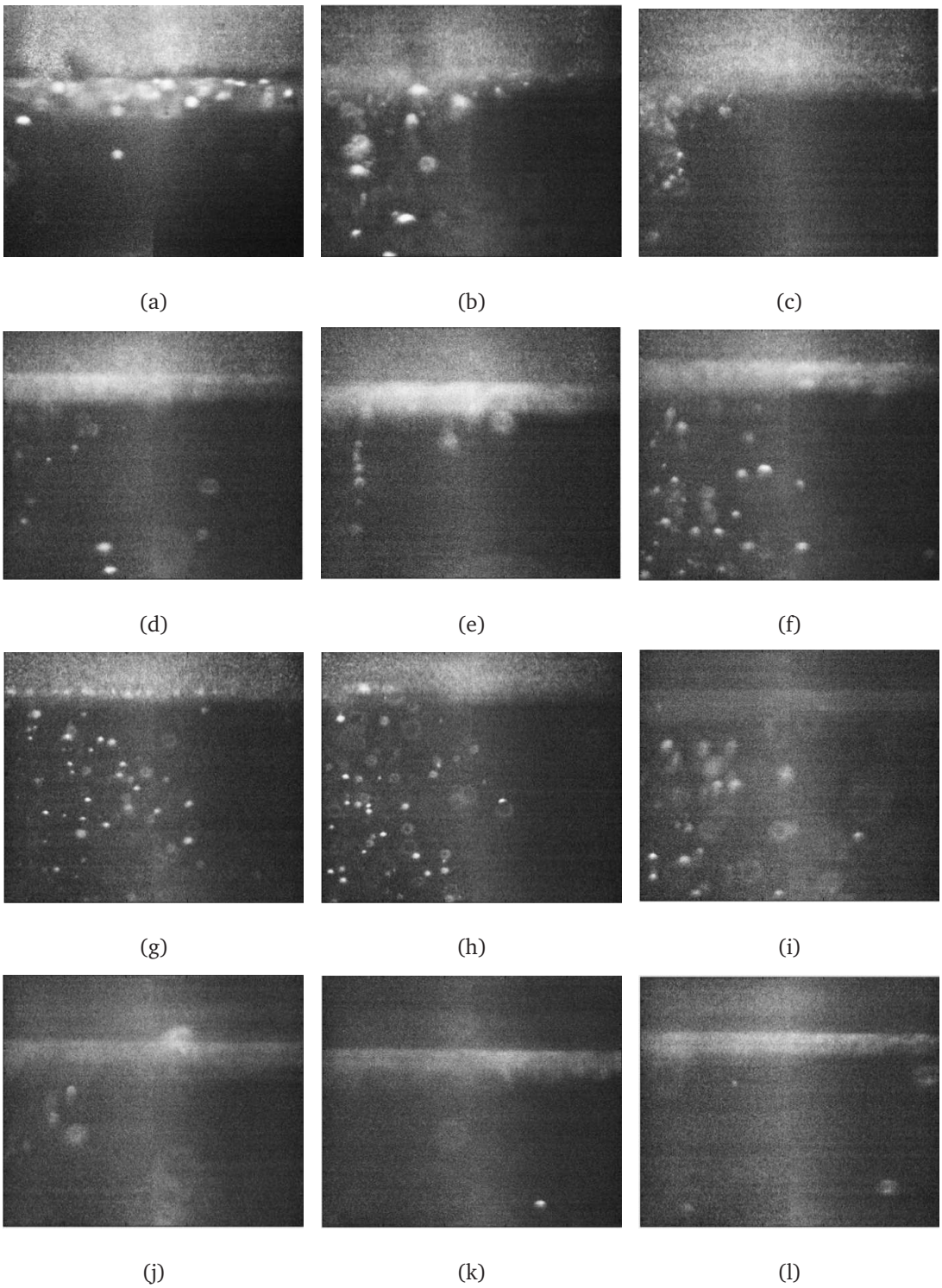


Figure 3.10: The generation and propagation of cavitation bubbles from 465 ns to 2000 ns. a) 465 ns b) 475 ns c) 485 ns d) 495 ns e) 505 ns f) 515 ns g) 525 ns h) 535 ns i) 600 ns j) 1000 ns k) 1500 ns l) 2000 ns

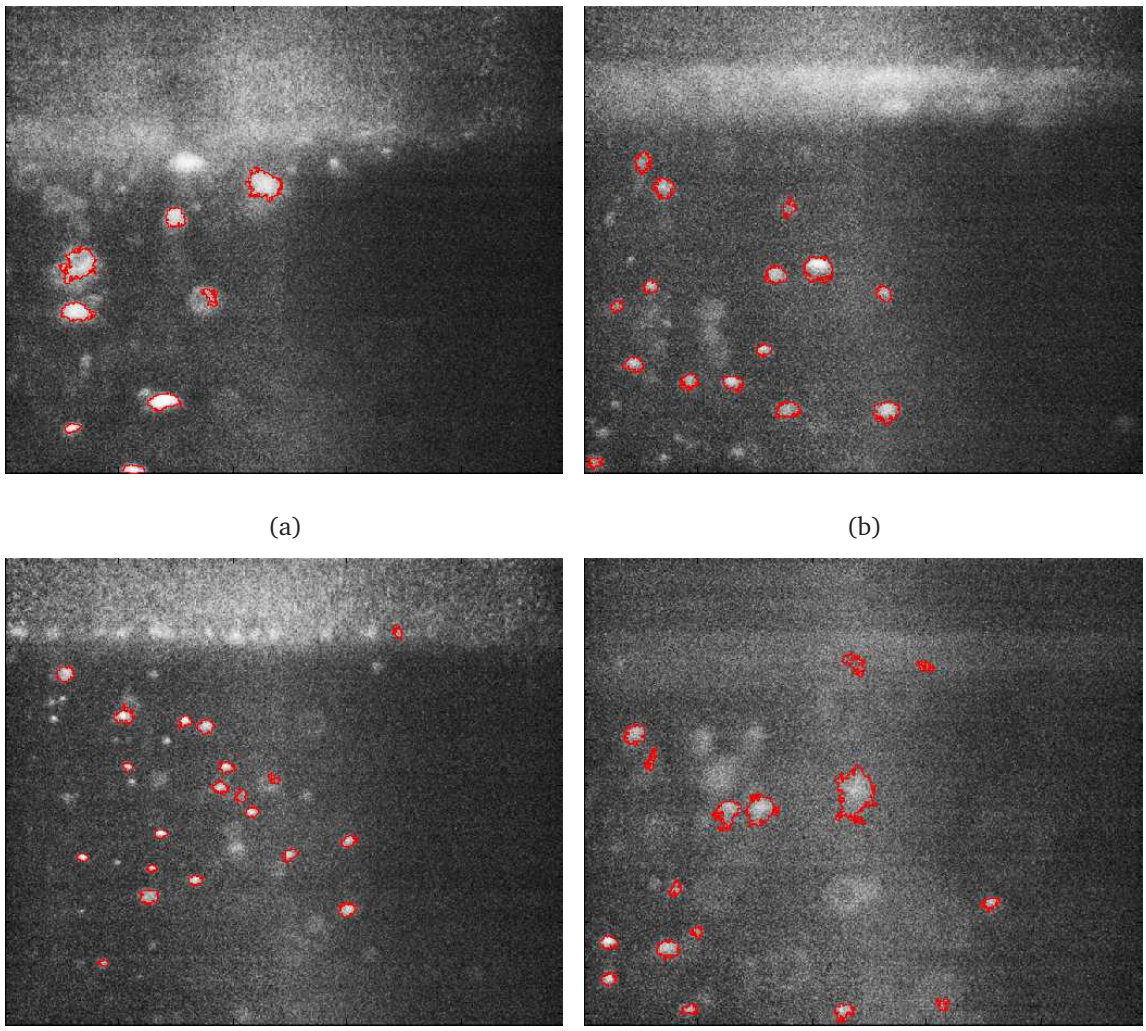

(a) (b)

(c) (d)

Figure 3.11: The outline of cavitation bubbles done using ImageJ software at a) 475 ns b) 515 ns c) 525 ns d) 800 ns. The outlined bubbles are the clearest bubbles used in bubble dismeter calculation.

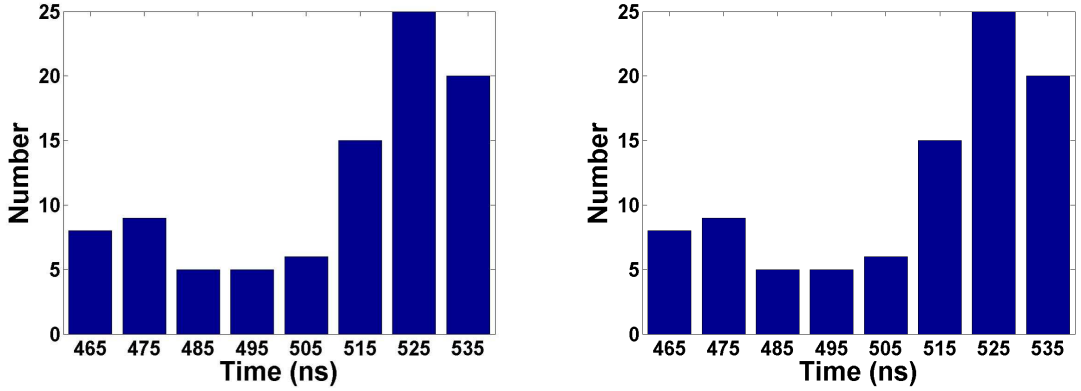


(a) (b)

Figure 3.12: The number of bubbles counted for each time point a) 465 ns to 535 ns b) 600 to 2000 ns

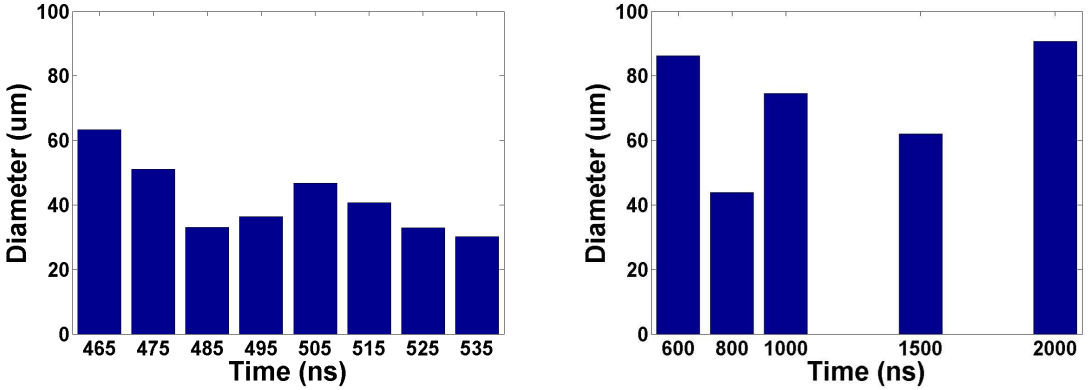


(a) (b)

Figure 3.13: The average diameter of the bubbles at each time point a) 465 ns to 535 ns b) 600 ns 2000 ns

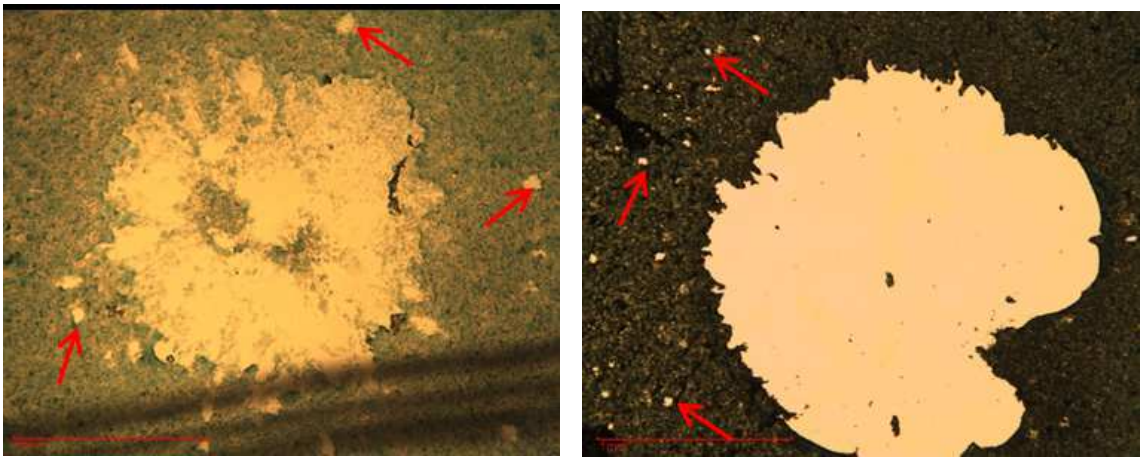

(a) (b)

Figure 3.14: Biofilm delamination at 75 mJ/$mm^2$ for a) Two day growth b) Three day growth. Red arrows indicate delamination due to cavitation bubbles.

# CHAPTER 4

# Effect of Laser Generated Shockwaves on *Ex vivo* Porcine Skin

## 4.1 Introduction

The use of LGS (Laser-Generated Shockwaves) as a technique to rid biofilms off of biotic and abiotic surfaces is of critical importance. The goal of this study is to understand the effects of LGS on freshly harvested porcine skin tissue. Porcine skin was chosen as it is very similar, both physiologically and anatomically, when compared to human skin [151] [152]. As discussed in Chapter , LGS have been shown to permeabilize cells [118] [119] [120] [121] and deliver macromolecules, permeabilize skin and even permeabilize biofilms [122] [123] [127]. When antibiotics are coupled with shockwaves, a killing effect of bacteria within the biofilm structure is achieved [128]. The underlying structures that biofilms reside on have been shown to not be damaged under the stress waves.

The mechanical effects of laser and LGS on various biological tissues have been studied and put to use extensively in the past few decades [153] [154] [155] [156]. In as early as 1984,excimer lasers were demonstrated to ablate tissue with minimal thermal injury [157]. Subsequently, Puliafito showed that 193nm radiation produced smaller damage zones than 248nm radiation when ablating the crystalline lens [153]. On the whole, excimer lasers were found to be effective in producing controlled ablation of the crystalline lens *in vitro* with effects similar to those seen in the cornea. Vogel et al. [154] compared the effects of picosecond (ps) and nanosecond (ns) pulses while performing

Nd:YAG laser surgery on intraocular tissue. Laser- induced cavitation effects were seen to be the major drawback of intrastromal corneal surgery. Cavitation causes tissue displacement and produces unpredictable refractive changes in the lens. The investigators concluded that ps pulses increased precision and diminished unwanted disruptive side-effects when compared to ns pulses, whereby the damage range decreased by a factor of three.Thus, ps pulsed lasers could be used for applications requiring great precision, although ablation rates are slow. In urology, the use of laser induced shockwaves for lithotripsy began to be explored both in combination with ultrasound [155] as well as exclusively with LGS [157]. By 1990, a variety of laser lithotripsy systems were in clinical use for urinary stone fragmentation [158]. The combination of small fiber diameters, mechanical stiffness of the endoscopes, and difficulty aiming the laser fibers led to perforation rates of approximately 10% of transurethral lithotripsy procedures [158]. Subsequently Holmium:YAG laser based systems were developed and supplanted the original 504 nm dye laser based systems.

In fact, Doukas [125] and Kollias showed effective drug delivery through the stratum corneum and the propagating wave did not create any pain or visible damage to the skin due to the spatial time scales of the stress disturbance. This chapter will present the purely compressive mechanical effect of using laser generated shockwaves generated using mylar on porcine tissue, including the same energy levels used to delaminate biofilms off polystyrene.

## 4.2 Materials and Methods

### 4.2.1 Specimen Preparation

The porcine model was chosen as it has been used as a model for human skin in the past due to its similarities to human skin both physiologically and anatomically [151] [152].

Porcine skin specimens were harvested from the abdominal region of a pig immediately postmortem. The specimen was cut into square shaped pieces of 5 mm length using a scalpel and blade. Each resulting specimen was maintained at room temperature (25°C) throughout the experiment, and not frozen, so as not to alter the structure or mechanical properties of the collagen fibers. LGS treatment was carried out no more than 30 minutes after specimens were harvested.

### 4.2.2 Substrate Preparation

Mylar sheets with dimensions of 80 x 30 cm x 0.1 mm were RF sputtered (Denton Discovery II 550, Denton Vacuum, NJ USA) with 0.5 $\mu$m thick layer of Ti. A layer of waterglass was then spin-coated on top of the Ti to achieve a uniform layer of $50-100$ $\mu$m. The waterglass layer acts as the constraining layer and is transparent to the Nd:YAG laser wavelength of 1.064 $\mu$m.

### 4.2.3 Shockwave Generating System and Laser Parameters

A Q-switched, Nd:YAG laser was used to generate LGS. A 3 - 6 ns long Nd:YAG laser pulse is impinged over a 3 mm dismeter area on the 0.5 $\mu$m Ti sandwiched between the back surface of the Mylar sheet and the layer of waterglass. Laser-generated pulses impinging upon the thin metallic surface generate stress waves within the material. The laser energy then ablates the thin metallic film, thereby causing a rapid thermal expansion of the film resulting in a compressive wave propagating through the substrate. The laser fluence, pulse width and the substrate material properties contribute to the temporal characteristics of the stress wave. The peak stress, rise time of the wave, and the stress profile generated are dependent on the above-mentioned parameters.

## 4.3 Experimental Procedure

The porcine skin sample was immersed in a petridish containing deionized water, such that there was a 1 mm thick layer of deionized water over the sample. The deionized water was used as a coupling agent between the sample and the Mylar sheet. The pigskin was held in place by placing it in between two acrylic blocks glued to the base of the petridish. The shockwaves were made to be perpendicularly incident on the porcine sample as shown in Figure 4.1 .

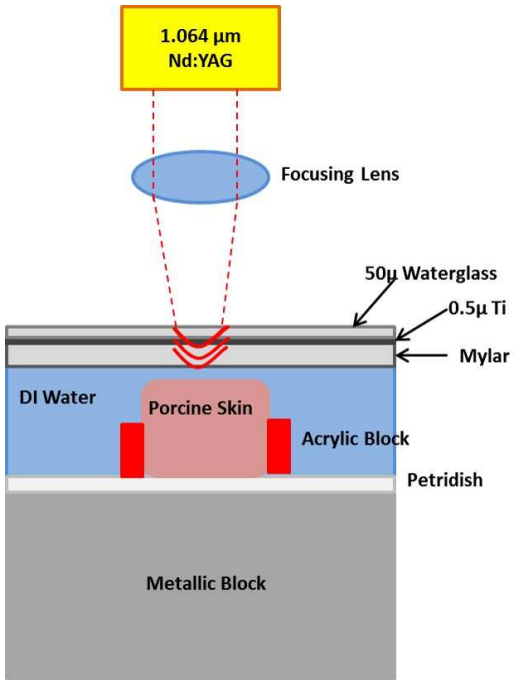


(a)

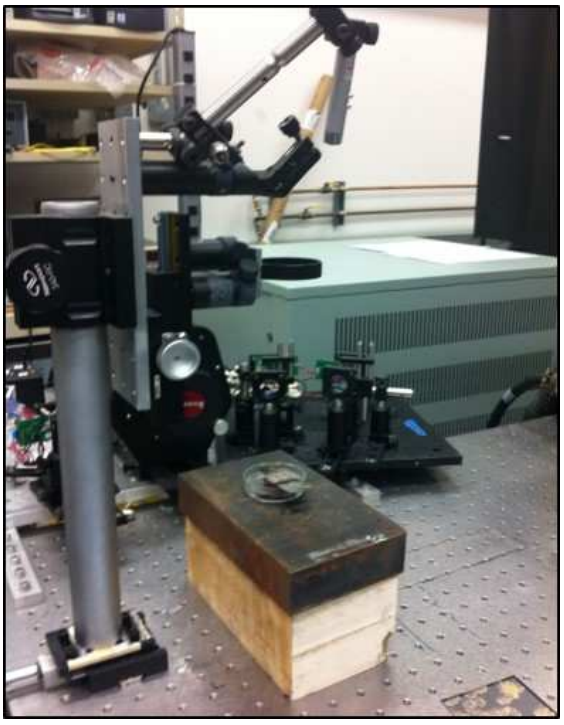

(b)

Figure 4.1: a) Schematic diagram b) Actual image of experimental set up to determine effect of LGS on *ex vivo* porcine skin

Each sample was subjected to LGS of a particular laser fluence ranging from 100-500 mJ. The precise laser fluences and corresponding energy density generated by the laser are shown in Table 4.1. For this pilot investigation, there were two samples per energy

level and one control sample.

Table 4.1: The energy density corresponding to each energy fluence used in the experiment.

| Laser Fluence (mJ) | Energy Density (mJ/mm2) |
|---|---|
| 118 | 16.68 |
| 149 | 21.07 |
| 228 | 32.24 |
| 264 | 37.33 |
| 350 | 49.49 |
| 400 | 56.56 |
| 498 | 70.42 |

### 4.3.1 Sample Preparation for Analysis

Immediately after shocking, the samples were fixed in formaldehyde and prepared for paraffin histology. Specimens were sectioned sagitally at 5$\mu$m along the midline, coinciding with the center of 3 mm shocked region. This region should correspond to the maximum mechanical impact generated by the laser shockwaves. The sections were then stained using H&E and Masson's Trichrome stain.

The tissue sections were scored on the basis of their overall appearance (O) and linear/slit- like spaces roughly parallel to the surface of the skin (S) when compared with other samples, on a scale from 0 to 3. An O score of 0 indicates that the sample is very different from the rest of the samples whereas an O score of 3 indicates that the sample is very similar to the rest of the samples on the basis of overall appearance. A S score of 0 indicates very small number of linear/slit-like spaces in the sample while a S score of 0 indicates very large number of linear/slit-like spaces. While assessing the over-

all appearance, the tissue sections were examined to see whether the stratum-corneum, epidermis, dermis and the epidermal-dermal junctions were intact. Indications for ablation of the top layers of the skin, congealing of the collagen fibers, changes to collagen structure or orientation, and mechanical trauma to the various layers of the skin were investigated.

## 4.4 Results

### 4.4.1 Qualitative observations of tissue sections under microscope

The tissue sections, including control, were viewed by an experienced pathologist (Dr. William Yong) in a comparative blind study. The stratum corneum, epidermis, dermis, and the epidermal-dermal junction were similar across all the irradiated specimens and control. There was no observable ablation of the top layers of the skin sample, congealing of the collagen fibers, or mechanical trauma in the various layers of the skin. The collagen structure and orientation remained intact, and no differences could be observed when compared to the control sample. There were some regions where the collagen fibers seem to have larger spaces or air pockets in between them, but such regions were also found in the control sample indicating that it is most probably an artifact related to preparation of specimens or sectioning. Figure 4.2 shows samples of tissue sections shocked with LGS of varying energy levels. The tissue section in Figure 4.2(a) have been stained with H&E stain and in Figure 4.2(b) with Masson's Trichrome stains.

### 4.4.2 Tissue Section Scoring

The scores for the tissue sections are shown in Table 4.2. The control samples were given the highest slit/ space and overall score. This suggests that the slits/spaces seen in the collagen structure are most probably a sectioning, or preparation, artifact. The high O

score given to the control sample indicates that the control sample appeared the most damaged when compared to the irradiated samples. Therefore, it is unlikely that LGS is having a detrimental effect. In addition, Table 4.2 reveals that all the samples received a high O score of either 2 or 3 suggesting that the overall appearance of all samples was similar.

9 of the 15 samples received S scores of 2. Furthermore, 3 samples received the lowest S score of 1. If the slits/spaces were indeed caused by LGS then we would expect samples shocked with 498 mJ to have the highest S score and samples shocked with 118 mJ to have the lowest S score. However, our results reveal that there is no clear pattern that can be observed in the S scores. This again suggests that the slits/spaces in the tissue sections are either inherently present in the tissue or are an artifact related to histology.

Finally, there was no apparent relationship between S and O scores and the energy level with which the samples were shocked. While further investigation and a full statistical analysis is necessary to confirm this result, it appears that treatment of the samples with LGS did not alter the overall appearance and structure of the *ex vivo* pigskin samples.

Table 4.2: Table showing the O scores and S scores of each tissue sample.

| Energy (mJ) | Energy Density (mJ/mm2) | Input Stress (at glass slide) (MPa) | Stress (at Porcine Skin) (MPa) |
|---|---|---|---|
| 118 | 16.68 | 31.85 | 6.05 |
| 149 | 21.07 | 45.87 | 8.71 |
| 228 | 32.24 | 81.53 | 15.49 |
| 264 | 37.33 | 97.79 | 18.58 |
| 350 | 49.49 | 136.61 | 25.96 |
| 400 | 56.56 | 159.19 | 30.24 |
| 498 | 70.42 | 203.44 | 38.65 |

## 4.5 Conclusions

This chapter discusses the set of experiments performed to determine the effect of LGS on *ex vivo* porcine skin. The chapter 2 discusses the experiments performed to determine the delamination threshold of biofilm. Before performing biofilm delamination experiments *in vivo* it was important that the effect of LGS on the structure of skin be assessed. If the LGS have no adverse effect on the structure of skin it will be safe to proceed with biofilm delamination experiments *in vivo*.

This was a set of preliminary experiments carried out using porcine skin and the same energy range as that used for the biofilm delamination studies 2 (0 - 500 mJ). Also experiments were performed on a very small set of samples (15). All the various structures of the porcine skin the stratum corneum, epidermis and dermis remained intact and looked similar to the control samples. As the results suggest LGS do not seem to have an adverse effect on the structure of porcine skin in the energy range of 0 - 500 mJ.

This was however a preliminary set of experiments performed on a very small set of samples. In order to be certain that LGS do not have any adverse effect on skin, similar experiments need to be performed on a much larger number of samples. Also it would be good to perform the experiments using a wider energy range and determine the damage threshold for porcine skin. This would help to obtain an energy range window which is appropriate to use for *in vivo* experiments. The following chapter 5 discusses the set of experiments performed on a much larger set of samples using a wider energy range.

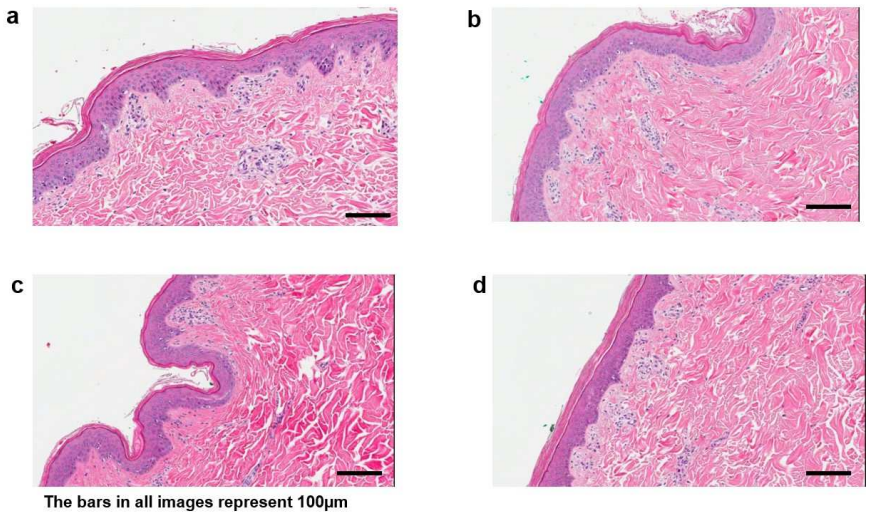


(a)

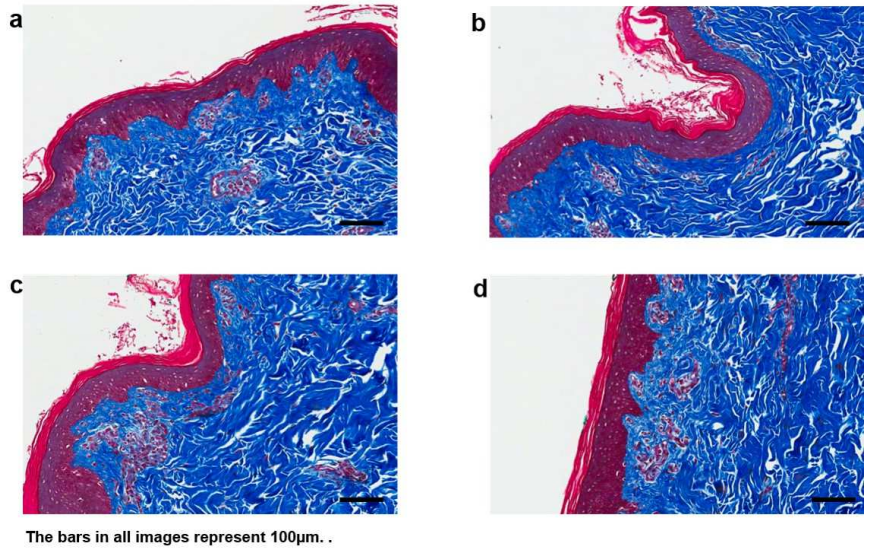


(b)

Figure 4.2: Samples of tissue sections shocked with various energy levels. They have been stained with a) H&E stain and b) Masson's Trichrome Stain

# CHAPTER 5

# Determining Damage Threshold of *Ex vivo* Porcine Skin

## 5.1 Introduction

The previous chapter discusses the set of experiments carried out to determine the effect of LGS (Laser Generated Shockwaves) on *ex vivo* porcine skin. The laser energy fluence that was used to look into the effect ranged between 100 and 500 mJ, around the energy level ($\sim$ 228 mJ) at which delamination of biofilm off a surface of petridish was observed. No damage to the porcine skin was observed in that energy range. However the goal of this set of experiments was to determine the threshold energy level at which damage to the structure of porcine skin is visible.

Future experiments involve delaminating biofilm from *ex vivo* and *in vivo* surfaces. This might lead to several changes in the experimental set up to generate shockwaves as well as to couple the shockwaves to the target surface. For instance the use of flexible polymers that can generate shockwaves with high peak stresses similar to glass will be preferred over glass. Since these flexible polymers are safer to use and can be wrapped around varying contours easily in a clinical setting. These changes can lead to changes in the energy level that will be used to delaminate the biofilm, in turn leading to changes in the energy experienced by the *ex vivo* and *in vivo* porcine skin. The knowledge of threshold energy level for damage to *ex vivo* porcine skin will help choose an optimal energy level that will delaminate the biofilm as well as not cause any damage to the underlying skin.

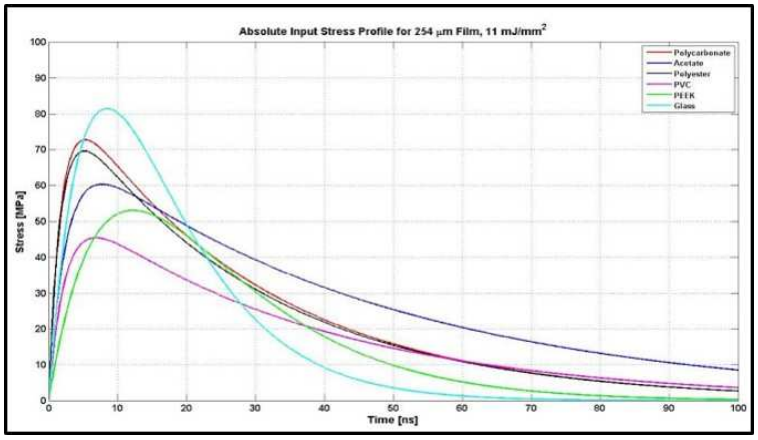


Figure 5.1: Stress generated by a particular material vs Time for a laser fluence of 11 mJ/$mm^2$. It can be seen that for a given laser fluence polycarbonate generates the highest peak stress after glass.

While these *ex vivo* experiments are being performed another set of experiments are being performed simultaneously to select an appropriate polymer which will be flexible as well as be able to generate shockwaves with high peak stresses. A number of different polymer films such as polyethylene, polystyrene, polyvinyl, polycarbonate, polypropylene and PEEK (polyetheretherketone) were examined. The Michelson interferometer was used to measure the displacement caused by the shockwave exiting the material. Using the deflection measurements and the material's mechanical properties, the velocity and the stress profile of the wave exiting the material was calculated. As shown in Figure 5.1 polycarbonate film generated the highest peak stress for a given laser fluence after glass. Thus, polycarbonate was chosen to generate the shockwaves for this set of experiments.

### 5.1.1 Effect of Laser and Laser Generated Shockwaves on Skin Tissue

A wide range of skin conditions are amenable to treatment with lasers [159]. Initial studies show that removal of the upper layers of the skin has a positive cosmetic effect. $CO_2$ and Er:YAG lasers are currently the most popular for this technique called skin re-

juvenation. Newer rejuvenating laser systems are being introduced to reduce the risk of side effects and unpleasant post operative recovery period that are associsted with $CO_2$ and Er:YAG lasers. These effects have also been achieved with mechanical systems. Histologic studies on the long-term effects of laser-resurfaced skin demonstrate elimination of epidermal atrophy and atypis, new collagen development in the dermis, proliferation of elastic fibers, homogenization of melanin distribution and a reduction in the amount of glycosaminoglycans [160]. These histological changes correlate with clinical findings of diminished fine wrinkles, enhanced color and texture and overall skin rejuvenation. However, a common side effect of these skin resurfacing methods is post-treatment erythema [159]. Sublethal thermal damage, increased vascular permeability, and collagen alterations have been proposed as etiologies for post laser erythema [159]. Recent developments in laser resurfacing technology have aimed at minimizing thermal damage to the dermis. Pigmentary disorders such as hyperpigmentation and hypopigmentation are some of the additional complications associsted with laser resurfacing. All of these must be considered when evaluating the shockwave system.Pigmentary disorders are thought to be due to the influence of the treatment on the complex microenvironment of keratinocytes, melanocytes, and collagen ?bers [161].

The effect of LGS on the structure of skin is, however, not very well known. There have been studies whereby the use of LGS for drug [162] and gene [120] delivery through skin has been explored. Doukas et al. showed that LGS produced using a Q switched ruby laser(694 nm wavelength and $\sim$ 28ns pulse duration) increases the permeability of the stratum corneum *in vivo* in humans [162]. The onset of permeabilization was observed at 35 MPa and increased with increasing peak pressure. During the transient period of increased permeability, macromolecules diffused through the stratum corneum to the epidermis and dermis. While pressure waves of 300 ns duration did not produce any negative sensation, pressure waves of 1 ms duration generated a noticeable sensation, but not pain [162]. With respect to skin changes, after the application of a pressure

wave, the 300 ns pressure wave did not produce signi?cant changes to the appearance of skin, while the 1ms pressure wave produced a minor erethyma, which disappeared within 10 to 15 minutes. The stratum corneum eventually did recover its barrier function within 15 minutes when water was used as the coupling medium [162]. Ogura et al. [120] demonstrated *in vivo* gene transfer using LGS generated by a Nd:YAG laser. Results revealed that rats injected with plasmid DNA and subsequently irradiated with LGS had luciferase activity at two orders of magnitude higher than controls. The peak pressures used in the study were estimated to be in the range of 15-75 MPa, with energy densities corresponding to 4-19 mJ/mm$^2$. At this fluence, one third of the rats showed erythema in the shockwave-exposed skin, but the effect disappeared within a week. Irradiation with more than three pulses caused erythema in all shockwave exposed skin which also disappeared within a week. Thus, no major side effect on skin was observed. The energy density and peak stresses generated in the present experiments were significantly higher than those used in previous experiments [162] [120] [161]. Yet, the current study shows that a single Nd:YAG laser generated shockwave pulse ($3-6$ ns)ranging from $16.68-70.42$ mJ/mm$^2$ of energy can be made incident on skin without damaging its collagen structure. The peak pressures of the LGS produced by Doukas [162] and Ogura [120] lie between $15-75$ MPa. Previous studies by our group have shown that it is possible to delaminate biofilm off surfaces using similar LGS pulses generated by Nd: YAG laser [163]. The most notable advantage of using LGS to delaminate biofilm from wound surfaces compared to methods such as ultrasound is the absence of the deleterious effects of tensile wave components and cavitation bubbles on skin tissue. In addition, given the precision of lasers we can expect to deal with biofilm delamination in a more controlled manner as compared to debridement of the biofilm from the wound which is the current gold standard for treating biofilm infected wounds. It is not clear whether the LGS kill the bacteria embedded in the delaminated biofilm. This question remains to be answered.

## 5.2 Materials and Methods

### 5.2.1 Specimen Preparation

The porcine model was chosen as it has been used as a model for human skin in the past due to its similarities to human skin both physiologically and anatomically [151] [152]. Porcine skin specimens were harvested from the abdominal region of a pig immediately post-mortem. The specimen was cut into square shaped pieces of 5 mm length using a scalpel and blade. Each resulting specimen was maintained at room temperature (25°C) throughout the experiment, and not frozen, so as not to alter the structure or mechanical properties of the collagen fibers. LGS treatment was carried out no more than 30 minutes after specimens were harvested.

### 5.2.2 Substrate Preparation

Polycarbonate sheets with dimensions of 3 x 1 inch and 5 $\mu$m in thickness were RF sputtered (Denton Discovery II 550, Denton Vacuum, NJ USA) with 0.5 $\mu$m thick layer of Ti. A layer of waterglass was then spin-coated on top of the Ti to achieve a uniform layer of $50-100$ $\mu$m. The waterglass layer acts as the constraining layer and is transparent to the Nd:YAG laser wavelength of 1.064 $\mu$m.

### 5.2.3 Shockwave Generating System and Laser Parameters

A Q-switched, Nd:YAG laser was used to generate LGS. A 3 - 6 ns long Nd:YAG laser pulse is impinged over a 3 mm dismeter area on the 0.5 $\mu$m Ti sandwiched between the back surface of the polycarbonate sheet and the layer of waterglass. Laser-generated pulses impinging upon the thin metallic surface generate stress waves within the material. The laser energy then ablates the thin metallic film, thereby causing a rapid thermal expansion

of the film resulting in a compressive wave propagating through the substrate. The laser fluence, pulse width and the substrate material properties contribute to the temporal characteristics of the stress wave. The peak stress, rise time of the wave, and the stress profile generated are dependent on the above-mentioned parameters.

## 5.3 Experimental Procedure

The porcine skin sample was placed in a petridish. The porcine skin was held in place by placing it in between two acrylic blocks glued to the base of the petridish. Ultrasound gel of $\sim 1-2$ mm was then applied on the top surface of the porcine skin. The ultrasound gel was used as a coupling agent between the porcine skin sample and the polycarbonate sheet. Ultrasound gel was chosen instead of deionized water as has been used in the previous experiments because it will be more suitable for use in a clinical setting. The shockwaves were made to be perpendicularly incident on the porcine skin sample as described in the previous chapter 4 and as shown in Figure 5.2.

Each sample was subjected to LGS of a particular laser fluence ranging from 0.25 - 1.5 J. The precise laser fluences and corresponding energy density generated by the laser are shown in Table 5.1. There were 15 samples per energy level and 15 control samples.

### 5.3.1 Sample Preparation for Analysis

Immediately after shocking, the samples were fixed in formaldehyde and prepared for paraffin histology. Specimens were sectioned sagitally at 5 $\mu$m along the midline, coinciding with the center of 3 mm shocked region. This region should correspond to the maximum mechanical impact generated by the laser shockwaves. The sections were then stained using H&E stain.

The tissue sections were scored on the basis of two criteria: Superficial Damage (S)

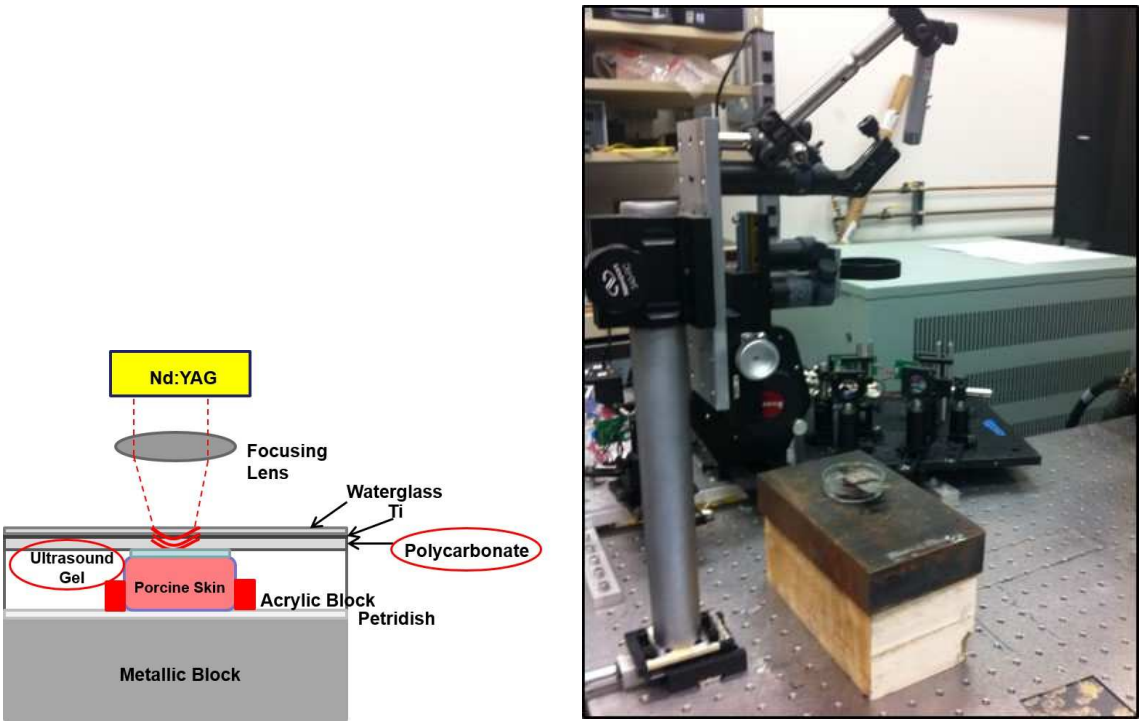


(a) (b)

Figure 5.2: Images showing a) Schematic Diagram b) Actual Image of experimental set up to determine damage threshold of *ex vivo* porcine skin.

and Deep Damage (D) to the skin. Superficial Damage refers to damage to the top layers of the skin namely the stratum corneum and epidermis. Deep Damage refers to damage to the layers of the skin that lie deep within namely the dermis. The scores were given on a scale from 0 to 3.

While assessing for 'Superficial Damage', the top region of the tissue sections namely the stratum corneum and epidermis were examined to ascertain whether they were intact, whether there were signs of mechanical trauma and whether they had gaps or slits. A 'S' score of 0 indicates that the stratum corneum and epidermal layers of the sample is is intact with no signs of damage and no slits or gaps whereas a 'S' score of 3 indicates that the sample is severely damaged. Figure 5.3 shows sample tissue sections that received scores from 0 to 3.

Table 5.1: Energy density corresponding to each energy fluence used in the experiment.

| S. No. | Energy Fluence (mJ) | Energy Density (mJ/mm ^ 2) |
|---|---|---|
| 1 | 250 | 35.38 |
| 2 | 500 | 70.77 |
| 3 | 750 | 106.14 |
| 4 | 1000 | 141.52 |
| 5 | 1250 | 176.9 |
| 6 | 1500 | 212.28 |

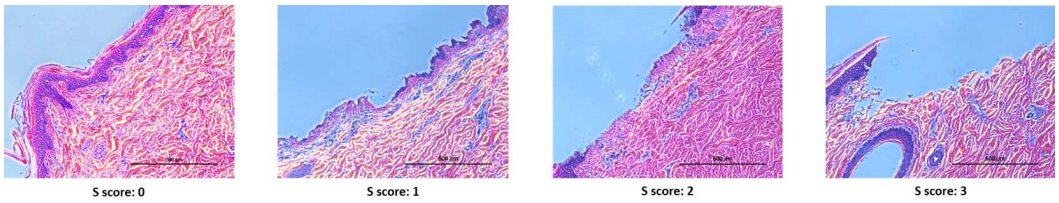


Figure 5.3: Sample tissue sections stained with H&E stain that received S scores from 0 to 3.

While assessing for 'Deep Damage', the deep regions of the tissue sections namely the dermis which contains collagen fibers was examined to look for congealing of collagen fibers, changes to the structure and orientation of the collagen fibers and gaps or slits in the collagen region. A 'D' score of 0 indicates almost no damage to the collagen structure of the sample while a 'D' score of 3 indicates extensive damage to the collagen structure. Figure 5.4 shows sample tissue sections that received scores from 0 to 3.

### 5.3.2 Results

The experiment was carried out for 6 different energy levels namely, 0.25 J, 0.5 J, 0.75 J, 1 J, 1.25 J and 1.5 J. One set of control samples was also included. For each energy level as well as the control there were 15 samples. As a result, there was a total of 105 samples.

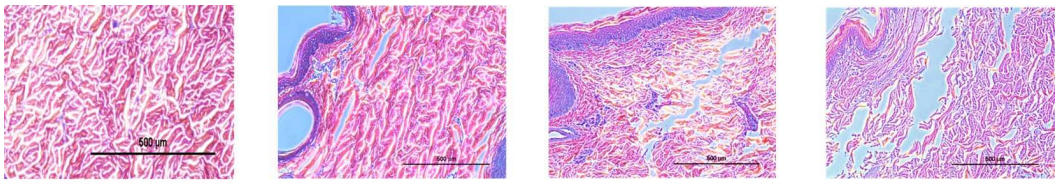


Figure 5.4: Sample tissue sections stained with H&E stain that received D scores from 0 to 3.

Each sample was bisected during histological analysis and each of the two sections was analyzed for S score and D score. The energy levels and their corresponding scores is presented in Appendix A .

#### 5.3.2.1 Qualitative Results

The tissue sections were analyzed and the predominant observation i.e. the observation that occurred for most of the samples at a particular energy level was recorded as shown in Table 5.2. This analysis helped analyze qualitatively whether increase in the energy with which the samples were shocked had an increasingly detrimental effect on the *ex vivo* porcine skin samples. This analysis helped obtain an idea about which energy levels were safe to use on porcine skin and which energy levels were causing serious damage to the structure of the skin.

As can be seen from Table 5.2, the damage caused to *ex vivo* porcine skin is increases in severity with increase in the energy level with which it is treated. There is no damage caused to the porcine skin samples upto 0.5 J of energy. Slight damage is caused to the porcine skin samples at energy levels between 0.75 - 1.25 J of energy. Much damage seems to be caused at 1.5 J (212.28 mJ/$mm^2$) of energy.

The qualitative analysis provides a rough estimate of the effect of a particular energy level on *ex vivo*porcine skin. We can also observe whether there is a trend in the

Table 5.2: Table showing the predominant observation for each energy level

| | Predominant Observation | |
|---|---|---|
| Energy Fluence | Stratum Corneum and Epidermis | Collagen structure of Dermis |
| Control | No damage | No damage |
| 0.25J | No damage | No damage |
| 0.5J | No damage | No damage |
| 0.75J | Irregularities in structure | Slight damage |
| 1J | Small regions blown off | Small Slits/pores |
| 1.25J | Regions blown off | Slits/pores |
| 1.5J | Large regions blown off | Large empty spaces |

damage to porcine skin caused by increasing the energy level with which it is shocked. However, in order to ascertain whether the damage caused by a particular energy level is significant and whether there is a particular energy level which can be considered the damage threshold i.e. the energy level above which significant damage to the skin will be caused, statistical analysis on the data provided in Appendix A needs to be carried out.

#### 5.3.2.2 Quantitative Analysis

Two types of analysis were performed on the data:

**Comparing mean scores of all energy levels** The mean scores (S scores and D scores) of each energy level were plotted to observe any trend in damage caused by increasing the energy with which the samples were shocked. Figure 5.5(a) and Figure 5.5(b) show the graph of mean score vs energy level for S scores and D scores respectively. As can be seen from the graphs for both S scores and D scores, there is a positive correlation between mean scores for damage of the porcine skin samples and the energy level with which the samples are treated. As the energy level increases the mean score also increases. We can be certain that the two variables namely the scores for the damage and the energy level are positively correlated since no other parameter was varied during the experiment.

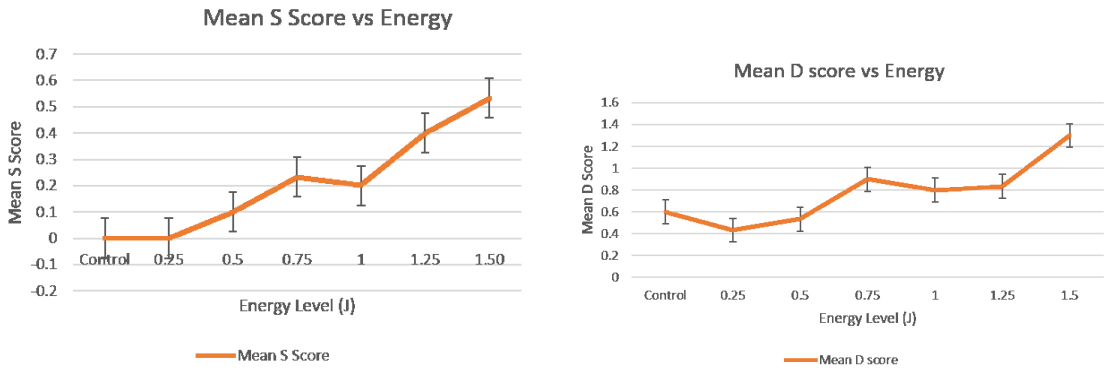


(a) (b)

Figure 5.5: a) Mean S scores vs Energy and b) Mean D scores vs Energy

**Two-sample mean-comparison test** A two-sample mean-comparison test which is essentially a student t-test was performed comparing the samples in the control group to those of each energy level. This test would help decide whether the two groups of samples being compared are essentially the same. This would imply that any differences between the scores of the two groups is purely due to random errors and not systematic errors. For this particular set of experiments, if the two groups being compared are considered to be the same, it implies that the control samples and the samples shocked with the particular energy level are appear to be the same. In other words, that particular energy

level does not have any effect on the structure of *ex vivo* porcine skin. If at any particular energy level significant difference between the particular group and control samples is observed that particular energy level can be considered as the damage threshold for *ex vivo* porcine skin above which significant damage to the porcine skin can be observed.

The results of the test are shown in Table 5.3 and Table 5.4. 95% significance level was chosen in order to test the null hypothesis. Since the groups being compared had unequal variances, welch's approximation was applied while carrying out the test. As can be seen from both the tables the null hypothesis was accepted for all pairs except between the control samples and those that were shocked with 1.5J of energy. This implies that the samples shocked with 1.5 J of energy were significantly different from the control samples. Consequently we can infer that 1.5 J of energy is causing significant damage to *ex vivo* porcine skin. Hence, 1.5 J (212.28 mJ/$mm^2$) can be considered as the damage threshold for porcine skin.

## 5.4 Conclusions

This chapter discusses the set of experiments performed to determine the damage threshold of *ex vivo* porcine skin. These experiments were performed on a larger set of samples and wider range of energies as compared to the experiments performed in the previous chapter 4. These set of experiments helped determine the energy at which significant damage to the porcine skin is observed.

These set of experiments were performed using 105 samples, 15 samples for each energy level and 15 control samples. The range of energies used in these experiments was 0-1500 mJ. Statistical analysis showed that the samples shocked with 1500 mJ of energy appeared significantly different from control samples and therefore had undergone significant damage.

Table 5.3: Student t-test comparing S scores of each energy level to scores of control at 95% significance

| Groups compared | Welch's df (degrees of freedom) | Pr ( \|T\| > \| t\| ) | Null Hypothesis |
|---|---|---|---|
| Control and 0.25 | - | - | Accepted (essentially the same group) |
| Control and 0.50 | 14 | 0.33 | Accepted |
| Control and 0.75 | 14 | 0.29 | Accepted |
| Control and 1.00 | 14 | 0.054 | Accepted |
| Control and 1.25 | 14 | 0.089 | Accepted |
| Control and 1.50 | 14 | 0.044 | Rejected |

With the help of experiments in this chapter as well as the experiments in chapter 4 a favorable energy window to be used for *in vivo* experiments was obtained. This energy window will be useful to begin *in vivo* experiments. Using energies in this energy window will ensure that the biofilm will be delaminated and that the skin will not be damaged. There will obviously be some differences between performing experiments *in vitro* and *in vivo*, but the energy window obtained is a good estimate to begin with.

Table 5.4: Student t-test comparing D scores of each energy level to scores of control at 95% significance

| Groups compared | WelchŠs df (degrees of freedom) | Pr ( \|T\| > \| t\| ) | Null Hypothesis |
|---|---|---|---|
| Control and 0.25 | 29.73 | 0.53 | Accepted (essentially the same group) |
| Control and 0.50 | 29.97 | 0.78 | Accepted |
| Control and 0.75 | 24.74 | 0.38 | Accepted |
| Control and 1.00 | 29.04 | 0.47 | Accepted |
| Control and 1.25 | 29.57 | 0.38 | Accepted |
| Control and 1.50 | 28.178 | 0.022 | Rejected |

# CHAPTER 6

# Modeling Laser Generated Shockwaves using COMSOL

## 6.1 Introduction

This chapter discusses the modeling of LGS (Laser-Generated Shockwaves) using COMSOL. The propagation of LGS through the coupling medium, biofilm and muscle was modeled. The various layers of the experimental set up used in this model are shown in Figure 6.1 .This model will be useful for predicting the outcome of future experiments. Performing experiments using different materials and methods in order to get improved results is tedious, time consuming and requires investment of time, effort and money. This model will be able to predict an approximate outcome of the experiment without actually performing the experiment. This will help eliminate new materials and methods much more easily. Using this model one can get an estimate of the amount of compressive and tensile pressure ultimately reaching the biofilm/muscle interface. Since the goal is to be able to delaminate the biofilm and at the same time ensure no damage to the underlying muscle tissue, one can use the model to ascertain whether there will be enough tensile stress at generated at the biofilm/muscle interface to delaminate the biofilm and at the same time cause no damage to the muscle tissue.

The model will also be capable of predicting the nature of interaction between two LGS made incident at a particular time interval. It will be able to estimate the time of arrival of the first tensile wave at the biofilm/muscle interface as well as its magnitude. This will help decide on the optimum combination of LGS that should be used to get the most favorable results.


Figure 6.1: The various layers of the experimental set up used in COMSOL model

### 6.1.1 Physics of the Model

The LGS while propagating through the various layers of the experimental set up such as ultrasound gel, biofilm and muscle undergoes damping due to the visco-elastic nature of the materials. The lossy wave equation which governs the propagation of acoustic waves through visco-elastic materials was used to model the LGS. The derivation and origin of the lossy wave equation is explained by Erlend Magnus Viggen [164]. Below is a brief description of the lossy wave equation:

Conservation of mass and momentum is expressed through the continuity and compressible Navier-Stokes equations, which relate density $\rho$, pressure p, and particle velocity u,

$$\frac{\partial \rho}{\partial t} = -\bigtriangledown .(\rho u) \tag{6.1}$$

and

$$\rho \frac{Du}{Dt} = -\bigtriangledown p + \rho(\frac{4}{3}\nu + \nu')\bigtriangledown(\bigtriangledown .u) - \rho\,\nu \bigtriangledown \times \bigtriangledown \times u \tag{6.2}$$

Assuming low Mach number, adiabatic compression, and sufficient distance to boundaries, it may be shown similarly that this implies a lossy wave equation,

$$\left(1 + \tau_\nu \frac{\partial}{\partial t}\right)\bigtriangledown^2 p - \frac{1}{c_s^2}\frac{\partial^2 \rho}{\partial t^2} = 0 \tag{6.3}$$

where

$$\tau_\nu = \left(\frac{4}{3}\nu + \nu'\right)/c_s^2 \tag{6.4}$$

is the viscous relaxation time. Also, $c_s$ is the speed of sound in that particular material and $\nu'$ & $\nu$ are the bulk and shear viscosities respectively and are related by the equation:

$$\nu' = \frac{2\nu}{3} \tag{6.5}$$

## 6.2 Materials and Methods

### 6.2.1 1D Modeling of LGS Propagation

The LGS propagation was modeled using 1D modeling. We could safely assume that the propagation of the LGS is uniform across its entire spacial distribution because the laser spot size is much greater than the thickness of the material through which it travels.

Modeling the LGS in one dimension made the simulations work faster and as well as caused much lesser computational load on the computer.

### 6.2.2 Material Properties

The material properties used for the modeling the experimental set up are presented in Table 6.1. The properties of a high viscosity ultrasound gel is used in the model since it is used most often in clinical settings. The viscosity of biofilm has a very wide range of values depending on the organism producing it and the conditions under which it is produced. In this particular model, the viscosity of biofilm is considered to be same as the viscosity of water. The viscosity of muscle also varies widely depending on the type of muscle and where it is located in the body. The viscosity of muscle tissue also varies with the magnitude of stress applied as well as the strain rate produced in the muscle. There was no obvious reason to choose one type of muscle over the other since a biofilm infected wound can occur almost anywhere in the body. Moreover, the strain rate applied in this particular experiment is very high $\sim 10^6$. The values of viscosity of muscle reported in the literature have been studied under strain rates which are much

lower than that used in this experiment. In this model the viscosity of muscle used is that of ballistic gel. Ballistic gels are used to mimic the human muscle in studies that look into the effect of high impact on human muscle which involve high strain rates and are therefore more suitable for our studies.

Table 6.1: Material properties of the materials used in the COMSOL model

| Material | Speed of Sound*,cs (m/s) | Bulk Viscosity*, (Pa.s) | Shear Viscosity*, (Pa.s) |
|---|---|---|---|
| Ultrasound Gel | 1497 | 100 | 66.66 |
| Biofilm | 1540 | 8.9e-4 | 5.93 |
| Muscle | 1600 | 100 | 66.66 |

## 6.3 Results

### 6.3.1 Modeling Propagation of Single Shockwave

This section describes the modeling of a single LGS propagation. The propagation of LGS through ultrasound gel, biofilm and muscle tissue was modeled. Using this model the nature of interaction between the shockwave and the various materials in the experimental set up can be studied.

For a particular input stress at the ultrasound gel, this model can help determine the intensity of the tensile wave that causes the delamination of biofilm. It can also help determine the intensity of the compressive wave that enters into the muscle. If the stress that causes delamination of biofilm from the muscle as well as the damage threshold for the muscle is known, the optimal value of input stress to the ultrasound gel can be determined. In addition the time at which the tensile wave reaches the biofilm-muscle interface can be determined using this model. This information will be helpful in designing experiments in the future where more than one single pulse of shockwave is

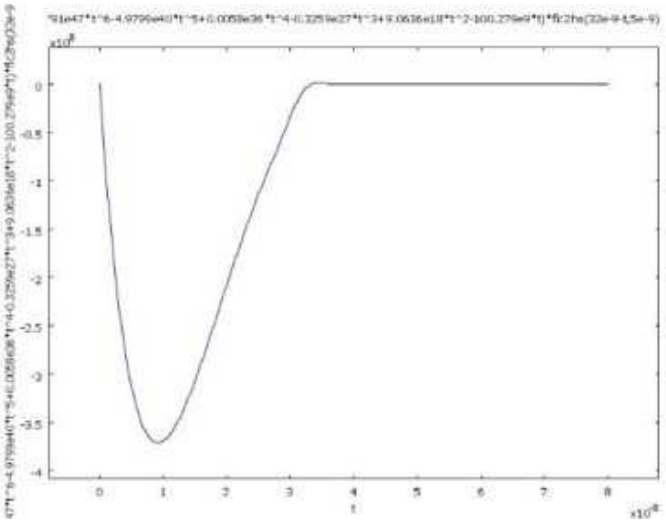

Figure 6.2: The waveform of the single shockwave used in the COMSOL model.

introduced into the experimental setup.

#### 6.3.1.1 Input and Boundary Conditions for the Model

The input for this model is the shockwave generated by impinging laser energy on glass/polycarbonate sandwiched between a layer of Ti and waterglass as explained in Chapter 1. Figure 6.2 shows the waveform. The expression that governs the waveform is given by:

$$(1.6791e^{47}.t^6 - 4.9799e^{40}.t^5 + 0.0058e^{36}.t^4 - 0.325e^{27}.t^3 + 9.0636e^{18}.t^2$$

$$-100.279e^{9}.t).flchs(32e^{-9} - t, 5e^{-9}).e^{6}$$

There were no special boundary conditions imposed on internal interfaces i.e. the ultrasound-biofilm interface and the biofilm-muscle interface. The shockwave was made to propagate through each of these interfaces, which resulted in a part of the wave being propagated as a compressive wave and part of it being reflected as a tensile wave. The magnitude of the wave being propagated and reflected depended on the impedance of the two materials present at the interface.

The end of the muscle was treated as a free surface, i.e. the stress at the end of the muscle was considered as 0.

#### 6.3.1.2 Determining Tensile Stress and Time of Arrival of the Tensile Stress

The results presented in this section are for the input compressive wave as shown in 6.3.1.1.

An animation showing the propagation of LGS through the various materials in the experimental set up can be viewed by visiting the link: http:youtu.be/f759Y_HoMxA. As can be seen in the animation, when a shockwave is introduced into the ultrasound material it propagates though the three materials undergoing some damping and hence some reduction in its magnitude. The amount of reduction in magnitude depends the physical properties of the material such as speed of sound in that particular material and the bulk and shear viscosities of the material. At the ultrasound gel-biofilm interface some amount of the wave propagates propagates as a compressive wave into the biofilm and a part of it gets reflected as a tensile wave back into the ultrasound gel. The proportion of the wave that propagates and gets reflected dependence on the impedance mismatch between the two materials. As the impedance mismatch between the materials increases, the amount of the incoming wave being reflected as a tensile wave will increase. The same process occurs at the biofilm/muscle interface too. Since there is hardly any impedance mismatch between the biofilm and muscle most of the wave propagates into the muscle as a compressive. Upon reaching the end of the muscle the wave reflects back as a tensile wave, which propagates through the muscle and reaches the biofilm-muscle interface. Again, the impedance mismatch between biofilm and muscle is not much so the tensile wave propagates through the muscle into the biofilm. This tensile wave causes delamination of the biofilm.

The variation of pressure with time at the biofilm-muscle interface is of particular

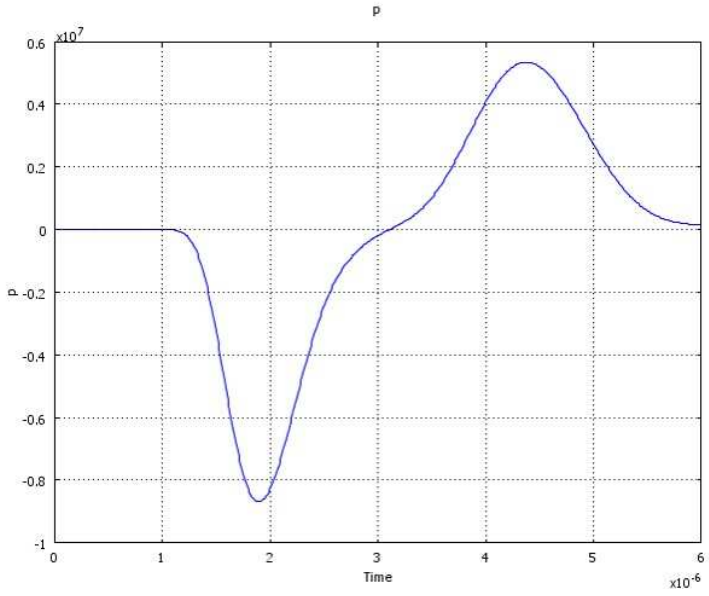


Figure 6.3: Variation of pressure with time at the biofilm-muscle interface as the single shockwave propagates through the materials.

interest for the purposes of this study. Figure 6.3 shows the variation of pressure with time at the biofilm-muscle interface. As can be seen in the figure, initially at $\sim$ 1200ns a compressive wave passes through the biofilm-muscle interface and then it experiences a tensile wave at $\sim$ 300ns. The input compressive wave has a magnitude of 360MPa and the corresponding tensile wave at the biofilm-muscle interface has a magnitude of $\sim$ 5.6MPa.

### 6.3.2 Modeling Propagation of Two Shockwaves

This section describes the modeling of the propagation of two shockwaves. Two identical shockwaves are made incident at a particular time interval. The model describes how the two shockwaves interact with one another as well as with the materials in the experimental set up, namely the ultrasound gel, biofilm and the muscle. This model can be used to find the magnitude of the tensile stress that will cause the delamination of the

biofilm. It also gives the time of arrival of the tensile wave at the biofilm/muscle interface.

In an actual clinical setting, more than one shockwave will be used to delaminate the biofilm from the muscle. Hence it is important to know how two shockwaves made incident on the wound at a particular time interval will interact with each other. It is also important to know whether they will be producing a synergistic effect resulting in an increase in the tensile wave pressure or whether the tensile wave pressure that causes the delamination will decrease. The time of arrival of the tensile wave at the biofilm-muscle interface is also important to know in order to design the system. This model will be able to provide all the above information. This model can be further used if more than two shockwaves are desired to be applied using simple modifications.

#### 6.3.2.1 Input and Boundary Conditions for the Model

The input for this model is two shockwaves made incident at a particular time interval. The shockwave is generated by impinging laser energy on glass/polycarbonate sandwiched between a layer of Ti and waterglass as explained in Chapter 1. Figure 6.4 shows the waveform. The expression for the model input is given by:

$$((1.6971e^{47}.t^6 - 4.9799e^{40}.t^5 + 0.0058e^{36}.t^4 - 0.3259e^{27}.t^3 + 9.063e^{18}.t^2$$

$$-100.279e^{9}.t) * flchs(32e^{-9} - t, 5e^{-9}) + (1.6971e^{47}.(t - T + 5e^{-9})^6) -$$

$$4.9799e^{40}.(t - T + 5e^{-9})^5 + 0.0058e^{36}.(t - T + 5e^{-9})^4 - 0.3259e^{27}.(t - T + 5e^{-9})^3$$

$$+9.063e^{18}.(t - T + 5e^{-9})^2 - 100.279e^{9}.(t - T + 5e^{-9})) * flc2hs(t - T, 5e^{-9}))$$

$$*flc2hs(T + 27e^{-9} - t, e^{-9})) * e^6 - p$$

where T is the time interval between the two shockwaves.

There were no special boundary conditions imposed on internal interfaces i.e. the ultrasound-biofilm interface and the biofilm-muscle interface. The shockwave was made

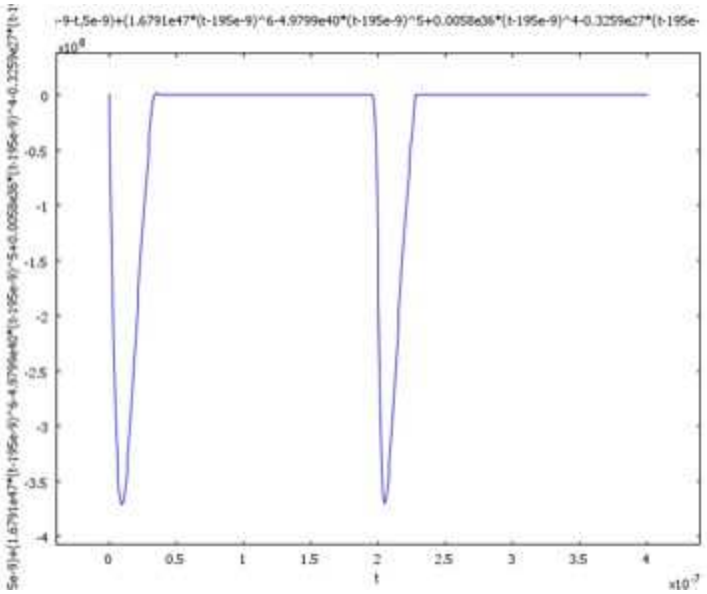


Figure 6.4: The waveform for the two shockwaves used in the COMSOL model. In this figure the two shockwaves are separated by a time interval of 2000 ns

to propagate through each of these interfaces, which resulted in a part of the wave being propagated as a compressive wave and part of it being reflected as a tensile wave. The magnitude of the wave being propagated and reflected depended on the impedance of the two materials present at the interface.

The end of the muscle was treated as a free surface, i.e. the stress at the end of the muscle was considered as 0.

#### 6.3.2.2 Determining Combined Tensile Stress and Time of Arrival of Tensile Wave

The results presented in this section is for the input compressive waves described in 6.3.2.1.

A sample animation showing the propagation and interaction of two LGS through the various materials in the experimental set up can be viewed by visiting the link: https:www.youtube.comwatch?vf̄759Y_HoMxA. The animation shows the propagation

of two shockwaves made incident 2000ns apart. The nature of interaction between the two shockwaves and the shockwaves and the materials vary depending on the time interval they at which they are made incident. They can be classified into the following 4 intervals:

1. T<700 ns: When the time interval between the two shockwaves is less than 700 ns the two waves combine to form a single wave. The amplitude as well as time interval of the combined wave is more than that of a single wave. This combined single wave moves through all the three materials and results in a single tensile wave at the biofilm-muscle interface causing delamination of the biofilm.

   As the time interval between the two waves increases the amplitude of the combined wave decreases. At a 10 ns interval the increase in amplitude is 100% and at 700 ns the increase in amplitude is reduced to 42%. Figure 6.5 shows the variation in pressure with time at the biofilm-muscle interface when the two shockwaves are made incident 300 ns apart. Both the input shockwaves have an amplitude of 360 MPa, the resultant tensile wave at the biofilm-muscle interface has a magnitude of $\sim$ 10 MPa. Thus, the increase in amplitude at 300 ns is $\sim$ 78%.

2. 700 ns<T<1200 ns: When the time interval between the two shockwaves lies in between $700 - 1200$ns the waves combine to form a single wavefront with two distinct peaks. This wavefront propagates through the three materials and results in a single tensile wave at the biofilm-muscle interface that causes the delamination of biofilm.

   As the time interval between the two waves increases the separation between the peaks of the compressive as well at as tensile wave increases. At 1200 ns complete separation of the two tensile waves is seen. When the two waves are separated the amplitude of the waves is the same as that of a single wave. Figure 6.6 shows the variation of pressure with time at the biofilm-muscle interface for two waves at an

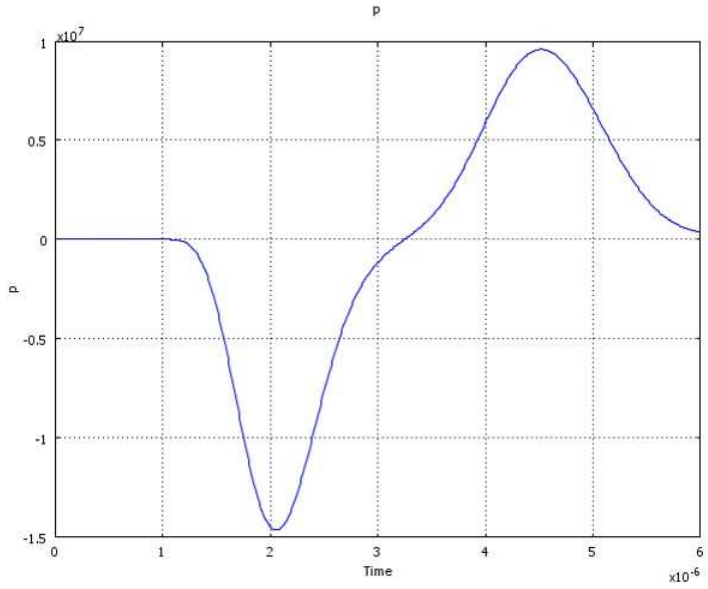


Figure 6.5: Variation of pressure with time at biofilm-muscle interface when the two shockwaves are made incident 300 ns apart.

interval of 1000 ns. Each incident shockwave has an amplitude of 360 MPa and the resultant tensile wave has an amplitude of $\sim$ 6MPa. Figure 6.7 shows the variation of pressure with time when the two waves are made incident 1200 ns apart. Here we begin to see the separation of the two tensile waves. The resultant amplitude being almost the same as that produced by a single shockwave $\sim$ 5.6 MPa.

3. 1200 ns<T<2450 ns: When the time interval between the two shockwaves lies between 1200 and 2450 ns the two waves propagate through the materials as single shockwaves. When the first wave results in a tensile wave at the biofilm-muscle interface, the second incoming compressive wave is present at the interface. As a result of interaction between the reflected tensile wave and the incoming compressive wave, the amplitude of the tensile wave is reduced.

   The amplitude decreases with increasing time interval between the two shockwaves. When the time interval between the two shockwaves is 2450 ns the de-

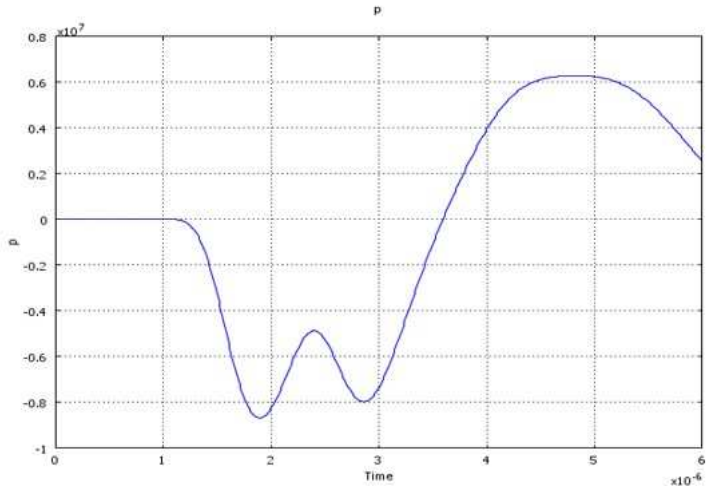


Figure 6.6: Variation of pressure with time at biofilm-muscle interface when the two shockwaves are made incident 1000 ns apart

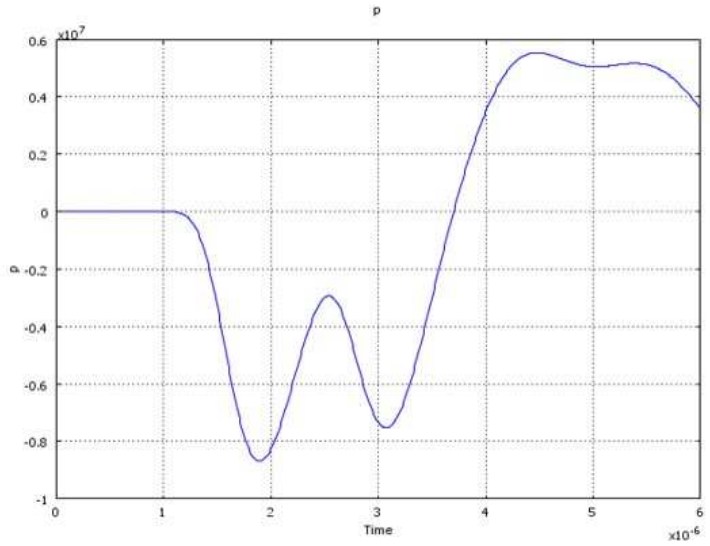


Figure 6.7: Variation of pressure with time at biofilm-muscle interface when the two shockwaves are made incident 1200 ns apart

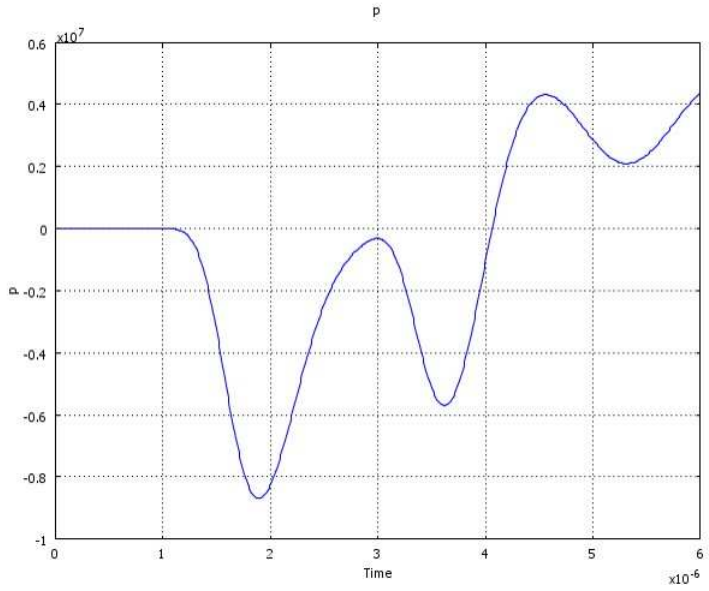


Figure 6.8: Variation of pressure with time at biofilm-muscle interface when the two shockwaves are made incident 1800 ns apart

crease in amplitude is 70%. Figure 6.8 shows the pressure at the biofilm-muscle interface when the two shockwaves are made incident 1800 ns apart. The incident shockwaves have an amplitude of 360 MPa and the resultant tensile wave at the biofilm-muscle interface has an amplitude of $\sim$ 5 MPa.

4. 2450 ns<T<3400 ns: When the time interval between the two shockwaves lies in between $2450-3400$ns the interaction between the reflected tensile wave and the incoming compressive wave reduces. At 2450ns we begin to see the reflected tensile wave and the second incoming compressive wave as two separate waves.

   As the time interval increases the interaction between the reflected tensile wave and incoming compressive wave decreases. As a result the amplitude of the reflected tensile wave causing delamination increases. At 3450 ns the two waves behave independent of each other. At 3450 ns and beyond the amplitude of the tensile wave is the same as that produced by a single shockwave. Figure 6.9shows the

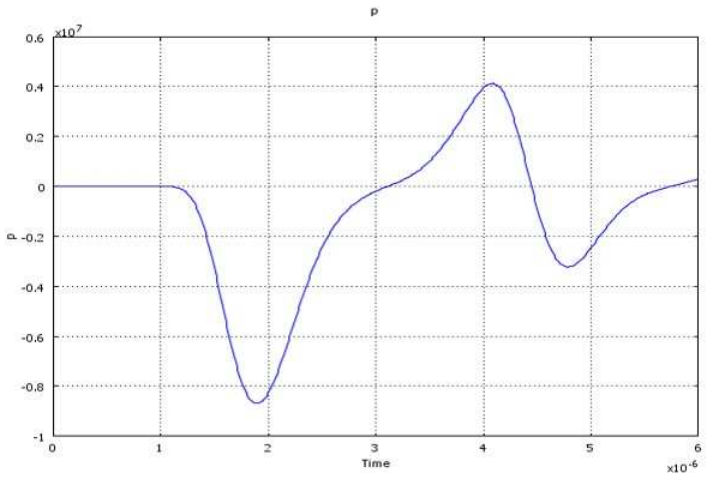


Figure 6.9: Variation of pressure with time at biofilm-muscle interface when the two shockwaves are made incident 2800 ns apart

pressure at biofilm-muscle interface when the two shockwaves are 2800 ns apart. The incident shockwaves have an amplitude of 360 MPa and the reflected tensile wave at biofilm-muscle interface has an amplitude of $\sim 4$ MPa. Figure 6.10 shows the pressure variation at the biofilm-muscle interface when the two waves are 3400 ns apart. As can be seen the two waves behave independent of each other and the reflected tensile wave has an amplitude same as that produced by a single wave i.e. $\sim 5.6$MPa.

Figure 6.11 summarizes the above results. It shows the variation in amplitude of the reflected tensile wave with time. Where T is the time interval between the two input shockwaves.

### 6.3.3 Verification of Model

The current model was verified using two methods:

1. Verification with analytical model of LGS propagation: An analytical model of LGS propagation based on the materials properties such as the density and speed of

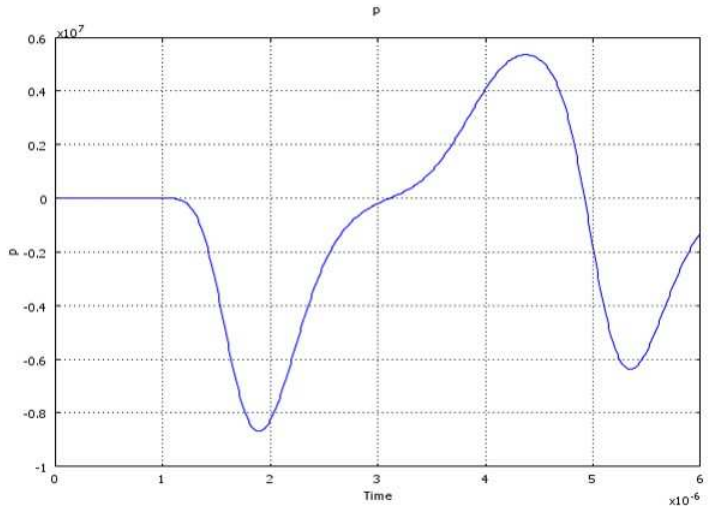


Figure 6.10: Variation of pressure with time at biofilm-muscle interface when the two shockwaves are made incident 3400 ns apart

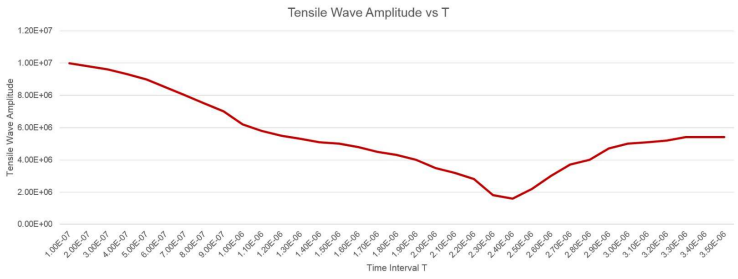


Figure 6.11: The variation of the tensile wave at the biofilm-muscle interface with respect to the time interval between the two shockwaves

sound in the material was prepared. The stress at the interfaces i.e. the ultrasound gel-biofilm and the biofilm-muscle interface was calculated. The stresses calculated using the analytical model were the same as those obtained from the COMSOL model. The damping of the wave was not considered in both the models.

2. Verification using a previous model: The stresses at the interfaces were calculated using a model prepared by a former graduate student. The same inputs were given to the current COMSOL model and the resultant stresses at the interfaces were calculated. The stresses at the interfaces were the same from both the models. Damping of the waves was not considered in the model.

## 6.4 Limitations of the Model

This model was built to simulate the propagation of LGS through the coupling medium, biofilm and the underlying muscle tissue. It was built to streamline and eliminate the need to perform experiments unnecessarily in the future. In case any parameter in the experimental set up needs to be changed, and the experimental outcome is not certain, the experimental outcome with those parameters can be determined using the model. If the outcome seems suitable that particular parameter can be used in the experiment to determine the outcome experimentally. As can be seen using the model will greatly help in saving time, resources and efforts.

However, this model is only a preliminary attempt at simulating the experimental set up. The outcomes predicted by this model are not completely accurate. The following are the limitations of the model:

1. The calculations for tensile stress at interfaces performed by this model are based on 1D propagation of LGS. 1D propagation of the LGS was assumed based on the fact that the laser spot size is much larger than the thickness of the material through

which the LGS travels. However, this condition does not hold true for all the materials through which the LGS travels. As a result the tensile stress experienced by the materials will vary across the area and 1D propagation of the LGS cannot be assumed.

2. The physical properties of muscle vary widely depending on age, sex, health condition, type of injury and location of the muscle in the body. Also muscle is composed of a number of different types of muscle fibers which gives it a heterogeneous composition and hence the physical properties of the muscle also vary spatially. In this model however, the physical properties of the muscle were considered to be similar to that of ballistic gel. Ballistic gels do mimic muscle well but they are not the best model for muscle under the effect of LGS with high peak stress and extremely short rise times. Also the physical properties of ballistic gels are considered uniform throughout which is not the case with actual muscle. Hence a better model which mimics the physical properties of muscle better should be considered.

3. As can be seen from the LGS propagation animations, the LGS propagates through the materials namely; ultrasound gel, biofilm and muscle. On reaching the end of the surface of the muscle the LGS reflects as a tensile wave, reaches the biofilm/muscle interface and then causes delamination of the biofilm from the surface of the muscle. This happens because in this model the end of the surface of the muscle is considered a free surface (Stress $= 0$). This is however not the case *in vivo*. The end of the surface of the muscle is usually bound by bone or skin and is not a free surface. This difference will effect the manner in which the LGS travels through the materials and ultimately cause delamination of the biofilm.

## 6.5 Conclusions

This model is a preliminary attempt to simulate the propagation of LGS through the various materials in the experimental set up. The model can be used to determine the effect of new parameters on the experimental outcome. Based on the predictions given by the model it can be decided whether the particular parameter is appropriate to use in the experimental set up. Using this model will help in saving time, resources and efforts to a large extent.

This model is however at a very nascent stage and is currently not an accurate predictor of the experimental outcome. The limitations of this model are enumerated in the section 6.4. If these limitations are overcome the model will be able to provide a good estimation of the experimental outcome.

# CHAPTER 7

# Conclusion and Future Directions

The goal of this dissertation was to work towards developing a system to delaminate bacterial biofilm from wound surfaces using LGS (Laser-Generated Shockwaves). Bacterial biofilms impose a major burden on wound care management. They can cause deterioration and prevent healing of wounds such as those caused by burns, in war zones to small common diabetic ulcers. The gold standard method to treat these bacterial biofilm infections is to use physical debridement and application of antibiotics. Physical debridement is very effective but is non-specific so it ends up excoriating healthy tissue below wound tissue and needless to mention it is very painful. Antibiotics are not very effective at low-moderate doses. They only help if the dosage is very high. If used at such high doses, toxicity and development of antibiotic resistance are major concerns. LGS can be used to physically disintegrate the bacterial biofilm present over the surface of the wound. Since it works based on the difference in the material properties of the biofilm and the underlying wound tissue, it is more specific. The use of LGS will also eliminate the concerns over toxicity and development of antibiotic resistance.

The first step towards developing such a treatment methodology was to determine whether LGS can be used to delaminate biofilm off surfaces. *In vitro* experiments were carried out by culturing bacterial biofilm on petrishes and treating them with LGS. The biofilm was successfully delaminated from the surface of the petridish. The minimum energy fluence per unit area required to cause delamination was determined. Using interferometry the value of the peak stress corresponding to the minimum energy fluence

required to cause delamination was established.

While carrying out the biofilm delamination experiments *in vitro* it was seen that treatment with LGS caused small regions of delamination in addition to the main central region of delamination. The reason for these small regions of delamination was not clear. In order to determine the cause of the small regions of delamination as well as visualize the propagation of LGS in order to understand it better, a low cost high speed imaging system was built in the lab. The high speed imaging system was used to image the propagation of LGS through the coupling medium lying in between the shockwave generating apparatus and the biofilm. It was seen that the propagation of shockwave through the coupling medium leads to formations of cavitation bubbles which move towards the biofilm. These bubbles were determined to be the cause of the small regions of delamination around the central region of delamination caused by the LGS.

In order to make this treatment clinically visible it was important to ensure that the LGS would not damage the tissue underlying the biofilm. Preliminary experiments were carried out to study the effect of LGS on *ex vivo* porcine skin. Energy fluences used to study this effect were around those that caused delamination of biofilm from petridish surfaces. At those energy fluences no effect of LGS on *ex vivo* porcine skin could be observed.

A thorough study to determine the damage threshold of *ex vivo* porcine skin was carried out. A wide range of energy fluences and a large number of samples were employed for this study. Using appropriate statistical analysis the minimum energy fluence that caused damage to the *ex vivo* porcine skin was determined.

The above studies have provided an energy fluence window which could be used for

delaminating biofilm from wound surfaces in *in vivo* studies. If an energy fluence lying in this window is chosen to delaminate biofilm from wound surfaces, it will cause delamination of the biofilm and not damage the underlying wound tissue.

Finally, COMSOL was used to model the propagation of LGS through the coupling medium, biofilm and the underlying muscle tissue. This model will be useful in designing *in vivo* experiments in the future. While translating from *in vitro* to *in vivo* settings and finally to a clinical set up. Many changes to the experimental set up and materials used in the experiment will have to be made. Carrying out experiments to determine whether any of the changes will be suitable will prove to be very tedious, and will cost a tremendous amount of time and money. Instead it will be easier to make the changes in the model and find out if they are appropriate. The model can be used to determine the suitability of new materials. It can also be used to understand the effect of multiple shockwaves on the biofilm and the underlying muscle tissue. Using the model will not only save on time, money and efforts, but it will help greatly reduce the number of animals to be used in *in vivo* experiments.

Significant progress to develop a treatment methodology to delaminate biofilm from wound surfaces using LGS has been made. However, a lot more remains to be done in order to finally make this treatment available to patients. Some of the aspects that need to be worked on are:

- Immediate future: Conducting experiments *in vivo*. Up till now experiments have been carried out only on *ex vivo* samples. In order to make this treatment clinically visible *in vivo* trials on animals and thereafter on human subjects need to be carried out. To carry out experiments on *in vivo* subjects a number of aspects will have to looked into among them being building a stage or platform for the animal and a system to deliver the right dose of anesthesia to the animal. Once *in vivo* experi-

ments are performed, more insight into the changes and additions needed to make the treatment more suitable for human subjects will be obtained.

- Long term developments: Making the LGS system automated, portable and robust to make it suitable for clinical applications. Currently the system used to produce LGS is bulky and requires adjustments every time a shockwave needs to be produced. Also any movements or jerks near the system tends to change its settings. It will not be appropriate to use this system for clinical scenarios. A portable system ideally a hand held device as well as a system that produces the appropriate shockwaves irrespective of movements and jerks around it is required to be built.

  Other systems/facilities also have to be worked on to make the treatment clinically visible. For instance an imaging system to image the wound before the treatment is delivered needs to be developed. An appropriate system to deliver anesthesia to the patient needs to be developed. Also it will be good to have a system to stop the treatment immediately in case the patient is experiencing any kind of discomfort.

# APPENDIX A

## Scores for Determining Damage Threshold of *Ex vivo* Porcine Skin

Table A.1: The S scores and D scores of *Ex vivo* Porcine Skin Tissue Sections treated with 0.25J (35.38mJ/$mm^2$) of energy

| Sp. No. | Section 1 | | Section 2 | | Average Score | |
|---|---|---|---|---|---|---|
| | S Score | D Score | S Score | D Score | S Score | D Score |
| 1 | 0 | 0 | 0 | 0 | 0 | 0 |
| 2 | 0 | 0 | 0 | 0 | 0 | 0 |
| 3 | 0 | 0 | 0 | 0 | 0 | 0 |
| 4 | 0 | 0 | 0 | 0 | 0 | 0 |
| 5 | 0 | 0 | 0 | 0 | 0 | 0 |
| 6 | 0 | 0 | 0 | 0 | 0 | 0 |
| 7 | 0 | 1 | 0 | 0 | 0 | 0.5 |
| 8 | 0 | 3 | 0 | 0 | 0 | 1.5 |
| 9 | 0 | 0 | 0 | 0 | 0 | 0 |
| 10 | 0 | 1 | 0 | 1 | 0 | 1 |
| 11 | 0 | 3 | 0 | 2 | 0 | 2.5 |
| 12 | 0 | 1 | 0 | 1 | 0 | 1 |
| 13 | 0 | 0 | 0 | 0 | 0 | 0 |
| 14 | 0 | 0 | 0 | 0 | 0 | 0 |
| 15 | 0 | 0 | 0 | 0 | 0 | 0 |

Table A.2: The S scores and D scores of *Ex vivo* Porcine Skin Tissue Sections treated with 0.50J (70.77mJ/$mm^2$) of energy

| Sp. No. | Section 1 | | Section 2 | | Average Score | |
|---|---|---|---|---|---|---|
| | S Score | D Score | S Score | D Score | S Score | D Score |
| 1 | 0 | 0 | 0 | 0 | 0 | 0 |
| 2 | 0 | 0 | 0 | 0 | 0 | 0 |
| 3 | 0 | 0 | 0 | 0 | 0 | 0 |
| 4 | 0 | 0 | 0 | 0 | 0 | 0 |
| 5 | 0 | 0 | 0 | 0 | 0 | 0 |
| 6 | 0 | 0 | 0 | 0 | 0 | 0 |
| 7 | 0 | 3 | 0 | 0 | 0 | 1.5 |
| 8 | 0 | 0 | 0 | 1 | 0 | 0.5 |
| 9 | 0 | 3 | 0 | 0 | 0 | 1.5 |
| 10 | 0 | 0 | 0 | 0 | 0 | 0 |
| 11 | 0 | 0 | 0 | 1 | 0 | 0.5 |
| 12 | 0 | 1 | 0 | 3 | 0 | 2 |
| 13 | 0 | 1 | 0 | 0 | 0 | 0.5 |
| 14 | 0 | 1 | 3 | 0 | 1.5 | 0.5 |
| 15 | 0 | 0 | 0 | 2 | 0 | 1 |

Table A.3: The S scores and D scores of *Ex vivo* Porcine Skin Tissue Sections treated with 0.75J (106.14mJ/$mm^2$) of energy

| Sp. No. | Section 1 | | Section 2 | | Average Score | |
|---|---|---|---|---|---|---|
| | S Score | D Score | S Score | D Score | S Score | D Score |
| 1 | 2 | 0 | 0 | 0 | 1 | 0 |
| 2 | 0 | 0 | 0 | 0 | 0 | 0 |
| 3 | 0 | 0 | 0 | 0 | 0 | 0 |
| 4 | 0 | 0 | 0 | 0 | 0 | 0 |
| 5 | 0 | 0 | 0 | 0 | 0 | 0 |
| 6 | 0 | 2 | 0 | 3 | 0 | 2.5 |
| 7 | 0 | 3 | 0 | 3 | 0 | 3 |
| 8 | 1 | 2 | 0 | 3 | 0.5 | 2.5 |
| 9 | 1 | 2 | 0 | 2 | 0.5 | 2 |
| 10 | 1 | 0 | 1 | 1 | 1 | 0.5 |
| 11 | 0 | 0 | 0 | 0 | 0 | 0 |
| 12 | 0 | 1 | 0 | 1 | 0 | 1 |
| 13 | 3 | 0 | 0 | 0 | 0.5 | 0 |
| 14 | 2 | 1 | 0 | 0 | 0 | 0.5 |
| 15 | 0 | 1 | 2 | 2 | 0 | 1.5 |

Table A.4: The S scores and D scores of *Ex vivo* Porcine Skin Tissue Sections treated with 1J (141.52mJ/$mm^2$) of energy

| Sp. No. | Section 1 | | Section 2 | | Average Score | |
|---|---|---|---|---|---|---|
| | S Score | D Score | S Score | D Score | S Score | D Score |
| 1 | 0 | 1 | 0 | 0 | 0 | 0.5 |
| 2 | 1 | 0 | 0 | 0 | 0.5 | 0 |
| 3 | 0 | 0 | 0 | 0 | 0 | 0 |
| 4 | 0 | 0 | 0 | 0 | 0 | 0 |
| 5 | 0 | 0 | 0 | 0 | 0 | 0 |
| 6 | 0 | 2 | 0 | 3 | 0 | 2.5 |
| 7 | 1 | 1 | 1 | 1 | 0 | 1 |
| 8 | 1 | 1 | 1 | 1 | 0.5 | 1 |
| 9 | 1 | 1 | 1 | 1 | 1 | 1 |
| 10 | 0 | 2 | 0 | 2 | 0 | 2 |
| 11 | 0 | 2 | 0 | 2 | 0 | 2 |
| 12 | 0 | 0 | 3 | 0 | 1 | 0 |
| 13 | 1 | 1 | 1 | 0 | 0 | 0.5 |
| 14 | 0 | 1 | 0 | 0 | 0 | 0.5 |
| 15 | 0 | 1 | 0 | 1 | 0 | 1 |

Table A.5: The S scores and D scores of *Ex vivo* Porcine Skin Tissue Sections treated with 1.25J (176.9mJ/$mm^2$) of energy

| Sp. No. | Section 1 | | Section 2 | | Average Score | |
|---|---|---|---|---|---|---|
| | S Score | D Score | S Score | D Score | S Score | D Score |
| 1 | 0 | 1 | 0 | 1 | 0 | 1 |
| 2 | 0 | 1 | 0 | 0 | 0 | 0.5 |
| 3 | 0 | 1 | 0 | 1 | 0 | 1 |
| 4 | 0 | 1 | 0 | 1 | 0 | 1 |
| 5 | 0 | 1 | 0 | 1 | 0 | 1 |
| 6 | 0 | 0 | 0 | 0 | 0 | 0 |
| 7 | 0 | 0 | 0 | 0 | 0 | 0 |
| 8 | 3 | 1 | 3 | 1 | 3 | 1 |
| 9 | 1 | 1 | 1 | 1 | 1 | 1 |
| 10 | 1 | 0 | 0 | 1 | 0.5 | 0.5 |
| 11 | 0 | 0 | 0 | 0 | 0 | 0 |
| 12 | 0 | 0 | 0 | 0 | 0 | 0 |
| 13 | 0 | 3 | 0 | 3 | 0 | 3 |
| 14 | 0 | 1 | 0 | 1 | 0 | 1 |
| 15 | 0 | 3 | 3 | 0 | 1.5 | 1.5 |

Table A.6: The S scores and D scores of *Ex vivo* Porcine Skin Tissue Sections treated with 1.5J (212.28mJ/$mm^2$) of energy

| Sp. No. | Section 1 | | Section 2 | | Average Score | |
|---|---|---|---|---|---|---|
| | S Score | D Score | S Score | D Score | S Score | D Score |
| 1 | 2 | 1 | 0 | 0 | 1.5 | 0.5 |
| 2 | 0 | 2 | 0 | 2 | 0 | 2 |
| 3 | 0 | 1 | 0 | 0 | 0 | 0.5 |
| 4 | 0 | 1 | 0 | 2 | 0 | 1.5 |
| 5 | 0 | 1 | 0 | 1 | 0 | 1 |
| 6 | 3 | 2 | 3 | 3 | 3 | 2.5 |
| 7 | 0 | 3 | 0 | 1 | 0 | 2 |
| 8 | 0 | 3 | 0 | 2 | 0 | 2.5 |
| 9 | 0 | 1 | 2 | 2 | 1 | 1.5 |
| 10 | 0 | 3 | 0 | 2 | 0 | 2.5 |
| 11 | 0 | 3 | 0 | 0 | 0 | 1.5 |
| 12 | 0 | 0 | 0 | 0 | 0 | 0 |
| 13 | 0 | 1 | 1 | 1 | 0.5 | 1 |
| 14 | 0 | 0 | 0 | 0 | 0 | 0 |
| 15 | 3 | 0 | 1 | 1 | 2 | 0.5 |

Table A.7: The S scores and D scores of *Ex vivo* Porcine Skin Tissue Sections treated as Control samples

| Sp. No. | Section 1 | | Section 2 | | Average Score | |
|---|---|---|---|---|---|---|
| | S Score | D Score | S Score | D Score | S Score | D Score |
| 1 | 0 | 0 | 0 | 0 | 0 | 0 |
| 2 | 0 | 0 | 0 | 1 | 0 | 0.5 |
| 3 | 0 | 0 | 0 | 0 | 0 | 0 |
| 4 | 0 | 0 | 0 | 0 | 0 | 0 |
| 5 | 0 | 0 | 0 | 0 | 0 | 0 |
| 6 | 0 | 0 | 0 | 0 | 0 | 0 |
| 7 | 0 | 0 | 0 | 0 | 0 | 0 |
| 8 | 0 | 3 | 0 | 0 | 0 | 1.5 |
| 9 | 0 | 0 | 0 | 3 | 0 | 1.5 |
| 10 | 0 | 0 | 0 | 1 | 0 | 0.5 |
| 11 | 0 | 2 | 0 | 2 | 0 | 2 |
| 12 | 0 | 1 | 0 | 1 | 0 | 1 |
| 13 | 0 | 0 | 0 | 0 | 0 | 0 |
| 14 | 0 | 1 | 0 | 1 | 0 | 1 |
| 15 | 0 | 2 | 0 | 0 | 0 | 1 |

# References


[1] J. Costerton, P. S. Stewart, and E. Greenberg, "Bacterial biofilms: a common cause of persistent infections," *Science*, vol. 284, no. 5418, pp. 1318–1322, 1999.

[2] C, S. Konturek, Tand Brzozowski, S. Konturek, A. Kwiecien, E. Dembinski, and P. Hahn, "Influence of bacterial lipopolysaccharide on healing of chronic experimental ulcer in rat," *Scandinavian journal of gastroenterology*, vol. 36, no. 12, pp. 1239–1247, 2001.

[3] G. S. Lazarus, D. M. Cooper, D. R. Knighton, D. J. Margolis, R. E. Percoraro, G. Rodeheaver, and M. C. Robson, "Definitions and guidelines for assessment of wounds and evaluation of healing," *Wound Repair and Regeneration*, vol. 2, no. 3, pp. 165–170, 1994. [Online]. Available: http://dx.doi.org/10.1046/j.1524-475X.1994.20305.x

[4] R. Wolcott, D. Rhoads, M. Bennett, B. Wolcott, L. Gogokhia, J. Costerton, and S. Dowd, "Chronic wounds and the medical biofilm paradigm," *Journal of wound care*, vol. 19, no. 2, p. 45, 2010.

[5] J. Nickel, I. Ruseska, J. Wright, and J. Costerton, "Tobramycin resistance of pseudomonas aeruginosa cells growing as a biofilm on urinary catheter material." *Antimicrobial agents and chemotherapy*, vol. 27, no. 4, pp. 619–624, 1985.

[6] I. W. Sutherland, "Biofilm exopolysaccharides: a strong and sticky framework," *Microbiology*, vol. 147, no. 1, pp. 3–9, 2001. [Online]. Available: http://mic.sgmjournals.org/content/147/1/3.short

[7] H. H. Fang, L.-C. Xu, and K.-Y. Chan, "Effects of toxic metals and chemicals on biofilm and biocorrosion," *Water Research*, vol. 36, no. 19, pp. 4709 – 4716, 2002. [Online]. Available: http://www.sciencedirect.com/science/article/pii/S0043135402002075

[8] C. E. Zobell, "The effect of solid surfaces upon bacterial activity," *Journal of bacteriology*, vol. 46, no. 1, p. 39, 1943.

[9] J. W. Costerton, K. Cheng, G. G. Geesey, T. I. Ladd, J. C. Nickel, M. Dasgupta, and T. J. Marrie, "Bacterial biofilms in nature and disease," *Annual Reviews in Microbiology*, vol. 41, no. 1, pp. 435–464, 1987.

[10] J. Lawrence, D. Korber, B. Hoyle, J. Costerton, and D. Caldwell, "Optical sectioning of microbial biofilms." *Journal of bacteriology*, vol. 173, no. 20, pp. 6558–6567, 1991.

[11] W. Costerton, R. Veeh, M. Shirtliff, M. Pasmore, C. Post, G. Ehrlich et al., "The application of biofilm science to the study and control of chronic bacterial infections," *Journal of clinical investigation*, vol. 112, no. 10, pp. 1466–1477, 2003.

[12] E. Denkhaus, S. Meisen, U. Telgheder, and J. Wingender, "Chemical and physical methods for characterisation of biofilms," *Microchimica Acta*, vol. 158, no. 1-2, pp. 1–27, 2007.

[13] L. R. Hoffman, D. A. D'Argenio, M. J. MacCoss, Z. Zhang, R. A. Jones, and S. I. Miller, "Aminoglycoside antibiotics induce bacterial biofilm formation," *Nature*, vol. 436, no. 7054, pp. 1171–1175, 2005.

[14] H. Dalton, A. Goodman, and K. Marshall, "Diversity in surface colonization behavior in marine bacteria," *Journal of industrial microbiology*, vol. 17, no. 3-4, pp. 228–234, 1996.

[15] D. R. Korber, J. R. Lawrence, H. M. Lappin-Scott, and J. W. Costerton, "Growth of microorganisms on surfaces," *Microbial biofilms*, pp. 15–45, 1995.

[16] G. A. O'Toole and R. Kolter, "Flagellar and twitching motility are necessary for pseudomonas aeruginosa biofilm development," *Molecular microbiology*, vol. 30, no. 2, pp. 295–304, 1998.

[17] A. Heydorn, A. T. Nielsen, M. Hentzer, C. Sternberg, M. Givskov, B. K. Ersbøll, and S. Molin, "Quantification of biofilm structures by the novel computer program comstat," *Microbiology*, vol. 146, no. 10, pp. 2395–2407, 2000.

[18] T. Tolker-Nielsen, U. C. Brinch, P. C. Ragas, J. B. Andersen, C. S. Jacobsen, and S. Molin, "Development and dynamics of pseudomonassp. biofilms," *Journal of bacteriology*, vol. 182, no. 22, pp. 6482–6489, 2000.

[19] P. Stoodley, K. Sauer, D. Davies, and J. W. Costerton, "Biofilms as complex differentiated communities," *Annual Reviews in Microbiology*, vol. 56, no. 1, pp. 187–209, 2002.

[20] J. Wingender, T. R. Neu, and H.-C. Flemming, "What are bacterial extracellular polymeric substances?" in *Microbial extracellular polymeric substances*. Springer, 1999, pp. 1–19.

[21] D. G. Davies, M. R. Parsek, J. P. Pearson, B. H. Iglewski, J. Costerton, and E. Greenberg, "The involvement of cell-to-cell signals in the development of a bacterial biofilm," *Science*, vol. 280, no. 5361, pp. 295–298, 1998.

[22] K. Sauer, A. K. Camper, G. D. Ehrlich, J. W. Costerton, and D. G. Davies, "Pseudomonas aeruginosa displays multiple phenotypes during development as a biofilm," *Journal of bacteriology*, vol. 184, no. 4, pp. 1140–1154, 2002.

[23] W. C. Fuqua, S. C. Winans, and E. P. Greenberg, "Quorum sensing in bacteria: the luxr-luxi family of cell density-responsive transcriptional regulators." *Journal of bacteriology*, vol. 176, no. 2, p. 269, 1994.

[24] P. Stoodley, S. Wilson, L. Hall-Stoodley, J. D. Boyle, H. M. Lappin-Scott, and J. Costerton, "Growth and detachment of cell clusters from mature mixed-species biofilms," *Applied and environmental microbiology*, vol. 67, no. 12, pp. 5608–5613, 2001.

[25] B. E. Lamed R, "Contact and cellulolysis in clostridium thermocellum via extensive surface organelles," *Experientia*, vol. 42, pp. 72–73, 1986.

[26] G. A. James, E. Swogger, R. Wolcott, P. Secor, J. Sestrich, J. W. Costerton, P. S. Stewart et al., "Biofilms in chronic wounds," *Wound Repair and Regeneration*, vol. 16, no. 1, pp. 37–44, 2008.

[27] A. D. Association et al., "Economic costs of diabetes in the us in 2007," *Diabetes care*, vol. 31, no. 3, pp. 596–615, 2008.

[28] M. McGuckin, R. Goldman, L. Bolton, and R. Salcido, "The clinical relevance of microbiology in acute and chronic wounds," *Advances in skin & wound care*, vol. 16, no. 1, pp. 12–23, 2003.

[29] T. Bjarnsholt, K. Kirketerp-Møller, P. Ø. Jensen, K. G. Madsen, R. Phipps, K. Krogfelt, N. Høiby, and M. Givskov, "Why chronic wounds will not heal: a novel hypothesis," *Wound repair and regeneration*, vol. 16, no. 1, pp. 2–10, 2008.

[30] C. Power, J. Wang, S. Sookhai, J. Street, and H. Redmond, "Bacterial wall products induce downregulation of vascular endothelial growth factor receptors on endothelial cells via a cd14-dependent mechanism: implications for surgical wound healing," *Journal of Surgical Research*, vol. 101, no. 2, pp. 138–145, 2001.

[31] R. J. White and K. F. Cutting, "Critical colonization–the concept under scrutiny." *Ostomy/wound management*, vol. 52, no. 11, pp. 50–56, 2006.

[32] L. Hall-Stoodley and P. Stoodley, "Evolving concepts in biofilm infections," *Cellular microbiology*, vol. 11, no. 7, pp. 1034–1043, 2009.

[33] R. D. Wolcott, D. D. Rhoads, S. E. Dowd et al., "Biofilms and chronic wound inflammation," *J Wound Care*, vol. 17, no. 8, pp. 333–341, 2008.

[34] J. A. Schaber, W. J. Triffo, S. J. Suh, J. W. Oliver, M. C. Hastert, J. A. Griswold, M. Auer, A. N. Hamood, and K. P. Rumbaugh, "Pseudomonas aeruginosa forms biofilms in acute infection independent of cell-to-cell signaling," *Infection and immunity*, vol. 75, no. 8, pp. 3715–3721, 2007.

[35] A. H. Rickard, K. R. Colacino, K. M. Manton, R. Morton, E. Pulcini, J. Pfeil, D. Rhoads, R. D. Wolcott, and G. James, "Production of cell–cell signalling molecules by bacteria isolated from human chronic wounds," *Journal of applied microbiology*, vol. 108, no. 5, pp. 1509–1522, 2010.

[36] A. H. Rickard, P. Gilbert, N. J. High, P. E. Kolenbrander, and P. S. Handley, "Bacterial coaggregation: an integral process in the development of multi-species biofilms," *Trends in microbiology*, vol. 11, no. 2, pp. 94–100, 2003.

[37] H.-C. Flemming, T. R. Neu, and D. J. Wozniak, "The eps matrix: the âĂIJhouse of biofilm cellsâĂİ," *Journal of bacteriology*, vol. 189, no. 22, pp. 7945–7947, 2007.

[38] J. W. Costerton, Z. Lewandowski, D. E. Caldwell, D. R. Korber, and H. M. Lappin-Scott, "Microbial biofilms," *Annual Reviews in Microbiology*, vol. 49, no. 1, pp. 711–745, 1995.

[39] P. Phillips, R. Wolcott, J. Fletcher, and G. Schultz, "Biofilms made easy," *Wounds International*, vol. 1, no. 3, pp. 1–6, 2010.

[40] E. Guiot, P. Georges, A. Brun, M. Fontaine-Aupart, M.-N. Bellon-Fontaine, and R. Briandet, "Heterogeneity of diffusion inside microbial biofilms determined by fluorescence correlation spectroscopy under two-photon excitation," *Photochemistry and photobiology*, vol. 75, no. 6, pp. 570–578, 2002.

[41] L. M. Weigel, R. M. Donlan, D. H. Shin, B. Jensen, N. C. Clark, L. K. McDougal, W. Zhu, K. A. Musser, J. Thompson, D. Kohlerschmidt et al., "High-level vancomycin-resistant staphylococcus aureus isolates associated with a polymicrobial biofilm," *Antimicrobial agents and chemotherapy*, vol. 51, no. 1, pp. 231–238, 2007.

[42] Y. Liu and J. Li, "Role of pseudomonas aeruginosa biofilm in the initial adhesion, growth and detachment of escherichia coli in porous media," *Environmental science & technology*, vol. 42, no. 2, pp. 443–449, 2007.

[43] K. Lewis, "Persister cells, dormancy and infectious disease," *Nature Reviews Microbiology*, vol. 5, no. 1, pp. 48–56, 2007.

[44] A. Brooun, S. Liu, and K. Lewis, "A dose-response study of antibiotic resistance inpseudomonas aeruginosa biofilms," *Antimicrobial agents and chemotherapy*, vol. 44, no. 3, pp. 640–646, 2000.

[45] H. Koseoglu, G. Aslan, N. Esen, B. H. Sen, and H. Coban, "Ultrastructural stages of biofilm development of< i> escherichia coli</i> on urethral catheters and effects of antibiotics on biofilm formation," *Urology*, vol. 68, no. 5, pp. 942–946, 2006.

[46] M. E. Olson, H. Ceri, D. W. Morck, A. G. Buret, and R. R. Read, "Biofilm bacteria: formation and comparative susceptibility to antibiotics," *Canadian Journal of Veterinary Research*, vol. 66, no. 2, p. 86, 2002.

[47] J. Conley, M. E. Olson, L. S. Cook, H. Ceri, V. Phan, and H. D. Davies, "Biofilm formation by group a streptococci: is there a relationship with treatment failure?" *Journal of clinical microbiology*, vol. 41, no. 9, pp. 4043–4048, 2003.

[48] V. A. Singh and A. Barbul, "Bacterial biofilms in wounds," *Wound Repair and Regeneration*, vol. 16, no. 1, pp. 1–1, 2008.

[49] R. Wolcott and D. Rhoads, "A study of biofilm-based wound management in subjects with critical limb ischaemia," *Journal of wound care*, vol. 17, no. 4, pp. 145–156, 2008.

[50] G. S. Schultz, D. J. Barillo, D. W. Mozingo, and G. A. Chin, "Wound bed preparation and a brief history of time," *International wound journal*, vol. 1, no. 1, pp. 19–32, 2004.

[51] D. Rhoads, R. Wolcott, and S. Percival, "Biofilms in wounds: management strategies," *Journal of wound care*, vol. 17, no. 11, p. 502, 2008.

[52] S. L. Percival, P. G. Bowler, and J. Dolman, "Antimicrobial activity of silver-containing dressings on wound microorganisms using an in vitro biofilm model," *International wound journal*, vol. 4, no. 2, pp. 186–191, 2007.

[53] G. R. Newman, M. Walker, J. A. Hobot, and P. G. Bowler, "Visualisation of bacterial sequestration and bactericidal activity within hydrating hydrofiber< sup>®</sup> wound dressings," *Biomaterials*, vol. 27, no. 7, pp. 1129–1139, 2006.

[54] R. Wolcott, S. Dowd, J. Kennedy, and C. Jones, "Biofilm-based wound care," *Advances in Wound Care*, vol. 1, no. 3, pp. 311–318, 2010.

[55] J. Costerton and P. S. Stewart, "Battling biofilms." *Scientific American*, vol. 285, no. 1, p. 74, 2001.

[56] E. A. Nelson, S. O'Meara, D. Craig, C. Iglesias, S. Golder, J. Dalton, K. Claxton, S. Bell-Syer, E. Jude, C. Dowson et al., "A series of systematic reviews to inform a decision analysis for sampling and treating infected diabetic foot ulcers," *Health Technology Assessment*, 2006.

[57] K. A. Marr, D. J. Sexton, P. J. Conlon, G. R. Corey, S. J. Schwab, and K. B. Kirkland, "Catheter-related bacteremia and outcome of attempted catheter salvage in patients undergoing hemodialysis," *Annals of internal medicine*, vol. 127, no. 4, pp. 275–280, 1997.

[58] P. S. Stewart and J. William Costerton, "Antibiotic resistance of bacteria in biofilms," *The Lancet*, vol. 358, no. 9276, pp. 135–138, 2001.

[59] C. Fux, J. Costerton, P. Stewart, and P. Stoodley, "Survival strategies of infectious biofilms," *Trends in microbiology*, vol. 13, no. 1, pp. 34–40, 2005.

[60] J. R. Wilson, J. G. Mills, I. D. Prather, and S. D. Dimitrijevich, "A toxicity index of skin and wound cleansers used on in vitro fibroblasts and keratinocytes," *Advances in skin & wound care*, vol. 18, no. 7, pp. 373–378, 2005.

[61] D. Doughty, "A rational approach to the use of topical antiseptics," *Journal of Wound Ostomy & Continence Nursing*, vol. 21, no. 6, pp. 224–231, 1994.

[62] A. Lansdown, "Silver i: its antibacterial properties and mechanism of action," *Journal of wound care*, vol. 11, no. 4, pp. 125–131, 2002.

[63] J. B. Wright, K. Lam, and R. E. Burrell, "Wound management in an era of increasing bacterial antibiotic resistance: a role for topical silver treatment," *American journal of infection control*, vol. 26, no. 6, pp. 572–577, 1998.

[64] S. L. Percival, P. Bowler, and E. J. Woods, "Assessing the effect of an antimicrobial wound dressing on biofilms," *Wound Repair and Regeneration*, vol. 16, no. 1, pp. 52–57, 2008.

[65] M. C. Ammons, "Anti-biofilm strategies and the need for innovations in wound care," *Recent patents on anti-infective drug discovery*, vol. 5, no. 1, pp. 10–17, 2010.

[66] S. A. Jones, P. G. Bowler, M. Walker, and D. Parsons, "Controlling wound bioburden with a novel silver-containing hydrofiber® dressing," *Wound Repair and Regeneration*, vol. 12, no. 3, pp. 288–294, 2004.

[67] T. Bjarnsholt, K. KIRKETERP-MØLLER, S. Kristiansen, R. Phipps, A. K. Nielsen, P. Ø. Jensen, N. Høiby, and M. Givskov, "Silver against pseudomonas aeruginosa biofilms," *Apmis*, vol. 115, no. 8, pp. 921–928, 2007.

[68] S. A. Kramer, "Effect of povidone-iodine on wound healing: a review," *Journal of Vascular Nursing*, vol. 17, no. 1, pp. 17–23, 1999.

[69] E. Presterl, M. Suchomel, M. Eder, S. Reichmann, A. Lassnigg, W. Graninger, and M. Rotter, "Effects of alcohols, povidone-iodine and hydrogen peroxide on biofilms of staphylococcus epidermidis," *Journal of antimicrobial chemotherapy*, vol. 60, no. 2, pp. 417–420, 2007.

[70] R. Niedner, "Cytotoxicity and sensitization of povidone-lodine and other frequently used anti-infective agents," *Dermatology*, vol. 195, no. Suppl. 2, pp. 89–92, 1997.

[71] H. Akiyama, T. Oono, M. Saito, and K. Iwatsuki, "Assessment of cadexomer iodine against staphylococcus aureus biofilm in vivo and in vitro using confocal laser scanning microscopy," *Journal of dermatology*, vol. 31, no. 7, pp. 529–534, 2004.

[72] T. Alandejani, J. Marsan, W. Ferris, R. Slinger, and F. Chan, "Effectiveness of honey on staphylococcus aureus and pseudomonas aeruginosa biofilms," *Otolaryngology–Head and Neck Surgery*, vol. 141, no. 1, pp. 114–118, 2009.

[73] A. Tonks, R. Cooper, K. Jones, S. Blair, J. Parton, and A. Tonks, "Honey stimulates inflammatory cytokine production from monocytes," *Cytokine*, vol. 21, no. 5, pp. 242–247, 2003.

[74] P. K. Singh, M. R. Parsek, E. P. Greenberg, and M. J. Welsh, "A component of innate immunity prevents bacterial biofilm development," *Nature*, vol. 417, no. 6888, pp. 552–555, 2002.

[75] Y. Kaneko, M. Thoendel, O. Olakanmi, B. E. Britigan, P. K. Singh et al., "The transition metal gallium disrupts pseudomonas aeruginosa iron metabolism and has antimicrobial and antibiofilm activity," *Journal of Clinical Investigation*, vol. 117, no. 4, pp. 877–888, 2007.

[76] G. Donelli, I. Francolini, D. Romoli, E. Guaglianone, A. Piozzi, C. Ragunath, and J. Kaplan, "Synergistic activity of dispersin b and cefamandole nafate in inhibition of staphylococcal biofilm growth on polyurethanes," *Antimicrobial agents and chemotherapy*, vol. 51, no. 8, pp. 2733–2740, 2007.

[77] P. Valenti, F. Berlutti, M. P. Conte, C. Longhi, and L. Seganti, "Lactoferrin functions: current status and perspectives," *Journal of clinical gastroenterology*, vol. 38, pp. S127–S129, 2004.

[78] K. Brandenburg, G. Jürgens, M. Müller, S. Fukuoka, and M. H. Koch, "Biophysical characterization of lipopolysaccharide and lipid a inactivation by lactoferrin," *Biological chemistry*, vol. 382, no. 8, pp. 1215–1225, 2001.

[79] E. D. Weinberg, "Human lactoferrin: a novel therapeutic with broad spectrum potential," *Journal of Pharmacy and Pharmacology*, vol. 53, no. 10, pp. 1303–1310, 2001.

[80] M. C. B. Ammons, L. S. Ward, S. T. Fisher, R. D. Wolcott, and G. A. James, "In vitro susceptibility of established biofilms composed of a clinical wound isolate of< i> pseudomonas aeruginosa</i> treated with lactoferrin and xylitol," *International journal of antimicrobial agents*, vol. 33, no. 3, pp. 230–236, 2009.

[81] H. Wakabayashi, K. Yamauchi, T. Kobayashi, T. Yaeshima, K. Iwatsuki, and H. Yoshie, "Inhibitory effects of lactoferrin on growth and biofilm formation of

porphyromonas gingivalis and prevotella intermedia," *Antimicrobial agents and chemotherapy*, vol. 53, no. 8, pp. 3308–3316, 2009.

[82] Y. Che, K. Sanderson, L. F. Roddam, S. M. Kirov, and D. W. Reid, "Iron-binding compounds impair pseudomonas aeruginosa biofilm formation, especially under anaerobic conditions," *Journal of medical microbiology*, vol. 58, no. 6, pp. 765–773, 2009.

[83] G. Gray and S. Wilkinson, "The effect of ethylenediaminetetra-acetic acid on the cell walls of some gram-negative bacteria," *Journal of general microbiology*, vol. 39, no. 3, pp. 385–399, 1965.

[84] J. L. Root, O. McIntyre, N. Jacobs, and C. Daghlian, "Inhibitory effect of disodium edta upon the growth of staphylococcus epidermidis in vitro: relation to infection prophylaxis of hickman catheters." *Antimicrobial agents and chemotherapy*, vol. 32, no. 11, pp. 1627–1631, 1988.

[85] P. Kite, K. Eastwood, S. Sugden, and S. Percival, "Use of in vivo-generated biofilms from hemodialysis catheters to test the efficacy of a novel antimicrobial catheter lock for biofilm eradication in vitro," *Journal of clinical microbiology*, vol. 42, no. 7, pp. 3073–3076, 2004.

[86] S. L. Percival, P. Kite, K. Eastwood, R. Murga, J. Carr, M. J. Arduino, and R. M. Donlan, "Tetrasodium edta as a novel central venous catheter lock solution against biofilm," *Infection control and hospital epidemiology*, vol. 26, no. 6, pp. 515–519, 2005.

[87] L. Martineau and H.-M. Dosch, "Biofilm reduction by a new burn gel that targets nociception," *Journal of applied microbiology*, vol. 103, no. 2, pp. 297–304, 2007.

[88] B. A. Burt, "The use of sorbitol-and xylitol-sweetened chewing gum in caries control," *J Am Dent Assoc*, vol. 137, no. 2, pp. 190–6, 2006.

[89] K. Masako, K. Yusuke, I. Hideyuki, M. Atsuko, M. Yoshiki, M. Kayoko, and K. Makoto, "A novel method to control the balance of skin microflora: Part 2. a study to assess the effect of a cream containing farnesol and xylitol on atopic dry skin," *Journal of dermatological science*, vol. 38, no. 3, pp. 207–213, 2005.

[90] M. Dinno, M. Dyson, S. Young, A. Mortimer, J. Hart, and L. Crum, "The significance of membrane changes in the safe and effective use of therapeutic and diagnostic ultrasound," *Physics in medicine and biology*, vol. 34, no. 11, p. 1543, 1989.

[91] S. Young and M. Dyson, "The effect of therapeutic ultrasound on angiogenesis," *Ultrasound in medicine & biology*, vol. 16, no. 3, pp. 261–269, 1990.

[92] P. Reher, M. Harris, M. Whiteman, H. Hai, and S. Meghji, "Ultrasound stimulates nitric oxide and prostaglandin e< sub> 2</sub> production by human osteoblasts," *Bone*, vol. 31, no. 1, pp. 236–241, 2002.

[93] W. Ennis, P. Foremann, N. Mozen, J. Massey, T. Conner-Kerr, and P. Meneses, "Ultrasound therapy for recalcitrant diabetic foot ulcers: results of a randomized, double-blind, controlled, multicenter study." *Ostomy/wound management*, vol. 51, no. 8, pp. 24–39, 2005.

[94] W. G. Pitt and S. A. Ross, "Ultrasound increases the rate of bacterial cell growth," *Biotechnology progress*, vol. 19, no. 3, pp. 1038–1044, 2003.

[95] J. Carmen, B. Roeder, J. Nelson, B. Beckstead, C. Runyan, G. Schaalje, R. Robison, and W. Pitt, "Ultrasonically enhanced vancomycin activity against staphylococcus epidermidis biofilms in vivo," *Journal of biomaterials applications*, vol. 18, no. 4, pp. 237–245, 2004.

[96] P. Piyasena, E. Mohareb, and R. C. McKellar, "Inactivation of microbes using ultrasound: A review," *International journal of food microbiology*, vol. 87, no. 3, pp. 207–216, 2003, cited By (since 1996):198. [Online]. Available: www.scopus.com

[97] W. G. Pitt, M. O. McBride, J. K. Lunceford, R. J. Roper, and R. D. Sagers, "Ultrasonic enhancement of antibiotic action on gram-negative bacteria." *Antimicrobial Agents and Chemotherapy*, vol. 38, no. 11, pp. 2577–2582, 1994. [Online]. Available: http://aac.asm.org/content/38/11/2577.abstract

[98] G. T. Ensing, D. Neut, J. R. v. Horn, H. C. v. d. Mei, and H. J. Busscher, "The combination of ultrasound with antibiotics released from bone cement decreases the viability of planktonic and biofilm bacteria: an in vitro study with clinical strains," *Journal of Antimicrobial Chemotherapy*, vol. 58, no. 6, pp. 1287–1290, 2006. [Online]. Available: http://jac.oxfordjournals.org/content/58/6/1287.abstract

[99] G. Ensing, B. Roeder, J. Nelson, J. van Horn, H. van Der Mei, H. Busscher, and W. Pitt, "Effect of pulsed ultrasound in combination with gentamicin on bacterial viability in biofilms on bone cements in vivo," *Journal of Applied Microbiology*, vol. 99, no. 3, pp. 443–448, 2005. [Online]. Available: http://dx.doi.org/10.1111/j.1365-2672.2005.02643.x

[100] T. Bigelow, T. Northagen, T. Hill, and F. Sailer, "The destruction of escherichia coli biofilms using high-intensity focused ultrasound," *Ultrasound in Medicine and Biology*, vol. 35, no. 6, pp. 1026–1031, 2009, cited By (since 1996)12.

[101] R. M. Donlan and J. W. Costerton, "Biofilms: Survival mechanisms of clinically relevant microorganisms," *Clinical Microbiology Reviews*, vol. 15, no. 2, pp. 167–193, 2002. [Online]. Available: http://cmr.asm.org/content/15/2/167.abstract

[102] R. Gerber, U. E. Studer, and H. DANUSER, "Is newer always better? a comparative study of 3 lithotriptor generations," *The Journal of urology*, vol. 173, no. 6, pp. 2013–2016, 2005.

[103] K. Novak, M. Govindaswami, J. Ebersole, W. Schaden, N. House, and M. Novak, "Effects of low-energy shock waves on oral bacteria," *Journal of dental research*, vol. 87, no. 10, pp. 928–931, 2008.

[104] G. Delacretaz, K. Rink, G. Pittomvils, J. Lafaut, H. Vandeursen, and R. Boving, "Importance of the implosion of eswl-induced cavitation bubbles," *Ultrasound in medicine & biology*, vol. 21, no. 1, pp. 97–103, 1995.

[105] L. Wang, L. Qin, H.-b. Lu, W.-h. Cheung, H. Yang, W.-n. Wong, K.-m. Chan, and K.-s. Leung, "Extracorporeal shock wave therapy in treatment of delayed bone-tendon healing," *The American journal of sports medicine*, vol. 36, no. 2, pp. 340–347, 2008.

[106] Y.-R. Kuo, C.-T. Wang, F.-S. Wang, K. D. Yang, Y.-C. Chiang, and C.-J. Wang, "Extracorporeal shock wave treatment modulates skin fibroblast recruitment and leukocyte infiltration for enhancing extended skin-flap survival," *Wound Repair and Regeneration*, vol. 17, no. 1, pp. 80–87, 2009.

[107] W. Schaden, A. Fischer, and A. Sailler, "Extracorporeal shock wave therapy of nonunion or delayed osseous union," *Clinical orthopaedics and related research*, vol. 387, pp. 90–94, 2001.

[108] T. Nishida, H. Shimokawa, K. Oi, H. Tatewaki, T. Uwatoku, K. Abe, Y. Matsumoto, N. Kajihara, M. Eto, T. Matsuda et al., "Extracorporeal cardiac shock wave therapy markedly ameliorates ischemia-induced myocardial dysfunction in pigs in vivo," *Circulation*, vol. 110, no. 19, pp. 3055–3061, 2004.

[109] G. Haupt and M. Chvapil, "Effect of shock waves on the healing of partial-thickness wounds in piglets," *Journal of Surgical Research*, vol. 49, no. 1, pp. 45–48, 1990.

[110] L. Gerdesmeyer, C. von Eiff, C. Horn, M. Henne, M. Roessner, P. Diehl, and H. Gollwitzer, "Antibacterial effects of extracorporeal shock waves," *Ultrasound in medicine & biology*, vol. 31, no. 1, pp. 115–119, 2005.

[111] W. Kerfoot, A. Beshai, and C. Carson, "The effect of isolated high-energy shock wave treatments on subsequent bacterial growth," *Urological research*, vol. 20, no. 2, pp. 183–186, 1992.

[112] H. Gollwitzer, C. Horn, C. Von Eiff, M. Henne, and L. Gerdesmeyer, "[antibacterial effectiveness of high-energetic extracorporeal shock waves: an in vitro verification]," *Zeitschrift fur Orthopadie und ihre Grenzgebiete*, vol. 142, no. 4, pp. 462–466, 2003.

[113] P. Müller, B. Guggenheim, T. Attin, E. Marlinghaus, and P. R. Schmidlin, "Potential of shock waves to remove calculus and biofilm," *Clinical oral investigations*, vol. 15, no. 6, pp. 959–965, 2011.

[114] S. Wanner, M. Gstöttner, R. Meirer, J. Hausdorfer, M. Fille, and B. Stöckl, "Low-energy shock waves enhance the susceptibility of staphylococcal biofilms to antimicrobial agents in vitro," *Journal of Bone & Joint Surgery, British Volume*, vol. 93, no. 6, pp. 824–827, 2011.

[115] X.-f. Chen and X.-l. Li, "Extracorporeal shock wave therapy could be a potential adjuvant treatment for orthopaedic implant-associated infections," *Journal of Medical Hypotheses and Ideas*, vol. 7, no. 2, pp. 54–58, 2013.

[116] J. M. Dodick and J. Christiansen, "Experimental studies on the development and propagation of shock waves created by the interaction of short nd: Yag laser pulses with a titanium target: possible implications for nd: Yag laser phacolysis of the cataractous human lens," *Journal of Cataract & Refractive Surgery*, vol. 17, no. 6, pp. 794–797, 1991.

[117] E. Alzner and G. Grabner, "Dodick laser phacolysis: thermal effects," *Journal of Cataract & Refractive Surgery*, vol. 25, no. 6, pp. 800–803, 1999.

[118] S. Lee, D. McAuliffe, H. Zhang, Z. Xu, J. Taitelbaum, T. Flotte, and A. Doukas, "Stress-wave-induced membrane permeation of red blood cells is facilitated by aquaporins," *Ultrasound in medicine & biology*, vol. 23, no. 7, pp. 1089–1094, 1997.

[119] M. Terakawa, M. Ogura, S. Sato, H. Wakisaka, H. Ashida, M. Uenoyama, Y. Masaki, and M. Obara, "Gene transfer into mammalian cells by use of a nanosecond pulsed laser-induced stress wave," *Optics letters*, vol. 29, no. 11, pp. 1227–1229, 2004.

[120] M. Ogura, S. Sato, K. Nakanishi, M. Uenoyama, T. Kiyozumi, D. Saitoh, T. Ikeda, H. Ashida, and M. Obara, "In vivo targeted gene transfer in skin by the use of laser-induced stress waves," *Lasers in surgery and medicine*, vol. 34, no. 3, pp. 242–248, 2004.

[121] S. Lee, D. J. McAuliffe, T. J. Flotte, N. Kollias, and A. G. Doukas, "Photomechanical transcutaneous delivery of macromolecules1," *Journal of investigative dermatology*, vol. 111, no. 6, pp. 925–929, 1998.

[122] N. S. Soukos, S. S. Socransky, S. E. Mulholland, S. Lee, and A. G. Doukas, "Photomechanical drug delivery into bacterial biofilms," *Pharmaceutical research*, vol. 17, no. 4, pp. 405–409, 2000.

[123] N. S. Soukos, S. E. Mulholland, S. S. Socransky, and A. G. Doukas, "Photodestruction of human dental plaque bacteria: enhancement of the photodynamic effect by photomechanical waves in an oral biofilm model," *Lasers in surgery and medicine*, vol. 33, no. 3, pp. 161–168, 2003.

[124] M. Ogura, A. D. Abernethy, R. D. Blissett, K. Ruggiero, S. Som, J. M. Goodson, R. Kent, A. G. Doukas, and N. S. Soukos, "Photomechanical wave-assisted molecular delivery in oral biofilms," *World Journal of Microbiology and Biotechnology*, vol. 23, no. 11, pp. 1637–1646, 2007.

[125] A. G. Doukas, "Laser-generated stress waves in medicine: From tissue injury to drug delivery»," *Biomedical Optical Spectroscopy and Diagnostics, Therapeutic Laser Applications*, vol. 22, p. 3, 1998.

[126] Y. P. Krespi, P. Stoodley, and L. Hall-Stoodley, "Laser disruption of biofilm," *The Laryngoscope*, vol. 118, no. 7, pp. 1168–1173, 2008.

[127] V. Kizhner, Y. P. Krespi, L. Hall-Stoodley, and P. Stoodley, "Laser-generated shockwave for clearing medical device biofilms," *Photomedicine and laser surgery*, vol. 29, no. 4, pp. 277–282, 2011.

[128] Y. P. Krespi, V. Kizhner, L. Nistico, L. Hall-Stoodley, and P. Stoodley, "Laser disruption and killing of methicillin-resistant< i> staphylococcus aureus</i> biofilms," *American journal of otolaryngology*, vol. 32, no. 3, pp. 198–202, 2011.

[129] V. Gupta, A. Argon, J. Cornie, and D. Parks, "Measurement of interface strength by laser-pulse-induced spallation," *Materials Science and Engineering: A*, vol. 126, no. 1, pp. 105–117, 1990.

[130] V. Gupta, A. Argon, D. Parks, and J. Cornie, "Measurement of interface strength by a laser spallation technique," *Journal of the Mechanics and Physics of Solids*, vol. 40, no. 1, pp. 141–180, 1992.

[131] J. Yuan and V. Gupta, "Measurement of interface strength by the modified laser spallation technique. i. experiment and simulation of the spallation process," *Journal of Applied Physics*, vol. 74, no. 4, pp. 2388–2396, 1993.

[132] V. Gupta and J. Yuan, "Measurement of interface strength by the modified laser spallation technique. ii. applications to metal/ceramic interfaces," *Journal of Applied Physics*, vol. 74, no. 4, pp. 2397–2404, 1993.

[133] V. Gupta, J. Yuan, and A. Pronin, "Recent developments in the laser spallation technique to measure the interface strength and its relationship to interface toughness with applications to metal/ceramic, ceramic/ceramic and ceramic/polymer interfaces," *Journal of adhesion science and technology*, vol. 8, no. 6, pp. 713–747, 1994.

[134] J. Yuan, V. Gupta, and M. Kim, "Structure and chemistry of nb/sapphire interfaces, with and without interlayers of sb and cr," *Acta metallurgica et materialia*, vol. 43, no. 2, pp. 769–779, 1995.

[135] V. Gupta, J. Wu, and A. N. Pronin, "Effect of substrate orientation, roughness, and film deposition mode on the tensile strength and toughness of niobium–sapphire interfaces," *Journal of the American Ceramic Society*, vol. 80, no. 12, pp. 3172–3180, 1997.

[136] V. Gupta, V. Kireev, J. Tian, H. Yoshida, and H. Akahoshi, "Glass-modified stress waves for adhesion measurement of ultra thin films for device applications," *Journal of the Mechanics and Physics of Solids*, vol. 51, no. 8, pp. 1395–1412, 2003.

[137] M. Niinomi, "Mechanical properties of biomedical titanium alloys," *Materials Science and Engineering: A*, vol. 243, no. 1, pp. 231–236, 1998.

[138] J. Shim, "The laser spallation technique for measurement of tensile strength of cell/tissue-biomaterial interface and its applications," Ph.D. dissertation, PhD thesis, University of California, Los Angeles, 2005.

[139] Y. H. An and R. J. Friedman, "Laboratory methods for studies of bacterial adhesion," *Journal of Microbiological Methods*, vol. 30, no. 2, pp. 141–152, 1997.

[140] J. Rayner, R. Veeh, and J. Flood, "Prevalence of microbial biofilms on selected fresh produce and household surfaces," *International journal of food microbiology*, vol. 95, no. 1, pp. 29–39, 2004.

[141] A. Navarro, "Laser-generated shockwaves for the disruption of bacterial biofilms," 2013.

[142] M. Vollmer and K.-P. Möllmann, "High speed and slow motion: the technology of modern high speed cameras," *Physics Education*, vol. 46, no. 2, p. 191, 2011.

[143] C. Willert, B. Stasicki, J. Klinner, and S. Moessner, "Pulsed operation of high-power light emitting diodes for imaging flow velocimetry," *Measurement Science and Technology*, vol. 21, no. 7, p. 075402, 2010.

[144] F. Testik, A. Barros, and L. Bliven, "Field observations of multimode raindrop oscillations by high-speed imaging." *Journal of the atmospheric sciences*, vol. 63, no. 10, 2006.

[145] C. E. Webb and J. D. Jones, *Handbook of Laser Technology and Applications: Laser design and laser systems*. CRC Press, 2004, vol. 2.

[146] W. Hiller, H.-M. Lent, G. Meier, and B. Stasicki, "A pulsed light generator for high speed photography," *Experiments in fluids*, vol. 5, no. 2, pp. 141–144, 1987.

[147] A. Brandorff and J. W. Sussmeier, "Method and apparatus for illumination and imaging of a surface using 2-d led array," Apr. 18 1995, uS Patent 5,408,084.

[148] Y. Kato and M. Yuyama, "Illumination apparatus, imaging apparatus and irradiation method for an imaging apparatus comprising light emitting diodes which are duty-driven during an imaging period of a frame period," Jun. 29 2010, uS Patent 7,746,405.

[149] Y. A. Pishchalnikov, O. A. Sapozhnikov, M. R. Bailey, J. C. Williams Jr, R. O. Cleveland, T. Colonius, L. A. Crum, A. P. Evan, and J. A. McAteer, "Cavitation bubble cluster activity in the breakage of kidney stones by lithotripter shockwaves," *Journal of endourology*, vol. 17, no. 7, pp. 435–446, 2003.

[150] J. Fujimoto, W. Lin, E. Ippen, C. Puliafito, and R. Steinert, "Time-resolved studies of nd: Yag laser-induced breakdown. plasma formation, acoustic wave generation, and cavitation." *Investigative ophthalmology & visual science*, vol. 26, no. 12, pp. 1771–1777, 1985.

[151] R. Kong and R. Bhargava, "Characterization of porcine skin as a model for human skin studies using infrared spectroscopic imaging," *Analyst*, vol. 136, no. 11, pp. 2359–2366, 2011.

[152] T. P. Sullivan, W. H. Eaglstein, S. C. Davis, and P. Mertz, "The pig as a model for human wound healing," *Wound repair and regeneration*, vol. 9, no. 2, pp. 66–76, 2001.

[153] C. A. Puliafito, R. F. Steinert, T. F. Deutsch, F. Hillenkamp, E. J. Dehm, and C. M. Adler, "Excimer laser ablation of the cornea and lens. experimental studies." *Ophthalmology*, vol. 92, no. 6, pp. 741–748, 1985.

[154] A. Vogel, M. Capon, M. N. Asiyo-Vogel, and R. Birngruber, "Intraocular photodisruption with picosecond and nanosecond laser pulses: tissue effects in cornea, lens, and retina." *Investigative ophthalmology & visual science*, vol. 35, no. 7, pp. 3032–3044, 1994.

[155] R. Hofmann, P. Olbert, J. Weber, S. Wille, and Z. Varga, "Clinical experience with a new ultrasonic and lithoclast combination for percutaneous litholapaxy," *BJU international*, vol. 90, no. 1, pp. 16–19, 2002.

[156] C. Palmqvist, *Laser Lithotripsy of Kidney Calculi with a Nd: YAG Laser*, 1988.

[157] W. Grundfest, I. Litvack, L. Morgenstern, J. Forrester, I. McDermid, T. Pacala, D. Rider, and J. Laudenslager, "Effect of excimer laser irradiation on human atherosclerotic aorta: amelioration of laser-induced thermal damage," in *Conference on Lasers and Electro-Optics, IEEE/OSA CLEO, Baltimore, MD*, 1984, pp. 196–197.

[158] T. J. Flotte, J. K. Frisoli, M. Goetschkes, and A. G. Doukas, "Laser-induced shock wave effects on red blood cells," in *Optics, Electro-Optics, and Laser Applications in Science and Engineering*. International Society for Optics and Photonics, 1991, pp. 36–44.

[159] M. M. Khosh, W. F. Larrabee, and B. Smoller, "Safety and efficacy of high fluence co 2 laser skin resurfacing with a single pass," *Journal of Cosmetic and Laser Therapy*, vol. 1, no. 1, pp. 37–40, 1999.

[160] J. M. Stuzin, T. J. Baker, T. M. Baker, and A. M. Kligman, "Histologic effects of the high-energy pulsed co2 laser on photoaged facial skin," *Plastic and reconstructive surgery*, vol. 99, no. 6, pp. 2036–2050, 1997.

[161] Y. J. Kim, H.-S. Lee, S.-W. Son, S.-N. Kim, and Y.-C. Kye, "Analysis of hyperpigmentation and hypopigmentation after er: Yag laser skin resurfacing," *Lasers in surgery and medicine*, vol. 36, no. 1, pp. 47–51, 2005.

[162] A. G. Doukas and N. Kollias, "Transdermal drug delivery with a pressure wave," *Advanced drug delivery reviews*, vol. 56, no. 5, pp. 559–579, 2004.

[163] A. Navarro, Z. D. Taylor, A. Z. Matolek, A. Weltman, V. Ramaprasad, S. Huang, D. O. Beenhouwer, D. A. Haake, V. Gupta, and W. S. Grundfest, "Bacterial biofilm disruption using laser-generated shockwaves," in *SPIE BiOS*. International Society for Optics and Photonics, 2012, pp. 82 141H–82 141H.

[164] E. M. Viggen, "Viscously damped acoustic waves with the lattice boltzmann method," *Philosophical Transactions of the Royal Society A: Mathematical, Physical and Engineering Sciences*, vol. 369, no. 1944, pp. 2246–2254, 2011.